JETP Letters, Vol. 80, No. 7, 2004, pp. 465–468. From Pis'ma v Zhurnal Éksperimental'noĭ i Teoreticheskoĭ Fiziki, Vol. 80, No. 7, 2004, pp. 531–534.

On the Thermodynamic and Quantum Fluctuations of the Cosmological Constant¶

G. E. Volovik

Low Temperature Laboratory, Helsinki University of Technology, Box 2200, FIN-02015 HUT, Finland
Landau Institute for Theoretical Physics, Russian Academy of Sciences, Moscow, 119334 Russia
e-mail: volovik@boojum.hut.fi

Received August 16, 2004

Abstract—We discuss, from a condensed-matter point of view, the recent idea that the Poisson fluctuations of the cosmological constant about zero could be a source of the observed dark energy [1, 2]. We argue that the thermodynamic fluctuations of Λ are much bigger. Since the amplitude of the fluctuations is $\propto V^{-1/2}$, where V is the volume of the universe, the present constraint on the cosmological constant provides a lower limit for V that is much larger than the volume within the cosmological horizon. © *2004 MAIK "Nauka/Interperiodica".*

PACS numbers: 04.60.–m; 98.80.Cq

Recently, the following approach to the solution of the cosmological problem has been suggested: the average value of the cosmological constant is zero, $\langle\Lambda\rangle = 0$, due to the ability of the quantum microstructure of space-time to readjust itself and to absorb bulk vacuum energy densities; the observed dark energy is provided by residual quantum fluctuations about zero that simulate a "small" cosmological constant [1, 2].

Here, we discuss this scenario using the condensed-matter approach. In the condensed-matter example of "quantum gravity," the "trans-Planckian" physics is well-known, while gravity naturally emerges in the low-energy corner together with gauge fields and chiral fermions (see [3]). This working model of "quantum gravity" provides us with some criteria for a selection of theories: those theories of a quantum vacuum are favorable which are consistent with its condensed-matter analog. Here, we apply this test to the theory of the fluctuating cosmological constant. We show that this idea is consistent with the condensed-matter "oracle," but that the amplitude of the fluctuations is in contradiction.

The first assumption made in [1, 2], namely, that the average value of Λ is zero ($\langle\Lambda\rangle = 0$) is certainly consistent with the condensed-matter "quantum gravity," where the same cosmological-constant problem arises and is resolved. As in our quantum vacuum, a naive estimation of the energy density of the condensed matter in its ground state gives the following "natural" characteristic value for the induced cosmological constant:

$$\Lambda_0 \sim \frac{E_{\rm Pl}^4}{\hbar^3 c^3}. \qquad (1)$$

Here, $E_{\rm Pl}$ is the corresponding ultraviolet energy cutoff of the atomic scale, which plays the role of the Planck energy scale. However, the microscopic (atomic) physics is well-known, which allows us to make exact calculations of the ground-state energy. One finds that, for the equilibrium ground state (vacuum) in the absence of excitations above the vacuum (matter), the energy density of a system isolated from the environment is exactly zero. In the language of gravity, this means that $\langle\Lambda\rangle = 0$. The contribution Λ_0 from sub-Planckian and Planckian modes of the quantum vacuum is exactly cancelled by the microscopic trans-Planckian (atomic) degrees of freedom without any fine-tuning.

This remarkable result follows from the general thermodynamic analysis applied to the quantum vacuum, which utilizes the Gibbs–Duhem relation (see, e.g., [4]). The same analysis demonstrates that, in the presence of matter, Λ is more or less on the order of the matter density or of other perturbations of the vacuum [3, 4].

If the perturbations of the vacuum are small, the cosmological constant induced by these perturbations may become smaller than the thermodynamic or quantum fluctuations of the cosmological constant about zero. At this point we enter the regime that was considered in [1, 2]. According to this suggestion, the presently observed dark energy is nothing but the fluctuation of the cosmological constant. To test this idea, we extend our thermodynamic analysis to incorporate the thermodynamic and quantum fluctuations of Λ.

The thermodynamic fluctuations of the cosmological constant Λ, and thus of the vacuum pressure $P_{\rm vac} = -\Lambda$, correspond to the thermodynamic fluctuations of pressure in a condensed-matter system—say, in a quantum liquid—when it is close to its ground state (vac-

¶ This article was submitted by the author in English.

uum). In quantum liquids, assuming that the liquid is in equilibrium with the environment, the average pressure is zero ($\langle P\rangle = 0$). This corresponds to

$$\langle \Lambda\rangle = -\langle P_{\rm vac}\rangle = 0 \qquad (2)$$

in the equilibrium vacuum. The thermodynamic fluctuations of pressure are given by the following general thermodynamic relation [5]:

$$\langle P^2\rangle_{\rm Thermal} = -T\left(\frac{\partial P}{\partial V}\right)_S, \qquad (3)$$

where S is entropy, T is temperature, and V is the volume of the system. In quantum liquids, Eq. (3) is expressed through the mass density of the liquid ρ and the speed of sound s:

$$\langle P^2\rangle_{\rm Thermal} = \frac{\rho s^2 T}{V}. \qquad (4)$$

Applying this to the vacuum, we use the fact that, in quantum liquids, the quantity ρs^2 is on the order of the characteristic energy density of the liquid. That is why, in the quantum vacuum, this would correspond to the natural value of the vacuum energy density, i.e., to the natural value of the cosmological constant as expressed in terms of the Planck energy scale in Eq. (1):

$$\rho s^2 \equiv \Lambda_0 \sim \frac{E_{\rm Pl}^4}{\hbar^3 c^3}, \qquad (5)$$

and we have the following estimation for the amplitude of the thermal fluctuations of the cosmological constant:

$$\langle \Lambda^2\rangle_{\rm Thermal} = \langle P_{\rm vac}^2\rangle_{\rm Thermal} = \Lambda_0 \frac{T}{V}. \qquad (6)$$

Thus, the temperature of the universe influences not only the matter degrees of freedom (and thus the geometry of the universe), but it also determines the thermal fluctuations of the cosmological constant. This is an important lesson from condensed-matter physics: the thermal fluctuations of the vacuum pressure are determined by vacuum degrees of freedom, and not by much smaller matter degrees of freedom, as one would naively expect.

Note that, in Eq. (6), Λ_0 is the contribution to the vacuum energy density and to the cosmological constant that comes from the Planck-scale modes in the quantum vacuum. But both in quantum liquids and in the quantum vacuum, the total contribution of all the modes to the energy density is zero if the vacuum is in complete equilibrium ($\langle\Lambda\rangle = 0$). The tiny contribution to the vacuum energy density comes from a small unbalance caused by perturbations of the vacuum state, and here we will discuss the unbalance produced by the "hydrodynamic" fluctuations of the vacuum.

From Eq. (6), we can get an estimate for the quantum fluctuations of the vacuum pressure and the cosmological constant, which are important when temperature becomes comparable to the distance between the quantum levels in the finite volume, i.e., when $T \sim \hbar c/V^{1/3}$. Substituting this T into Eq. (6), one obtains the amplitude of the quantum fluctuations of Λ:

$$\langle \Lambda^2\rangle_{\rm Quantum} = \langle P_{\rm vac}^2\rangle_{\rm Quantum} = \Lambda_0 \frac{\hbar c}{V^{4/3}}. \qquad (7)$$

Let us apply this first to the vacuum in the closed Einsteinian universe, with the volume of the 3D spherical space $V = 2\pi R^3$. This gives the following estimation for the amplitude of the quantum fluctuations of Λ:

$$\sqrt{\langle \Lambda^2\rangle}_{\rm Quantum} \sim \frac{E_{\rm Pl}^2}{\hbar c R^2}. \qquad (8)$$

This is comparable to the mean value of Λ in the Einsteinian universe. For example, in the cold universe, one has $\langle\Lambda\rangle = E_{\rm Pl}^2/8\pi\hbar c R^2$, while in the hot universe, $\langle\Lambda\rangle = 3E_{\rm Pl}^2/16\pi\hbar c R^2$. Moreover, in any reasonable universe, the temperature is much bigger than the quantum limit: $T \gg \hbar c/R$, and thus the thermodynamic fluctuations of Λ highly exceed the value required for the construction of the closed solution. This means that thermodynamic fluctuations would actually destroy the Einstein solution. However, we must note that, in the thermodynamic derivation used, it was assumed that the closed universe is in thermal (but not dynamical) contact with the "environment"; i.e., the universe is immersed in a thermal reservoir at a fixed temperature, say, in analogy to a brane immersed in the higher-dimensional world. The Einsteinian universe under these conditions has been studied in [6]. For the truly closed system, i.e., without any contact at all with the environment, such fluctuations are suppressed due to energy conservation.

Let us now turn to our universe, which is spatially flat and thus formally infinite. What volume is relevant for the thermodynamic and quantum fluctuations? If we suppose that $V \sim R_h^3$, where R_h is on the order of the scale of the cosmological horizon, then, for the amplitude of the quantum fluctuations of Λ, one obtains exactly what was suggested in [1, 2]:

$$\sqrt{\langle \Lambda^2\rangle}_{\rm Quantum} \sim \frac{E_{\rm Pl}^2}{\hbar c R_h^2}. \qquad (9)$$

For the same estimation of the vacuum energy density using different approach, see [7].

Equation (9) gives the correct order of magnitude for Λ in the present universe. However, again this is negligibly small compared to the amplitude of the thermal fluctuations of Λ at any reasonable temperature of the universe. Assuming, for example, that the temperature of the universe coincides with the temperature

$T_{\rm CMB}$ of the cosmic microwave background (CMB) radiation, one obtains the following amplitude:

$$\sqrt{\langle\Lambda^2\rangle}_{\rm CMB} \sim \frac{E_{\rm Pl}^2 T_{\rm CMB}^{1/2}}{(\hbar c)^{3/2} R_h^{3/2}} \sim 10^{14}\frac{E_{\rm Pl}^2}{\hbar c R_h^2} \gg \sqrt{\langle\Lambda^2\rangle}_{\rm Quantum}. \quad (10)$$

Such a large value of Λ is certainly in contradiction with observations. This means that we cannot use the volume inside the horizon as the proper volume for the estimation of the quantum and thermal fluctuations of Λ. The reason is that we are interested not in the fluctuations of Λ from one Hubble volume to another, but in the influence of the Λ term on the dynamics of the whole universe. Thus, instead of the Hubble volume R_h^2, one must use the real volume of the universe, which is not limited by the cosmological horizon.

From the condition that the thermal fluctuations of Λ at $T_{\rm CMB}$ must be smaller than the experimental upper limit, $\sqrt{\langle\Lambda^2\rangle}_{\rm CMB} < \Lambda_{\rm exp}$, one can estimate a lower limit for the size of the universe:

$$V > \frac{T_{\rm CMB}\Lambda_0}{\Lambda_{\rm exp}^2} \sim \frac{T_{\rm CMB}}{\hbar H} R_h^3 \sim 10^{28} R_h^3, \quad (11)$$

where $H \sim c/R_h$ is the Hubble constant. Note that, when considering distances much bigger than the size of the horizon, we do not sacrifice the usual notion of causality. The "hydrodynamic" fluctuations of the vacuum are independent in different volumes of the space if these volumes are separated by a distance $|\mathbf{r}_1 - \mathbf{r}_2| > \hbar c/T$:

$$\langle\delta P(\mathbf{r}_1)\delta P(\mathbf{r}_2)\rangle_{\rm Thermal} = \Lambda_0 T\delta(\mathbf{r}_1 - \mathbf{r}_2), \quad |\mathbf{r}_1 - \mathbf{r}_2| > \frac{\hbar c}{T}. \quad (12)$$

Since $T \gg \hbar c/R_h$, the correlations decay at distances much smaller than R_h, and thus we do not need correlations across the horizon.

The expanding universe is certainly not in equilibrium. The noise caused by the deviations from equilibrium adds to the estimated fluctuations and may change the effective temperature. Moreover, Λ in Eq. (9) depends on time in the expanding universe, and this dependence is inconsistent with observations. Supernovae data show that the dark-energy density is either constant with time [8], or that it still may depend on time, but rather weakly [9]. In the latter scenario, the dark-energy density is constant on average up to redshifts of 0.5 and growing for larger redshifts. But it still remains significantly less than the matter energy density.

Our thermodynamic analysis here cannot consider the dynamics of the universe. However, the fact that the dark-energy density is not very far from the density of dark matter demonstrates that the universe is not very far from equilibrium [4], and thus our estimations are not highly distorted by expansion. To incorporate fluctuations of the cosmological constant and its time dependence in the real universe, the Einstein equations must be modified; otherwise, both the fluctuations and the time-dependence are prohibited by Bianchi identities. But even in this case, the condensed-matter "quantum gravity" can be useful, since it provides us with a general scheme of how the dissipation is introduced. Following this scheme, one can incorporate into the Einstein equations the extra terms that contain the time derivative of Λ [10]. Modification of the Einstein equations was also suggested in [2], but that represents the particular case of the two-parametric modification suggested in [10]. The two parameters introduced in [10] and considered as phenomenological fitting parameters can in principle fit the real behavior of Λ in an expanding universe.

Our last comment concerns the emergent gravity and relativistic quantum field theory in condensed-matter systems in general. The usage of fermionic condensed matter as a primer of emergent physics does not mean that we necessarily return to a view of space-time as an absolute background structure incorporating absolute simultaneity. The emergence is based on the general topological properties of fermionic vacuums in momentum space (see Chapter 8 of [3]) that are not sensitive to the background geometry: the background can be Galilean, Lorentzian, or something else. The only requirement for the application of the topology in momentum space is the invariance of the vacuum under translations, so that the Green's function can be represented in terms of the four-momentum. If the universe is inhomogeneous, the four-momentum and, thus, the momentum-space topology are well-determined in the quasiclassical limit, i.e., for wavelengths much smaller than the characteristic size of the universe. This is enough for the construction of the universality classes of quantum vacuums. For one of the two important universality classes, the main physical laws of the Standard Model and of gravity gradually emerge in the low-energy corner irrespective of the background. If the background is originally non-Lorentzian, the information on this background is lost in the low-energy corner where the effective Lorentzian space-time gradually arises.

It was recently suggested from a consideration of the highest energy cosmic rays yet observed that Lorentzian invariance is probably more fundamental than all other physical laws, since it persists even well beyond the Planck energy scale $E_{\rm Pl}$ [11]. This is an encouraging fact for the emergent physics. According to Bjorken [12], the emergence can explain the high precision of the present physical laws only if there is an extremely small expansion parameter. This small parameter can be the ratio of the energy scales, namely, $E_{\rm Pl}/E_{\rm Lorentz}$, where $E_{\rm Lorentz} \gg E_{\rm Pl}$ is the energy scale

where the Lorentz invariance is violated. In the effective action for the gauge and gravity fields obtained by integration over fermions, the integration region is limited by the Planck energy cutoff. If $E_{\rm Pl} \ll E_{\rm Lorentz}$, then integration is concentrated in the fully relativistic region, where fermions are still very close to Fermi points and thus obey the effective gauge invariance and general covariance that follow from the topology of a Fermi point (see Chapter 33 of [3]). As a result, the effective bosonic action also becomes invariant, and the precision of the emergent physical laws is determined by some power of $E_{\rm Pl}/E_{\rm Lorentz}$.

This is the reason why we assume that Lorentzian invariance is obeyed at the microscopic level. The Lorentzian invariance implies that the analog of the vacuum speed of sound s in Eq. (4) coincides with the speed of light c. As a result, the thermal fluctuations of Λ are determined by the "bare" vacuum energy Λ_0 according to Eq. (5).

In conclusion, from the condensed-matter analog of "quantum gravity," it follows that the main idea of [1, 2], i.e., that fluctuations $\sqrt{\langle \Lambda^2 \rangle}$ of the cosmological constant may dominate over its mean value $\langle \Lambda \rangle$, is correct. However, it appears that the thermal fluctuations of Λ at any reasonable temperature of the universe are much larger than the "quantum" Poisson-type fluctuations suggested in [1, 2]. If this analogy is correct, then the thermal fluctuations of Λ impose a limit on the size of the universe, which must be at least nine orders of magnitude bigger than the size of the cosmological horizon.

I am grateful to J.D. Bjorken, P.B. Greene, T. Padmanabhan, L. Smolin, R.D. Sorkin, and A.A. Starobinsky for e-mail correspondence. This work is supported in part by the Russian Foundation for Basic Research (project no. 02-02-16218), the Russian Ministry of Education and Science (project no. NSh-2338.2003.2 for Leading Scientific Schools and the Research Program "Cosmion"), and the European Science Foundation (Program COSLAB).

REFERENCES

1. T. Padmanabhan, Class. Quantum Grav. **19**, L167 (2002); gr-qc/0204020.
2. M. Ahmed, S. Dodelson, P. B. Greene, and R. Sorkin, Phys. Rev. D **69**, 103523 (2004); R. Sorkin, Int. J. Theor. Phys. **36**, 2759 (1997).
3. G. E. Volovik, *The Universe in a Helium Droplet* (Clarendon Press, Oxford, 2003).
4. G. E. Volovik, gr-qc/0405012.
5. L. D. Landau and E. M. Lifshitz, *Statistical Physics*, 2nd ed. (Nauka, Moscow, 1964; Pergamon, London, 1959).
6. C. Barceló and G. E. Volovik, Pis'ma Zh. Éksp. Teor. Fiz. **80**, 239 (2004) [JETP Lett. **80**, 209 (2004)]; gr-qc/0405105.
7. J. D. Bjorken, Phys. Rev. D **64**, 085008 (2001).
8. A. G. Riess, L.-G. Strolger, J. Tonry, *et al.*, Astrophys. J. **607**, 665 (2004).
9. U. Alam, V. Sahni, T. D. Saini, and A. A. Starobinsky, astro-ph/0311364; U. Alam, V. Sahni, and A. A. Starobinsky, J. Cosmol. Astropart. Phys. **0406**, 008 (2004); astro-ph/0403687; R. A. Daly and S. G. Djorgovsky, astro-ph/0403664; Astrophys. J. (2004) (in press).
10. G. E. Volovik, in *Patterns of Symmetry Breaking*, Ed. by H. Arodz, J. Dziarmaga, and W. H. Zurek (Kluwer Academic, Dordrecht, 2003), p. 381; gr-qc/0304061.
11. O. Gagnon and G. D. Moore, hep-ph/0404196.
12. J. D. Bjorken, Phys. Rev. D **67**, 043508 (2003).

JETP Letters, Vol. 80, No. 7, 2004, pp. 469–473. Translated from Pis'ma v Zhurnal Éksperimental'noĭ i Teoreticheskoĭ Fiziki, Vol. 80, No. 7, 2004, pp. 535–540.

Focusing of Parametric X-ray Radiation

A. V. Shchagin

National Science Center Kharkov Institute of Physics and Technology, ul. Akademicheskaya 1, Kharkov, 61108 Ukraine
e-mail: shchagin@kipt.kharkov.ua

Received May 31, 2004; in final form, August 12, 2004

The possibility of focusing parametric x rays (PXRs) without x-ray optics has been shown. Parametric x rays are emitted by channeled relativistic charged particles moving along a bent crystal. Parametric x rays emitted from the entire length of the bent crystal are focused at two points on the bending axis of the crystal. The Huygens picture of formation of focused PXRs is given. The width of the spectral peak of this radiation has been estimated. Certain properties of focused PXRs are estimated for typical experimental conditions, and possibilities for the application of focused PXRs are discussed. An experiment for the observation of focused PXRs has been proposed. It has been shown that focused PXRs can be observed for a proton energy of several tens of GeVs or higher. © *2004 MAIK "Nauka/Interperiodica".*

PACS numbers: 41.50.+h; 41.60.–m; 61.80.Cb; 61.85.+p

The possibility of using crystals to control the motion of charged particles was predicted in [1]. This control can be realized for channeled particles moving through a long, smoothly bent crystal [2, 3]. In particular, experiments on the deflection, focusing, and extraction of proton beams by means of bent crystals were carried out in Serpukhov with a 70-GeV proton beam [4, 5], at CERN for 120 [6] and 450 [7, 8] GeV, and at Fermilab for 900 GeV [9]. The control is most efficient for the planar channeling of positive particles (see, e.g., [7]). Bent crystals with a length of several centimeters are usually used in experiments. Such crystals can likely be used as radiators for obtaining focused parametric x rays (PXRs) from channeled relativistic particles.

Since 1985, experimental investigations of PXRs from relativistic electrons crossing unbent thin crystals have been carried out to study their properties and to develop a new source of a quasi-monochromatic polarized x-ray beam. It was shown that the yield of PXRs is maximal near the Bragg direction with respect to a crystallographic plane (PXR reflection). The PXR reflection was observed and studied with electron beams of energies from several MeVs to several GeVs and for PXR energies from several to several hundreds of keVs. In most available papers, the applicability of Ter-Mikaelyan theory [10] for describing the observed properties of PXRs was shown. General information on the nature, properties, and investigations of PXRs, as well as references to original works, can be found in reviews [11–14]. An experiment on the observation of proton-emitted PXRs was described in [15]. However, PXRs from channeled particles moving through a bent crystal have not yet been studied as far as I know.

Let us consider focusing PXRs [16]. We assume that channeled relativistic charged particles move along a bent thin single-crystal plate as shown in Fig. 1. The crystal is bent with a bending radius R about the f axis. Particles move along the crystallographic plane denoted by the reciprocal-lattice vector $\mathbf{g}$. They cross other crystallographic planes and emit PXR reflections in the Bragg directions with respect to these planes. In this work, we consider PXR reflections from crystallographic planes located at an angle of 45° with respect to the trajectory of a particle perpendicular to the plane of Fig. 1a. These crystallographic planes are denoted by the reciprocal-lattice vectors $\mathbf{g}_1$ and $\mathbf{g}_2$. Reflections of PXRs from these planes are emitted perpendicularly to both the particle trajectory and the crystal-plate plane. Reflections of PXRs from planes $\mathbf{g}_1$ are emitted from the concave side of the plate and converge in the f-axis direction. The maxima of radiation in these reflections cross each other on the f axis or, in other words, are focused. Thus, PXRs from crystallographic planes $\mathbf{g}_1$ that are emitted from the entire length of the bent crystal (several centimeters) are accumulated (focused) near the f axis. Reflections of PXRs from planes $\mathbf{g}_2$ are emitted from the convex side of the plate and diverge in the directions opposite to the f axis.

A classical expression for the frequency of PXRs from an unbent crystal [10] can be obtained from the constructive-interference condition for sequential radiation bursts that arise when a particle crosses crystallographic planes. The phase difference of radiation from neighboring crystallographic planes must be a multiple of 2π (see the Huygens picture in [12, 14]). In the case under consideration, PXRs are formed similarly. However, radiation bursts occur periodically on the curvilinear trajectory of the particle rather than on a straight line. Figure 1a shows the Huygens picture for this case. The phase difference between the wave fronts of converging radiation from neighboring crystallographic

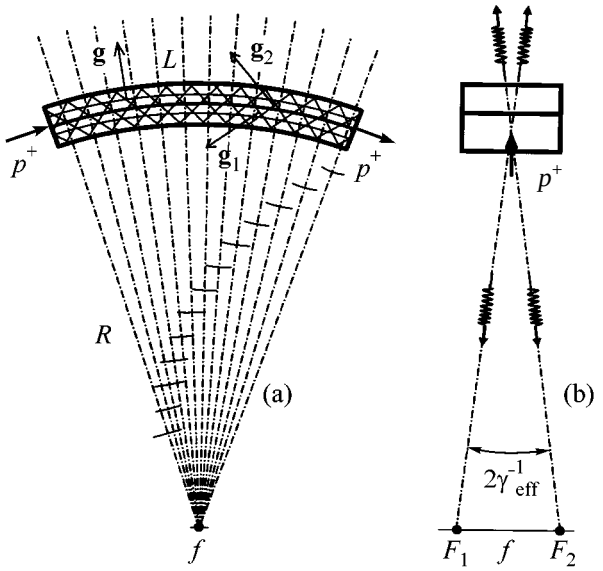

Fig. 1. Huygens picture and focusing PXRs emitted by channeled particles moving along a thin bent single-crystal plate: (a) side and (b) front views. The trajectory of a particle is denoted by arrows p^+. Particles move along the crystallographic planes denoted by the reciprocal-lattice vector **g**. The crystal is bent with the bending radius R about the f axis. The directions of radiation propagation are shown by wavy lines with arrows in panel (b). Parametric x rays from the crystallographic planes denoted by the reciprocal-lattice vector $\mathbf{g}_1$ are focused at points F_1 and F_2 on the f axis. Reflections of PXRs from the crystallographic planes denoted by the reciprocal-lattice vector $\mathbf{g}_2$ are emitted in opposite directions. Parametric x rays focused at points F_1 and F_2 are linearly polarized virtually in the plane of panel (b). Sections of the spherical wave fronts of radiation arising at the points of crossing of crystallographic planes by the particle are shown on the radial lines R in panel (a). A wave train with wavelength $\lambda = c2\pi\sqrt{2}/Vg_1$, train length $l = cL/V$, and number of periods $n = Lg_1/2\pi\sqrt{2}$ is focused near the f axis.

planes is a multiple of 2π. The frequency of PXRs emitted in the direction of the bending axis f by a channeled particle moving along the bent crystal is obviously equal to the frequency of PXRs emitted perpendicularly to the straight-line trajectory of the particle in the unbent crystal. In both cases, the energy E (frequency ω) is expressed as

$$E = \hbar\omega = V\hbar g_1/\sqrt{2}. \quad (1)$$

Here, V is the particle velocity and $g_1 = |\mathbf{g}_1| = 2\pi/a$, where a is the distance between neighboring crystallographic planes that are described by the reciprocal-lattice vector $\mathbf{g}_1$. In such a way, monochromatic radiation from periodically distributed discrete sources is formed and arrives at the focus with a phase difference that is equal to or a multiple of 2π. For brevity, we call such formation as focusing PXRs. The frequency of PXRs on the f axis is independent of the bending radius R.

From the classical point of view, a wave train arriving at the focus has constant amplitude and a number of periods equal to the number of crystallographic planes $n = Lg_1/2\pi\sqrt{2}$ that are crossed by the particle. Formation of the train is shown in Fig. 1a. The train propagation direction varies within a small angle L/R. The relative natural width of the spectral peak of this radiation can be estimated as $\Delta E/E \sim 1/n$. From the quantum point of view, a quantum of this radiation with energy E may arrive at the focus in the time interval $\Delta t = L/V$, equal to the time of particle motion through the crystal. In this case, the natural width of the spectral peak of PXRs can be estimated from the Heisenberg uncertainty relation $\Delta E\Delta t \sim \hbar$. Using Eq. (1), we obtain $\Delta E/E \sim 1/2\pi n$. Thus, the classical and quantum estimates almost coincide with each other. According to these estimates, the relative natural width of the spectral peak of focused PXRs is very small, $\sim 1/n$. However, this estimate is valid only for an infinitely small detector and ideal experimental conditions. In an actual experiment, the spectral peak will be broadened due to the finite angular size of the detector, the angular resolution of the experiment as a whole, the deviation of the shape of the bent crystal from the cylindrical shape, the effect of the radiation of unchanneled particles, and other experimental factors.

The properties of the PXR reflection emitted at right angle to the particle beam in thin crystals were studied in several works. In particular, the image of such PXR reflection was obtained in [17], its polarization was considered in [18], and the detailed structure of the angular distribution of the PXR yield was analyzed in [19]. For example, the angular distribution of the yield in the PXR reflection was shown in figures in [14, 17, 19], and the angular distribution of linear-polarization directions, in [14, 18]. The angular distribution of the PXR yield in the reflection at right angles to the particle trajectory has two maxima in the plane perpendicular to the particle trajectory at an angular distance of $2\gamma_{\text{eff}}^{-1}$ from each other. Therefore, the PXRs are focused near two points F_1 and F_2 on the f axis in the plane of Fig. 1b at the distance $2\gamma_{\text{eff}}^{-1}R$ from each other. Here, $\gamma_{\text{eff}}^{-1} = \sqrt{\gamma^{-2} + |\chi_0|}$, where γ_{eff} is the effective relativistic factor in the medium [14], γ is the relativistic factor of incident particles, and χ_0 is the dielectric susceptibility of the medium.

The size of the spot of PXRs focused near point F_1 or F_2 is equal to about $\gamma_{\text{eff}}^{-1}R$. When the observation point is shifted by a distance b from the f axis in the hor-

izontal direction (in Fig. 1a), the energy (frequency) of PXRs in the spot near points F_1 and F_2 changes by

$$\Delta E = E\frac{b}{R}. \quad (2)$$

However, when the observation point is shifted in the direction parallel to the f axis, the frequency of PXRs does not change [10, 20, 21]. Parametric x rays are linearly polarized near points F_1 and F_2. The direction of linear polarization in both symmetric spots lies virtually in the plane of Fig. 1b. Thus, focused PXRs are linearly polarized in the plane of Fig. 1b.

Particles moving through the plate not only emit PXRs but also ionize and excite the atoms of the crystal. These atoms emit characteristic x rays (CXRs), which are isotropic and not focused but which are also present at points F_1 and F_2.

Let us estimate some properties of focused PXRs for typical experimental conditions, where 70- and 450-GeV protons move along a silicon single-crystal plate with thickness $T = 0.5$ mm, length $L = 5$ cm, and bending radius $R = 5$ m. Channeled protons move along the (110) crystallographic plane, which is denoted by the reciprocal-lattice vector $\mathbf{g} = \langle \bar{1}\bar{1}0\rangle$ in Fig. 1. Reflections of PXRs are formed on crystallographic planes parallel to the reciprocal-lattice vectors $\mathbf{g}_1 = \langle 100\rangle$ and $\mathbf{g}_2 = \langle 0\bar{1}0\rangle$ shown in Fig. 1. The number of PXR quanta I_{PXR} per proton per 1 cm^2 at points F_1 or F_2 was calculated by the formula

$$I_{\mathrm{PXR}} = Y\frac{L}{T}\Omega, \quad (3)$$

where $\Omega = S/R^2$ is the solid angle of the detector that has area $S = 1$ cm^2 and is placed at point F_1 or F_2, and Y is the differential yield of PXRs at the maximum of the reflection at an angle of 90° to the particle velocity with allowance for the attenuation of this radiation in the Si single-crystal target from which it is emitted in the Laue or Bragg geometry, that has thickness $T/\sqrt{2}$, and that is placed at an angle of 45° to the beam axis. This differential yield Y is equal to the differential yield of PXRs from the bent-crystal section with a length T that is irradiated by particles uniformly distributed along the thickness of the crystal. The differential yield Y with allowance for the attenuation of radiation in the target was calculated by formulas taken from [12, 14, 22] that were derived in Ter-Mikaelyan kinematic theory [10]. Reflections of PXRs that are focused near points F_1 and F_2 are formed on the (400), (800), and (12 00) crystallographic planes, which are parallel to the (100) plane and have a nonzero structure factor. Reflections of PXRs from planes with higher Miller indices give a much lower yield of radiation. Reflections of PXRs from similar crystallographic planes parallel to the $(0\bar{1}0)$ plane are emitted in directions opposite to the f axis from the convex side of the plate. They form a virtual image of the radiation sources at points F_1 and F_2. The special case of diffraction of channeling radiation [23], as well as other types of radiation from a particle in the crystal, is not considered in this work. The multiple scattering of protons was ignored because they are channeled in the crystal.

In the case under consideration, the $\langle \bar{1}10\rangle$ crystallographic axis is oriented along the proton beam. To avoid the axial channeling of protons in an experiment, the crystal lattice must be reoriented in the (110) plane by an angle slightly exceeding the Lindhard critical channeling angle. The critical channeling angles for 70- and 450-GeV protons in the Si single crystal are equal to about 2.4×10^{-5} and 10^{-5}, respectively [2]. These angles are much smaller than the characteristic angular sizes of PXR reflections, which are determined by the parameter $\gamma_{\mathrm{eff}}^{-1}$ (see table). Therefore, the basic properties of PXRs and the positions of points F_1 and F_2 change only slightly when the lattice is so slightly reoriented with respect to the particle beam.

The properties of PXRs are determined by the relativistic factor and the magnitude of the incident-particle charge [10, 12, 22]. Therefore, the above calculations would be valid for 38- and 245-MeV positrons and electrons that have the same relativistic factor. However, the motion of these particles in a long crystal may differ strongly from the motion of protons. For example, a considerable part of the high-energy protons can move through the long bent crystal in the channeling regime [2–9]. At the same time, channeled electrons are strongly scattered. As far as I know, the motion of channeled positrons in bent crystals, as well as the emission of PXRs by positrons in any crystals, has not yet been studied experimentally.

In addition, the number of 1.74-keV CXR quanta produced due to the ionization of the K shell of Si atoms by relativistic protons was estimated by the formula

$$I_{\mathrm{CXR}} = \frac{\sigma_K \omega_K \Omega n_0 L T_e}{4\pi T}. \quad (4)$$

Here, σ_K is the cross section for the K-shell ionization of Si atoms by protons, ω_K is the fluorescence yield, n_0 is the density of atoms in the Si single crystal, and T_e is the length where 1.74-keV radiation is attenuated by a factor of e in the Si single crystal. Calculations were carried out with values of 1654 and 1946 b for the cross section for K-shell ionization by 70- and 450-MeV protons, respectively. These values were calculated for 38- and 245-MeV electrons that have the same relativistic factor as 70- and 450-GeV protons, respectively. Cross sections were calculated according to the recommendations given in [24]. The planar-channeling effect was ignored in these estimates of the CXR yield, because it must be weak for high-energy particles (see references cited in [24]). However, the number of CXR quanta

Properties of CXRs and focused PXRs from 70- and 450-GeV protons moving in the channelling regime along the (110) crystallographic plane in a bent Si single-crystal plate

Radiation		CXRs Si	PXRs (400)	PXRs (800)	PXRs (12 00)
Polarization		no	linear	linear	linear
E, keV		1.74	6.46	12.91	19.37
$(\Delta E/E)_{nat}$			3.84×10^{-9}	1.92×10^{-9}	1.28×10^{-9}
$(\Delta E/E)_D$			2×10^{-3}	2×10^{-3}	2×10^{-3}
T_e in Si, μm		13.3	37	270	865
70-GeV protons	γ_{eff}^{-1}	–	1.42×10^{-2}	1.36×10^{-2}	1.35×10^{-2}
	ΔF, mm	–	142	136	135
	I, photons per cm^{-2} per proton	1.65×10^{-7}	9.56×10^{-8}	1.86×10^{-8}	1.55×10^{-9}
450-GeV protons	γ_{eff}^{-1}	–	5.24×10^{-3}	3.18×10^{-3}	2.63×10^{-3}
	ΔF, mm	–	52.4	31.8	26.3
	I, photons per cm^{-2} per proton	1.94×10^{-7}	6.90×10^{-7}	3.32×10^{-7}	3.98×10^{-8}

Note: The plate has a thickness $T = 0.5$ mm, length $L = 5$ cm, and bending radius $R = 5$ m. The source of radiation (CXRs or focused PXRs from the indicated crystallographic planes) and its polarization are given in the first and second rows of the table; E is the energy of the spectral peak of radiation, $(\Delta E/E)_{nat} = 1/n$ is the relative natural width of the spectral peak of PXRs on the f axis for a point detector, $(\Delta E/E)_D$ is the line width calculated by Eq. (2) for a detector with horizontal size $b = 1$ cm, T_e is the length where radiation with energy E is attenuated by a factor of e in a Si crystal, γ_{eff}^{-1} is the inverse effective relativistic factor (for comparison, the inverse relativistic factor γ^{-1} for 70- and 450-GeV protons is equal to 1.34×10^{-2} and 2.08×10^{-3}, respectively), ΔF is the distance between points F_1 and F_2, I is the number of quanta per proton per 1 cm^2 at points F_1 and F_2 with allowance for the attenuation of x rays in the crystal for the total number of channeled protons randomly distributed over the thickness of the crystal plate.

from channeled protons in experiments must be somewhat less than the estimate obtained here by disregarding the channeling effect.

Calculations were performed for a uniform distribution of protons over the plate thickness. Radiation emitted by channeled protons moves to points F_1 and F_2 across the plate and is attenuated in the Si crystal. The attenuation of radiation in the silicon plate was taken into account in the calculations.

The results of the calculations are presented in the table. The spectrum of x rays at points F_1 and F_2 includes four spectral peaks in the energy region from 1.7 to 19.4 keV. It is convenient to detect this spectrum by a standard Si(Li) x-ray detector. The 1.74-keV peak is attributed to unfocused (isotropic) unpolarized CXRs, which are emitted primarily by protons moving in the 13.3-μm layer on the concave side of the plate. The thickness of this layer is determined by the attenuation of 1.74-keV x rays in the Si crystal (see table). Thus, only a small fraction of protons passing through the plate emit CXRs that arrive at points F_1 and F_2. The other spectral peaks are associated with linearly polarized, focused PXRs. The 6.46- and 12.91-keV spectral peaks of PXRs are attributed primarily to protons moving in the 37- and 270-μm layers, respectively, on the concave side of the plate (see attenuation length in table). The 19.37-keV spectral peak is attributed to almost all protons moving in the plate.

Thus, the sources of radiation for different spectral peaks at points F_1 and F_2 have different distributions over the thickness of the crystal plate. Therefore, measurements and analysis of the relative intensities of these spectral peaks can provide an estimate of the distribution of the proton beam over the crystal thickness. This estimate can be obtained for the entire plate or its separate part if all other parts of the plate are shielded and the x-ray detector can monitor only this separate part of the crystal. Characteristic x rays from the 13.3-μm layer on the convex side of the bent crystal can be detected by another x-ray detector placed opposite the convex side of the bent crystal, because CXRs are isotropic and the number of their quanta must be almost the same on both sides of the crystal.

The angular divergence (convergence) of focused PXRs is equal to L/R in the plane of Fig. 1a. It can be changed by varying the bending radius R of the bent crystal. Thus, we have an x-ray source with a size of several centimeters with the possibility of smoothly controlling its divergence (convergence). Such a source of polarized quasi-monochromatic x rays with the possibility of smoothly controlling its divergence can be used to calibrate x-ray detectors or x-ray optics with a large aperture, such as the objectives of space-based x-ray telescopes [25].

Focused PXRs can be experimentally observed at a proton accelerator with a crystal bent for controlling the

proton beam when the current of channeled particles is approximately equal to or larger than $10^7 p^+$/s. As is seen in the table, all the spectral peaks have comparable intensities for a proton energy of 450 GeV [16]. When the proton energy decreases to 70 GeV, the intensity of high-energy peaks decreases strongly, but low-energy spectral peaks remain observable. An x-ray detector with an area of about 1 cm^2 must be placed at point F_1 or F_2 on the f axis. The asymmetric arrangement of two detectors at points F_1 and F_2 provides for the detection of the maximum number of quanta from various PXR reflections. The detection of PXRs and CXRs from unchanneled particles can be suppressed by measuring the spectrum of x rays in coincidence with particles passed through the bent crystal in the channeling regime. To observe soft x rays, it is necessary to ensure a vacuum connection between the bent crystal and the x-ray detector, because radiation is attenuated in air. X rays with energies of 1.74 and 6.46 keV are almost completely absorbed over a 5-m path in air. However, the spectral peaks of focused PXRs with higher energies can be observed in air. X rays with energies of 12.91 and 19.37 keV are attenuated by factors of 0.23 and 0.60, respectively, over a 5-m path in dry air. The energies of all spectral peaks are virtually independent of the energy of the relativistic particle. However, their intensities may increase (decrease) when the energy of particles increases (decreases) [12, 22].

I am grateful to E.N. Tsyganov for a discussion at the conference "The Future of Accelerator Physics" [3, 26] and to X. Artru, I. Endo, and V.V. Sotnikov for discussions.

REFERENCES

1. E. N. Tsyganov, *Fermilab TM-682* (Batavia, 1976).
2. V. M. Biryukov, Yu. A. Chesnokov, and V. I. Kotov, Usp. Fiz. Nauk **164**, 1017 (1994) [Phys. Usp. **37**, 937 (1994)].
3. E. Tsyganov, in *The Future of Accelerator Physics*, Ed. by T. Tajima (AIP, New York, 1996), AIP Conf. Proc., Vol. 356, p. 73.
4. A. A. Asseev and M. Yu. Gorin, Nucl. Instrum. Methods Phys. Res. B **119**, 210 (1996).
5. Yu. A. Chesnokov, Nucl. Instrum. Methods Phys. Res. B **119**, 163 (1996).
6. K. Elsener, G. Fidecaro, M. Gyr, *et al.*, Nucl. Instrum. Methods Phys. Res. B **119**, 215 (1996).
7. A. Baurichter, K. Kirsebom, R. Medenwaldt, *et al.*, Nucl. Instrum. Methods Phys. Res. B **119**, 172 (1996).
8. N. Doble, L. Gatigton, and P. Grafström, Nucl. Instrum. Methods Phys. Res. B **119**, 181 (1996).
9. C. T. Murphy, R. Carrigan, D. Chen, *et al.*, Nucl. Instrum. Methods Phys. Res. B **119**, 231 (1996).
10. M. L. Ter-Mikaelian, *High-Energy Electromagnetic Processes in Condensed Media* (Akad. Nauk Arm. SSR, Yerevan, 1969; Wiley, New York, 1972).
11. M. L. Ter-Mikaelian, Usp. Fiz. Nauk **171**, 597 (2001) [Phys. Usp. **44**, 571 (2001)].
12. A. V. Shchagin and X. K. Maruyama, in *Accelerator-based Atomic Physics Technique and Applications*, Ed. by S. M. Shafroth and J. C. Austin (AIP Press, New York, 1997), p. 279.
13. P. Rullhusen, X. Artru, and P. Dhez, *Novel Radiation Sources Using Relativistic Electrons* (World Sci., Singapore, 1998).
14. A. V. Shchagin, in *Electron–Photon Interactions in Dense Media*, Ed. by H. Wiedemann (Kluwer Academic, Dordrecht, 2002), NATO Sci. Ser. II: Math., Phys. Chem., Vol. 49, p. 133.
15. V. P. Afanasenko, V. G. Baryshevsky, R. F. Zuevsky, *et al.*, Phys. Lett. A **170**, 315 (1992).
16. A. V. Shchagin, physics/0404137 (2004). Correction: The number of quanta for PXR(12 00) at proton energy 450 GeV in Table 1 must be 3.98×10^{-8} instead of 1.28×10^{-7}.
17. R. B. Fiorito, D. W. Rule, M. A. Piestrup, *et al.*, Phys. Rev. E **51**, R2759 (1995).
18. A. V. Shchagin, Phys. Lett. A **247**, 27 (1998).
19. A. V. Shchagin, Phys. Lett. A **262**, 383 (1999).
20. A. V. Shchagin, V. I. Pristupa, and N. A. Khizhnyak, Phys. Lett. A **148**, 485 (1990).
21. K.-H. Brenzinger, B. Limburg, H. Backe, *et al.*, Phys. Rev. Lett. **79**, 2462 (1997).
22. A. V. Shchagin and N. A. Khizhnyak, Nucl. Instrum. Methods Phys. Res. B **119**, 115 (1996).
23. T. Ikeda, Y. Matsuda, H. Nitta, and Y. H. Ohtsuki, Nucl. Instrum. Methods Phys. Res. B **115**, 380 (1996).
24. A. V. Shchagin, V. I. Pristupa, and N. A. Khizhnyak, Nucl. Instrum. Methods Phys. Res. B **48**, 9 (1994).
25. A. V. Shchagin, N. A. Khizhnyak, R. B. Fiorito, *et al.*, Nucl. Instrum. Methods Phys. Res. B **173**, 154 (2001).
26. A. V. Shchagin, in *The Future of Accelerator Physics*, Ed. by T. Tajima (AIP, New York, 1996), AIP Conf. Proc., Vol. 356, p. 359.

Translated by R. Tyapaev

JETP Letters, Vol. 80, No. 7, 2004, pp. 474–478. From Pis'ma v Zhurnal Éksperimental'noĭ i Teoreticheskoĭ Fiziki, Vol. 80, No. 7, 2004, pp. 541–545.

A Flow Phase Diagram for Helium Superfluids¶

L. Skrbek

Joint Low Temperature Laboratory, Institute of Physics ASCR and Charles University, 18000 Prague, Czech Republic
e-mail: skrbek@fzu.cz

Received September 1, 2004

The existence of the flow phase diagram predicted by Volovik [JETP Lett. **78**, 553 (2003)] is discussed based on the available experimental data for He II and ^{3}He–B. The effective temperature-dependent but scale-independent Reynolds number $\mathrm{Re}_{\mathrm{eff}} = 1/q \equiv (1 - \alpha')/\alpha$, where α and α' are the mutual friction parameters, and the superfluid Reynolds number characterizing the circulation of the superfluid component in units of the circulation quantum are used as the dynamic parameters. In particular, the flow diagram permits the identification of the experimentally observed turbulent states I and II in counterflowing He II with the classical and quantum turbulent regimes suggested by Volovik. © *2004 MAIK "Nauka/Interperiodica".*

PACS numbers: 47.27.Ak; 67.40.Vs; 67.57.De

We consider the flow of quantum liquids such as He II or ^{3}He–B that can be described in the framework of the two-fluid model (see, e.g., [1]). The normal fluid and superfluid velocity fields are coupled by two terms: the Gorter–Mellink term that describes the mutual friction between these two liquids when vortices are present in the superfluid and the temperature-gradient term, which is responsible, e.g., for the fountain effect. The circulation in the superfluid component is quantized in units of κ (0.997×10^{-3} cm^2/s for He II and 0.662×10^{-3} cm^2/s for ^{3}He–B); we assume singly quantized vortices.

Let us consider a flow that can be approximated as isothermal.[1] Then, the generally coupled complex flow of both components described by the two two-fluid equations can be simplified and becomes easier to understand, especially for two extreme cases:

(i) **There are no quantized vortices in the flow.** This represents a situation in which the normal and superfluid velocity fields are fully decoupled. The normal fluid thus obeys the usual Navier–Stokes equation, while the superfluid flow remains potential. Thus, formally, the normal fluid could become turbulent without a single vortex being present in the superfluid—in the absence of mutual friction, the superfluid simply does not "know" what is happening in the normal fluid. In practice, however, remnant vortices are almost always present, at least in He II [2], where they are pinned to walls that are always rough on the atomic scale. In ^{3}He–B, a vortex-free sample is more likely, but the highly viscous normal fluid can hardly become turbulent in a laboratory-scale container.

(ii) **The normal fluid is at rest in some frame of reference.** Such a possibility arises, for example, for ^{3}He–B, whose highly viscous normal component is effectively clamped by the walls in a laboratory-scale container.[2] Following first the original approach of Volovik [3, 4], let us assume that the quantized vortices in the flow are arranged in such a way that the coarse-grained hydrodynamic equation

$$\frac{\partial \mathbf{v}_s}{\partial t} + \nabla\mu = (1 - \alpha')\mathbf{v}_s \times \boldsymbol{\omega} + \alpha\hat{\boldsymbol{\omega}} \times (\boldsymbol{\omega} \times \mathbf{v}_s), \quad (1)$$

obtained from the Euler equation after averaging over vortex lines [5] and written in the frame of reference of the normal fluid, provides a sufficiently accurate description of the superflow. We shall return to the applicability of this equation later. The normal fluid thus provides a unique frame of reference, and we have to deal only with the superfluid velocity $\mathbf{v}_s$. Rescaling the time variable such that $t \longrightarrow 1 - \alpha' t$ leads to

$$\frac{\partial \mathbf{v}}{\partial t} + \nabla\mu = \mathbf{v} \times \boldsymbol{\omega} + q\hat{\boldsymbol{\omega}} \times (\boldsymbol{\omega} \times \mathbf{v}), \quad (2)$$

where $\mathbf{v} = \mathbf{v}_s$, $\boldsymbol{\omega}$ is the course-grained vorticity, and $\hat{\boldsymbol{\omega}}$ is a unit vector in the direction of $\boldsymbol{\omega}$. A theoretical analysis of the fluid dynamical problem based on this equation has been performed by Volovik [3, 4]; Vinen [6]; and L'vov, Nazarenko, and Volovik [7]. As was first emphasized by Finne *et al.* [8], Eq. (2) has a very remarkable property that distinguishes it from the ordinary Navier–Stokes equation, where the relative impor-

¶ This article was submitted by the author in English.

[1] This cannot be strictly true, as dissipation in flowing normal fluid possessing finite viscosity leads to heating in places of high vorticity and to a counterflow. We assume here that the heating is small and can be neglected.

[2] This situation can also occur in He II at a fairly low temperature ($\simeq$1 K and below), where the kinematic viscosity of the normal fluid rapidly increases with decreasing temperature [9].

tance of the inertial and dissipative terms is given by the Reynolds number, which in turn depends on the geometry of the particular flow under study. Here, the role of the effective Reynolds number is played by the parameter $\mathrm{Re}_{\mathrm{eff}} = q^{-1} = (1 - \alpha')/\alpha$, which depends on temperature but not on geometry. We stress that the superfluid Reynolds number (as soon as it is high enough, so that Eq. (2) represents a good approximation of the superflow) is not relevant to a consideration of the problem of a flow obeying Eq. (2), the beauty of which lies in the fact that one is able to derive more general conclusions about turbulent flow generated from suitable initial conditions depending only on a single temperature-dependent parameter $1/q$, regardless of the actual geometry of the flow. A wide range of q values is easily experimentally achievable, with q increasing with temperature in both He II [9] and ^{3}He–B [10].

Like the usual Navier–Stokes equation, Eq. (2) has both laminar (for $q \gg 1$) and turbulent solutions. For $q \ll 1$, it describes fully developed turbulence. The latter is discussed in detail in [3, 4], where it is shown that a turbulent cascade will develop in a range of scales. It was claimed, however, that the 3D energy spectrum is of a usual[3] Kolmogorov form $E(k) \cong \varepsilon^{2/3}k^{-5/3}$.

Vinen [6] recently developed a different approach to superfluid turbulence in the presence of a stationary normal fluid. His approach is based on physical arguments concerning the turnover and decay times of eddies of various sizes, and the results are confirmed by numerical solutions of a diffusion equation that describes flow of turbulent energy in k space. Owing to the action of mutual friction, there is strong damping of large eddies, with the result that, at low wave numbers, the energy spectrum falls off much more rapidly (approaching k^{-3}) than for the Kolmogorov spectrum. However, the damping remains weak for small eddies, so that the Kolmogorov spectrum is recovered for large k beyond a certain critical wave number. Vinen also correctly points out that this feature is inherently contained in Eq. (2).

The most recent theoretical discussion of this issue, by L'vov, Nazarenko, and Volovik [7], which is based on an analytical solution of the first-order k-space diffusion equation, confirms the crucial role of mutual friction forces on a large scale. Moreover, scenarios of various turbulent regimes depending on various parameters of the flow are suggested and discussed.

Although this interesting problem of superfluid turbulence in the presence of a stationary normal fluid is most likely not yet fully settled, we believe that the main features of such a turbulent superflow have been firmly established.

The continuous approach for considering superfluid turbulence based on Eq. (2) would be fully applicable in the limit $\kappa \longrightarrow 0$. As pointed out by Volovik [3, 4], at finite κ one has to ensure that, at the smallest scale r_0, the "granularity" due to individual vortices does not become important, so that the circulation $v_{r0}r_0 = q^2UR = q^2\kappa\mathrm{Re}_s > \kappa$. This leads to an important criterion: $\mathrm{Re}_s > 1/q^2 \gg 1$. Indeed, the turbulent cascade might reach small scales containing only a few quantized vortices and most likely continues past that level (perhaps in the form of a Kelvin wave cascade), but the form of the energy spectrum around and beyond the quantum scale [11], $l_q \approx (\varepsilon/\kappa^3)^{-1/4}$, must depend explicitly on κ.[4]

In order to apply an analysis based on Eq. (2), we must bear in mind that this coarse-grained equation sufficiently accurately describes the superfluid velocity field on the scale over which the averaging is done. Therefore, this approach cannot include initial conditions similar to those commonly believed to apply in counterflow turbulence in He II if only a single scale is assumed. Such a distribution of vortices will most likely be described by the Vinen equation [12]. It is well known and in agreement with simulations by Schwarz [13][5] that there is a critical self-sustaining counterflow velocity above which the turbulence is in dynamical equilibrium. According to these computer simulations and to a common belief based on the experiments of Awschalom *et al.* [14], this state is, at least approximately, homogeneous. If it contains just one scale, the vortex line density L ought to decay as $1/t$, as follows from the Vinen equation and, according to some experiments [12, 15], it most likely does.

Now, let us increase the counterflow velocity U_{cf}, assuming the normal fluid velocity profile remains flat, and continue the discussion in the reference frame where the normal fluid is at rest. It is an established experimental fact that another transition (from turbulent state I to turbulent state II with distinctly different features, in accord with Tough's classification scheme [1]) occurs [1, 17, 18]. It has been a long-lasting challenge to explain the nature of this transition. We believe that the answer might be hidden in Volovik's analysis [3, 4]. As he claims, there is a crossover between what he calls the Kolmogorov and Vinen states of superfluid turbulence when

$$\mathrm{Re}_s q^2 = U_{cf}Rq^2/\kappa \simeq 1. \qquad (3)$$

[3] Possibly logarithmically corrected (see [4]).

[4] The relevant discussion is contained in [11]; here, we only remind the reader that the exact functional form of the spectral energy density $\Phi(\varepsilon, k, \kappa)$ around and beyond l_q cannot be written explicitly based on a dimensional analysis similar to that of Kolmogorov (see [11]), as it can contain, in principle, any function of the dimensionless combination $\varepsilon\kappa^{-3}k^{-4}$. However, the form of $\Phi(\varepsilon, k, \kappa)$ can be judged if one uses experimental data on the late decay of the grid-generated turbulence [16], relevant to scales of order $l_{\mathrm{diss}} \approx (\varepsilon/\nu_n^3)^{-1/4}$, where the normal fluid can be considered to be at rest.

[5] Note, however, that these simulations have been performed using the so-called local induction approximation, so that the nonlocal interaction as it takes place in classical turbulence is automatically cut out.

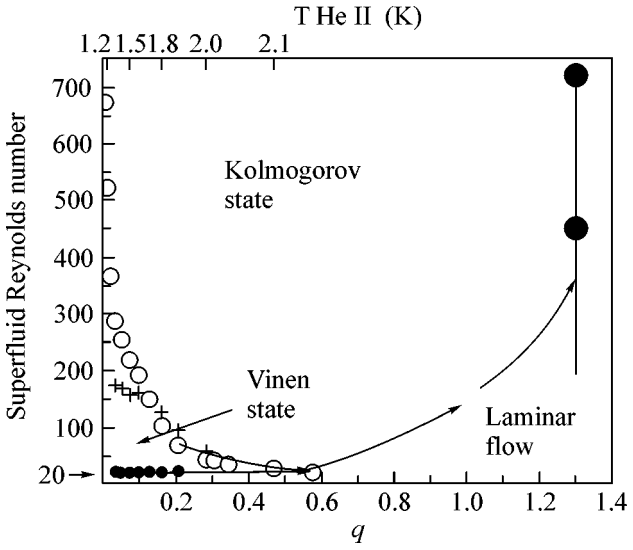

Fig. 1. The observed flow phase diagram of He II and ^{3}He–B superfluids in the unique frame of reference where the normal fluid is at rest. The abscissa q represents the inverse of the Reynolds number for a superflow (for convenience, the corresponding temperature in He II is indicated on the upper axis), while the ordinate Re_s represents the strength of circulation at the outer scale of the flow in units of κ. The small closed circles represent the onset of turbulent state I in apure superflow of He II when the motion of the normal fluid was inhibited by superleaks [26]; the crosses [17] and open circles [28] mark the transition from state I into state II for counterflowing He II. The two large closed points mark approximately the region where the onset of superfluid turbulence has been observed by various methods of vortex loop injection into rotating ^{3}He–B in the vortex-free Landau state (for $\Delta T \approx 0.05\, T_c$ around $0.6T/T_c$ at 29 bar; see Fig. 3 in [8]).

This result has been confirmed in the most recent theoretical work [7]. For higher counterflow velocities, an analysis based on Eq. (2) is likely to be valid and, therefore, a range of scales between the outer scale R and a minimum scale to which the cascade extends due to mutual friction occurs, and this minimum scale (it would be misleading to call it a dissipative scale, as dissipation occurs at all scales and is more important at large ones) still exceeds the quantum scale. Within these scales, the superfluid turbulence cannot be of the pure Kolmogorov type—the analysis [6, 7] clearly shows that, in such a case, there is no dissipation and nothing stops turbulent energy from propagating to smaller and smaller scales, eventually violating the above condition of circulation at the smallest scale exceeding κ. The energy spectrum thus must be of the k^{-3} type, or at least of the mutual friction modulated $k^{-5/3}$ type (see Eq. (28) in [7]). We therefore have large superfluid eddies that strongly interact via mutual friction with the normal fluid. So far, we have considered the theoretical approach when the normal fluid is strictly at rest, but in He II, this will most likely be violated and the normal fluid will be driven into a turbulent state as well.[6] In a steady counterflow, the coupled turbulence similar to the towed grid coupled turbulence [19] is unlikely, as the big superfluid and normal eddies are on average taken apart by the counterflow velocity. The situation changes, however, when the heater that generates the counterflow is turned off and the turbulence decays. Large normal and superfluid eddies can match each other, and there will be, therefore, no energy loss by mutual friction at large scales. As a result, the low-k part of the spectrum will change from the k^{-3} type to a classical $k^{-5/3}$ Kolmogorov type. We believe that this is the reason why the so-called "anomalous" decay of counterflow turbulence in He II was observed in the pioneering work of Vinen [12] and later by Schwarz and Rosen [20]. In our own decay experiments [21], we have observed that the temperature gradient along the counterflow channel decays very fast when the heater is switched off; thus, the flow can be considered as isothermal when the second sound decay measurement is being performed [23]. We therefore expect that the decays of high-Re_s counterflow turbulence and grid-generated He-II turbulence ought to display the same character. And indeed, it was clearly shown in experiments that, for both towed grid-generated He-II turbulence [16] and high-Re_s counterflow turbulence [21], most of the decay[7] of the vortex line density displays the same $t^{-3/2}$ power law. This decay law follows from the spectral decay model [16] based on the existence of the Kolmogorov 3D energy spectrum, which was directly shown by Maurer and Tabeling [24] to be present in classically generated ^{4}He turbulence both above and below the lambda point.

The crossover to superfluid turbulence state II has been observed in channels with both circular and square cross sections, but not in narrow channels with high-aspect-ratio rectangular cross sections [25]. Naturally, the transition cannot take place if the size of the sample intervenes. If some dimension of the channel is too small, its physical size limits the size of eddies.

There are many experimental data that can be used in order to probe the existence of the phase diagram (see Fig. 1) suggested by Volovik [3, 4]. The recent experiment of Finne *et al.* [8] provides evidence for a velocity-independent transition from a laminar to a turbulent-flow regime in rotating ^{3}He–B, where values of q of order unity are experimentally easily accessible.

In He II, these large values of q occur very close to the lambda point, where, to our knowledge, no reliable measurements exist that can be considered in the frame of reference of the normal fluid. On the other hand, there is ample experimental data on counterflow He-II turbulence at lower temperatures. However, the data on the transition into superfluid state I (the Vinen state) in

[6] That the normal fluid is likely turbulent in state II of the counterflow He-II turbulence is independently supported by the stability analysis of Melotte and Barenghi [22].

[7] After the energy-containing length scale becomes saturated by the size of the channel [16].

tubes and capillaries of various sizes cannot be reliably used here, as it is believed that, below this threshold, the viscous normal fluid possesses a velocity profile similar to a flow of ordinary viscous flow in a pipe. A unique frame of reference is not, therefore, provided by the normal fluid. However, Baehr *et al.* [26] studied the transition from dissipationless superflow to homogeneous superfluid turbulence, when both ends of the pipe were blocked by superleaks and the normal fluid inside the pipe thus remained stationary (at least, on average), thereby providing this unique frame of reference. These data, spanning the temperature range 1.3 K < T < 1.9 K, mark the transition from laminar flow to the Vinen state (state I) shown in Fig. 1.

That the existence of the normal fluid reference frame is important can be demonstrated using the different set of data of Baehr and Tough [27], which was obtained with an essentially identical setup but for flows where, at fixed temperature, the normal and superfluid velocities can be varied independently. If the normal fluid flow profile were flat, one would expect that the critical counterflow velocity for transition into turbulent state I, simply as a consequence of the Galilean invariance, stays unchanged. This does not happen, as the observed critical counterflow velocity increases with the imposed averaged normal fluid velocity, supposedly due to the fact that its flow profile is not flat.

Various counterflow experiments clearly display the transition from state I (Vinen) to state II (Kolmogorov): the signature is pronounced on temperature and pressure difference versus heat-input dependences. We use here the data of Ladner, Childers, and Tough [17] (their Table 1), assuming that, in state I, the normal fluid profile is flat, again providing the unique frame of reference in which the normal fluid is at rest. Let us point out that this transition to a different flow regime is accompanied by a pronounced increase in fluctuations [18], which is characteristic of phase transitions. The data [17] also clearly show that, upon increasing the temperature, the difference in counterflow velocity between state I and II transitions decreases and that around 2 K they become indistinguishable.

As another set of experimental data marking the state I–state II transition, we have used the thermal-conduction measurements made by Chase [28] of He II in tubes of various diameters. We have scanned the available experimental data and show in Fig. 2 that they collapse onto a single curve if Reynolds number scaling is applied. The open circles in Fig. 1 correspond to the onset of state II.

We emphasize that the procedure used to acquire the data points shown in the flow diagram is probably not very accurate for several reasons, such as different temperature scales or uncertainty in the values of q, and that more work is needed to map it out accurately. We believe, however, that the essential physics is displayed clearly and that Fig. 1 strongly supports the ideas

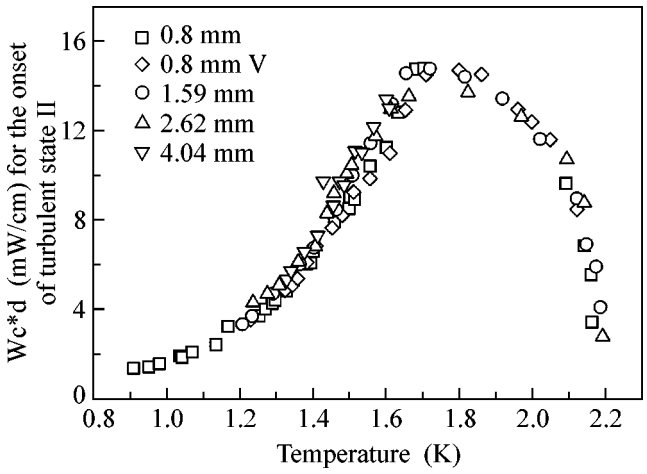

Fig. 2. Product of the critical heat input per unit area, Wc, times the inner diameter of the used tube, d, marking the onset of the turbulent state II versus temperature [28] (two different experimental methods have been used for a tube with d = 0.8 mm). The data obtained with tubes of various d as indicated collapse onto a single curve. Assuming that $U_{cf} \propto Wc$, these sets of data demonstrate that the onset of turbulent state II occurs at any temperature at a critical value of Re_s that is shown in Fig. 1.

underlying the physical problem of superfluid turbulence.

Let us comment here on the apparent disagreement in the zero-temperature limit between this phase flow diagram (Vinen state preferred for any finite Re_s) and the computer simulations of Araki *et al.* [29], which strongly indicate the presence of Kolmogorov scaling. Although these simulations are performed in the zero-temperature limit in the sense that there is no normal fluid, the simulation introduces a cutoff at the scale of the grid used for simulations, meaning that all vortex rings or loops smaller than this size are removed from the flow. This effectively introduces an artificial dissipative mechanism at a prescribed length scale. We believe that any dissipative mechanism acting at some small length scale (such as a Kelvin wave cascade with subsequent phonon emission [30]) leads to a Kolmogorov cascade in the continuum approximation, as the assumptions for it are only that there is a range of scales where dissipation is unimportant, that the form of the energy spectrum only depends on k, and that the total energy decay rate $\varepsilon = -dE/dt$ is independent of k. Dimensional analysis then leads to the energy spectrum of the Kolmogorov form. The physical mechanism of the dissipation is unimportant, so long as it acts only on small scales.

In practice, there could be a crossover from the mutual friction-dissipation regime into a different one that is probably based on vortex wave irradiation. The governing equation (Eq. (2)) will have to be altered accordingly, and a similar analysis repeated.

To conclude, we have shown that the extraordinary fluid properties of quantum fluids give rise to the flow diagram suggested by Volovik [3], which contains two distinctly different turbulent flow regimes. These can most likely be identified with the puzzling turbulent states I and II according to the classification scheme of Tough [1]. We emphasize that the energy spectrum in what is called the Kolmogorov state does not have the classical exponent –5/3.

Discussions with many colleagues, especially with D. Charalambous, P.V.E. McClintock, A.V. Gordeev, N.B. Kopnin, M. Krusius, W.F. Vinen, and G.E. Volovik are warmly acknowledged. This research was supported by the Grant Agency of the Czech Republic (grant no. GACR 202/02/0251).

REFERENCES

1. J. T. Tough, in *Progress in Low Temperature Physics* (North-Holland, Amsterdam, 1982), Vol. 8.
2. D. D. Awschalom and K. W. Schwarz, Phys. Rev. Lett. **52**, 49 (1984).
3. G. E. Volovik, JETP Lett. **78**, 533 (2003).
4. G. E. Volovik, cond-mat/0402035.
5. E. B. Sonin, Rev. Mod. Phys. **59**, 87 (1987).
6. W. F. Vinen, Phys. Rev. B (in press).
7. V. S. L'vov, S. V. Nazarenko, and G. E. Volovik, Pis'ma Zh. Éksp. Teor. Fiz. **80**, 535 (2004) [JETP Lett. **80**, 469 (2004)].
8. A. P. Finne *et al.*, Nature **424**, 1022 (2003).
9. R. J. Donnelly and C. F. Barenghi, J. Phys. Chem. Data **27**, 1217 (1998).
10. T. D. C. Bevan *et al.*, J. Low Temp. Phys. **109**, 423 (1997).
11. L. Skrbek, J. J. Niemela, and K. R. Sreenivasan, Phys. Rev. E **64**, 067301 (2001).
12. H. E. Hall and W. F. Vinen, Proc. R. Soc. London, Ser. A **238**, 204 (1956); Proc. R. Soc. London, Ser. A **238**, 205 (1956); W. F. Vinen, Proc. R. Soc. London, Ser. A **240**, 114 (1957); Proc. R. Soc. London, Ser. A **240**, 128 (1957); Proc. R. Soc. London, Ser. A **242**, 489 (1957).
13. K. W. Schwarz, Phys. Rev. B **38**, 2398 (1988).
14. D. D. Awschalom, F. P. Milliken, and K. W. Schwarz, Phys. Rev. Lett. **53**, 1372 (1984).
15. F. P. Milliken and K. W. Schwarz, Phys. Rev. Lett. **48**, 1204 (1982).
16. L. Skrbek, J. J. Niemela, and R. J. Donnelly, Phys. Rev. Lett. **85**, 2973 (2000).
17. D. R. Ladner, R. K. Childers, and J. T. Tough, Phys. Rev. B **13**, 2918 (1976).
18. C. P. Lorenson, D. Griswold, V. U. Nayak, and J. T. Tough, Phys. Rev. Lett. **55**, 1494 (1985).
19. W. F. Vinen and J. J. Niemela, J. Low Temp. Phys. **128**, 167 (2002).
20. K. W. Schwarz and J. R. Rozen, Phys. Rev. Lett. **66**, 1898 (1991); Phys. Rev. B **44**, 7563 (1991).
21. L. Skrbek, A. V. Gordeev, and F. Soukup, Phys. Rev. E **67**, 047302 (2003).
22. D. J. Melotte and C. F. Barenghi, Phys. Rev. Lett. **80**, 4181 (1998).
23. A. V. Gordeev, T. V. Chagovets, F. Soukup, and L. Skrbek, J. Low. Temp. Phys. (in press).
24. J. Maurer and P. Tabeling, Europhys. Lett. **43**, 29 (1998).
25. C. P. Lorenson, D. Griswold, V. U. Nayak, and J. T. Tough, Phys. Rev. Lett. **55**, 1494 (1985).
26. M. L. Baehr, L. B. Opatowsky, and J. T. Tough, Phys. Rev. Lett. **51**, 2295 (1983).
27. M. L. Baehr and J. T. Tough, Phys. Rev. Lett. **53**, 1669 (1984).
28. C. E. Chase, Phys. Rev. **127**, 361 (1962); Phys. Rev. **131**, 1898 (1963).
29. T. Araki, M. Tsubota, and S. K. Nemirovskii, Phys. Rev. Lett. **89**, 145301 (2002).
30. W. F. Vinen, Phys. Rev. B **61**, 1410 (2000).

JETP Letters, Vol. 80, No. 7, 2004, pp. 479–483. From Pis'ma v Zhurnal Éksperimental'noĭ i Teoreticheskoĭ Fiziki, Vol. 80, No. 7, 2004, pp. 546–550.

Energy Spectra of Developed Superfluid Turbulence¶

V. S. L'vov[1, *], S. V. Nazarenko[2, **], and G. E. Volovik[3, 4, *]**

[1] *Department of Chemical Physics, The Weizmann Institute of Science, 76100 Rehovot, Israel*
[2] *University of Warwick, Mathematics Institute, CV4 7AL Coventry, United Kingdom*
[3] *Low Temperature Laboratory, Helsinki University of Technology, FIN-02015 HUT, Finland*
[4] *Landau Institute for Theoretical Physics, Russian Academy of Sciences, Moscow, 117940 Russia*
**e-mail: Victor.Lvov@Weizmann.ac.il (http://lvov.weizmann.ac.il)*
***e-mail: snazar@maths.warwick.ac.uk (http://www.maths.warwick.ac.uk/~snazar)*
****e-mail: Volovik@boojum.hut.fi*
Received August 27, 2004

Turbulence spectra in superfluids are modified by the nonlinear energy dissipation caused by the mutual friction between quantized vortices and the normal component of the liquid. We have found a new state of fully developed turbulence, which occurs in some range of two Reynolds parameters characterizing the superfluid flow. This state displays both the Kolmogorov–Obukhov 5/3-scaling law $E_k \propto k^{-5/3}$ and a new "3-scaling law" $E_k \propto k^{-3}$, each in a well-separated range of k. *© 2004 MAIK "Nauka/Interperiodica".*

PACS numbers: 43.37.+q; 47.32.Cc; 67.40.Vs; 67.57.Fg

A superfluid consists of mutually penetrating components—a viscous normal component and one or several frictionless superfluid components. This explains why different types of turbulent motion are possible depending on whether the normal and the superfluid components move together or separately. Here, we are interested in the simplest case, in which the dynamics of the normal component can be neglected. This occurs, for example, in the superfluid phases of ^{3}He, where the normal component is so viscous that it is practically clamped to the container walls. The role of the normal component in this case is to provide the preferred heat-bath reference frame, in which the normal component, and thus the heat bath, are at rest. Dissipation takes place when the vortices move with respect to this reference frame. Turbulence in such a superfluid component with the normal component at rest will be called here superfluid turbulence.

Recent experiments on ^{3}He–B [1] demonstrated that the fate of a few vortices injected into a rapidly moving superfluid depends on a dimensionless intrinsic temperature-dependent parameter q rather than on the flow velocity. At $q \sim 1$, a rather sharp transition is observed between laminar evolution of the injected vortices and a turbulent many-vortex state of the whole superfluid. This adds a new twist to the general theory of turbulence in superfluids that was developed by Vinen [2, 3] and others. Attempts to modify the theory in order to incorporate the new phenomenon have been made in [4–6].

In this letter, we describe how the celebrated Kolmogorov–Obukhov 5/3-law for the turbulent energy spectrum in a normal fluid, $E_k \propto k^{-5/3}$, is modified in the superfluid turbulence, thus giving rise to the much steeper decrease $E_k \propto k^{-3}$.

As a starting point, we utilize a coarse-grained hydrodynamic equation for the superfluid dynamics with distributed vortices. In this equation, the parameter q characterizes the friction force between the superfluid and the normal components of the liquid, which is mediated by quantized vortices. According to this equation, turbulence develops only if the friction is relatively small compared to the inertial term, i.e., when $q < 1$. Here, we will study the case of developed turbulence, which must occur at $q \ll 1$.

An important feature of superfluid turbulence is that the vorticity of the superfluid component is quantized in terms of the elementary circulation quantum κ (in ^{3}He–B, $\kappa = \pi\hbar/m$, where m is the mass of a ^{3}He atom). Thus, superfluid turbulence is the chaotic motion of well-determined and well-separated vortex filaments [3]. Using this as a starting point, we can simulate the main ingredients of classical turbulence—the chaotic dynamics of the vortex degrees of freedom of the liquid. However, to make the analogy useful for classical turbulence, one must choose the regime described by hydrodynamic equations that are valid at length scales above the intervortex distance, the latter being a microscopic cutoff similar to the interatomic distance in conventional hydrodynamics. The coarse-grained hydrodynamic equation for the superfluid component is obtained from the Euler equation for the superfluid

¶ This article was submitted by the authors in English.

velocity $\mathbf{v} \equiv \mathbf{v}_s$ after averaging over the vortex lines (see review [7]):

$$\frac{\partial \mathbf{v}}{\partial t} + (\mathbf{v} \cdot \nabla)\mathbf{v} + \nabla\mu = \mathbf{D}, \quad (1)$$

where μ is the chemical potential and $\mathbf{D}$ describes the mutual friction:

$$\mathbf{D} = -\alpha'(\mathbf{v} - \mathbf{v}_n) \times \boldsymbol{\omega} + \alpha\hat{\boldsymbol{\omega}} \times [\boldsymbol{\omega} \times (\mathbf{v} - \mathbf{v}_n)]. \quad (2)$$

Here, $\boldsymbol{\omega} = \nabla \times \mathbf{v}$ is the superfluid vorticity, $\hat{\boldsymbol{\omega}} = \boldsymbol{\omega}/\omega$, $\mathbf{v}_n$ is the velocity of the normal component (which is fixed), and α' and α are dimensionless parameters describing the mutual friction between the superfluid and the normal components of the liquid mediated by the quantized vortices that transfer momenta from the superfluid to the normal subsystem. For a flow with vortices locally aligned with each other, these parameters enter the reactive and dissipative forces acting on a vortex line as it moves with respect to the normal component. For vortices in fermionic systems (superfluid ^{3}He and superconductors), such forces acting on a vortex were calculated by Kopnin [8], and they were measured in ^{3}He–B over a broad temperature range by Bevan *et al.* [9]. Here, we consider α' and α as phenomenological parameters, assuming the general case in which the quantized vortices are not aligned locally and, thus, the bare parameters are renormalized.

Further, we shall work in the reference frame in which $\mathbf{v}_n = 0$. In this frame, the nondissipative first term in Eq. (2) renormalizes the inertial term $\mathbf{v} \times \boldsymbol{\omega}$ in the left-hand side of Eq. (1) by the factor $1 - \alpha'$. The role of the Reynolds number in this hydrodynamics, i.e., the relative magnitude of the two nonlinear terms (the inertial and friction ones), is played by the velocity-independent ratio of dimensionless parameters $\mathrm{Re} = (1 - \alpha')/\alpha$, which was denoted in [1] as $\mathrm{Re} = 1/q$. The role of the parameter q as the inverse Reynolds number was demonstrated in the experiments described in [1], where it was shown that the turbulence develops only below some critical value of q (i.e., at $q < q_c \sim 1$).

Here, we are interested in the region of large Reynolds numbers, $\mathrm{Re} \gg 1$ ($q \ll 1$), where the inertial term is strongly dominating. In this region, one expects well-developed turbulence characterized by a Richardson–Kolmogorov-type cascade, which is modified due to the nonlinear dissipation. In ^{3}He–B, the range $q \ll 1$occurs at low temperatures, where $\alpha' \ll \alpha$, $q \approx \alpha$. Then, the mutual friction term in Eq. (2) can be written as

$$\mathbf{D} = q\boldsymbol{\omega} \times [\boldsymbol{\omega} \times \mathbf{v}]/|\omega|, \quad (3)$$

and we finally arrive at the hydrodynamic equation (Eq. (1)) whose left-hand side is the usual Euler equation with the nonlinear term, which is responsible for the energy cascade in the developed hydrodynamic turbulence, while the right-hand side contains the nonlinear dissipation term given by Eq. (3). We will describe this cascade in the simplest possible manner, using the differential form [10, 11] of the energy-transfer term in the energy budget equation (the more complicated version, using the second derivative [12], was used for superfluid turbulence by Vinen [6]):

$$\frac{\partial E_k}{\partial t} = -\mathcal{D}_k - \frac{\partial \varepsilon_k}{\partial k}. \quad (4)$$

Here, E_k is the one-dimensional density of the turbulent kinetic energy in the k space, defined such that the total energy density (in the physical space) E is given by

$$E \equiv \frac{1}{2}\langle |\mathbf{v}|^2 \rangle = \int dk E_k. \quad (5)$$

The dissipation of energy on the scale k is described by the $\mathcal{D}_k$ term on the right-hand side of Eq. (4), which will be clarified later. The idea of [10] is to relate E_k and ε_k in Eq. (4) in the spirit of Kolmogorov 1941 (K41) dimensional reasoning:

$$E_k = C\varepsilon_k^{2/3} k^{-5/3}. \quad (6)$$

Here, $C \simeq 1$ is the Kolmogorov dimensionless constant. In the absence of dissipation, Eq. (4) immediately produces the stationary solution $\varepsilon_k = \varepsilon$ with constant energy flux ε in the inertial interval of scales. Then, Eq. (6) turns into the Kolmogorov–Obukhov 5/3-law for E_k:

$$E_k = C\varepsilon^{2/3} k^{-5/3}. \quad (7)$$

The goal of this letter is to describe a possible modification of the scaling exponents in E_k due to form (3) of the dissipation term, which is different than in the Navier–Stokes equation. The energy-balance equation in the differential approximation (Eq. (4)) is just an adequate tool for this study: it is as simple as possible, but not excessively. A more accurate integral representation for the energy-transfer term gives exactly the same results for the scaling exponents, because they arise from the power counting. Clearly, approximation (4) does not accurately control the numerical prefactors and the exact functional form of the possible crossover region, but these are not important for the questions we aim to study here.

Within the same level of accuracy, we can simplify the vectorial structure of the dissipation term $\mathbf{D}$ and average Eq. (3) over the directions of the vorticity $\boldsymbol{\omega}$ (at fixed direction of $\mathbf{v}$):

$$\mathbf{D} \longrightarrow \langle \mathbf{D} \rangle_{\boldsymbol{\omega}/|\omega|} = -\frac{2}{3} q|\omega|\mathbf{v} \longrightarrow q|\omega|\mathbf{v}. \quad (8)$$

Again, we are not bothered by the numbers and, therefore, have skipped for simplicity the factor 2/3 in the Eq. (8). Notice that vorticity in hydrodynamic turbulence is usually dominated by the k eddies (i.e., motions on the scale $\sim 1/k$) with the largest characteristic wavevector $k_{\max}$. These eddies have the smallest turnover time $\tau_{\min}$ that is of the order of their decorrelation time. One can show that the main contribution to the velocity (not vorticity) in the equation for the dissipa-

tion of the k eddies, $\mathcal{D}_k$, with the intermediate wavevectors k, $1/R < k \ll k_{\max}$, is dominated by the k' eddies with $k' \sim k$. Because the turnover time of these eddies $\tau_{k'} \gg \tau_{\min}$, we can think of $|\omega|$ in Eq. (8) on the time intervals of interest ($\tau_{\min} \ll \tau \ll \tau_{k'}$) as a self-averaging quantity, because it is almost uncorrelated with the velocity $\mathbf{v}$, which can be treated as dynamical variable. In this study, this allows us to neglect in Eq. (8) the fluctuating part of $|\omega|$ and to replace $|\omega|$ by its mean value. In this approximation, Eq. (8) takes a very simple form:

$$\mathbf{D} = -\Gamma\mathbf{v}, \quad \Gamma \equiv q\omega_0, \quad \omega_0 \equiv \langle|\omega|\rangle. \tag{9}$$

From Eq. (9), one easily finds that

$$\mathcal{D}_k = \Gamma E_k, \tag{10}$$

and the balance equation (Eq. (4)) in the steady state finally takes the form

$$\frac{\partial \varepsilon_k}{\partial k} = -2\Gamma\varepsilon_k^{2/3}k^{-5/3}, \tag{11}$$

in which, for simplicity, we have put $C = 1$, because, in our simple approach, we are not controlling numbers of the order of unity.

Let us analyze the solutions of Eq. (11) that arise in the presence of a fixed energy influx $\epsilon_k = \epsilon_+$ at $k = 1/R$ into the turbulent system. Hereafter, R is the outer scale of turbulence that is of the order of the radius of the cryostat. In terms of the dimensionless variables $p = kR$, $f_p = \epsilon_p/\epsilon_+$, $\gamma = \Gamma R/V$, and $V = (\epsilon_+ R)^{1/3}$, we have

$$\frac{\partial f_p}{\partial p} = -2\gamma f_p^{2/3} p^{-5/3}. \tag{12}$$

The solution to this, with the boundary condition $f|_{p=1} = 1$, is

$$f_p^{1/3} = \gamma p^{-2/3} + 1 - \gamma, \tag{13}$$

or, in terms of the dimensional energy spectrum,

$$E_k = \frac{V^2}{k(kR)^{2/3}}\left[1 + \frac{\gamma}{(kR)^{2/3}} - \gamma\right]^2. \tag{14}$$

Then, expressing the mean vorticity through this energy spectrum, one obtains the closed equation for the parameter γ:

$$\Gamma = \gamma V/R = q\omega_0(\gamma), \tag{15}$$

which manifests the existence of several different regimes of turbulence. We consider first the case in which the resulting $\gamma < 1$ and Eq. (14) can be rewritten as

$$E_k = \frac{V^2\gamma^2}{R^2k^{5/3}}\left[\frac{1}{k^{2/3}} + \frac{1}{k_{\rm cr}^{2/3}}\right]^2, \tag{16}$$

where

$$k_{\rm cr} \equiv \frac{\gamma^{3/2}}{(1-\gamma)^{3/2}R} \tag{17}$$

is a crossover wavenumber separating two different scaling ranges. For $k \gg k_{\rm cr}$, we have the K41 scaling, in which the dissipation is negligible and the energy flux is approximately constant:

$$E_k = \frac{V^2(1-\gamma)^2}{R^{2/3}k^{5/3}}. \tag{18}$$

This equation can be rewritten in the traditional form (Eq. (7))

$$E_k \simeq \varepsilon_\infty^{2/3}k^{-5/3}, \tag{19}$$

in which the energy flux ε_∞ for $k > k_{\rm cr}$ due to the mutual friction can be much smaller than the energy influx ε_+ into the turbulent system:

$$\varepsilon_\infty = \varepsilon_+(1-\gamma)^3 < \varepsilon_+. \tag{20}$$

In order to see how ε_k decreases toward large k, approaching ε_∞ at $k \sim k_{\rm cr}$, we consider the region $k \ll k_{\rm cr}$. In this region, Eqs. (13) and (14) yield

$$\varepsilon_k = \frac{\varepsilon_+}{(kR)^2}, \quad E_k = \frac{V^2\gamma^2}{R^2k^3}. \tag{21}$$

Thus, the rate of the energy dissipation, which is proportional to E_k, decreases toward large k and becomes insignificant at $k \gg k_{\rm cr}$. In this region, $\varepsilon_k \simeq \varepsilon_\infty$ and one has the K41 scaling (Eq. (19)).

Notice that the k^{-3} spectrum (Eq. (21)) corresponds to the balance between the energy flux and the dissipation due to the mutual friction. This follows from the energy balance equation (Eq. (11)), but it can also be directly understood in the r representation. Indeed, the energy flux in the scale r can be evaluated as V_r^3/r, while the energy dissipation is ΓV_r^2. Here, V_r is the characteristic velocity of eddies on the scale r, i.e., the velocity increment across the separation r. The balance yields $V_r \simeq \Gamma r$, i.e., the energy of the r eddies $V_r^2 \propto r^2$. In the k representation, this gives the one-dimensional energy spectrum $E_k \propto k^{-3}$, i.e., the 3-law (Eq. (21)).

The K41 scaling ends by a cutoff at a "microscopic" scale $1/k_*$, at which circulation in the k_* eddy reaches the circulation quantum κ:

$$\kappa \sim \frac{v_*}{k_*} = \frac{RV(1-\gamma)}{(k_*R)^{4/3}}, \tag{22}$$

i.e.,

$$(k_*R)^{4/3} \sim \mathcal{N}^2(1-\gamma), \tag{23}$$

where $\mathcal{N}^2 = RV/\kappa$ is the "quantum Reynolds number" [1]. The parameter $\mathcal{N}$ can be considered as the ratio of R to the mean intervortex distance. Clearly, with the classical approach to the problem, we can consider only the limit $\mathcal{N} \gg 1$.

Now, we can clarify the equation of self-consistency (Eq. (15)) for γ. Estimating ω_0 as follows

$$\omega_0^2 = \langle|\omega|\rangle^2 \simeq \langle|\omega|^2\rangle \simeq \int_{1/R}^{k_*} dk k^2 E_k,$$

and using Eqs. (15) and (16), one gets

$$1 \simeq q^2 \int_{1/R}^{k_*} dk k^{1/3}\left[\frac{1}{k^{2/3}} + \frac{1}{k_{cr}^{2/3}}\right]^2. \quad (24)$$

Together with Eqs. (17) and (23), which relate k_* and k_{cr} to γ and $\mathcal{N}$, this equation allows one to find γ, k_*, and k_{cr} in terms of the "external parameters" of the problem, q and $\mathcal{N}$. As we pointed out, the classical regime of developed turbulence corresponds to the region $q \ll 1$, $\mathcal{N} \gg 1$.

We consider first the case in which the inner (quantum) scale of turbulence is well separated from the crossover scale: $k_* \gg k_{cr}$. Then, the main contribution to the integral in Eq. (24) comes from the region $k \gg k_{cr}$, where the second term in the integral dominates. Therefore, Eq. (24) gives the relationship

$$k_{cr} \simeq q^{3/2} k_*, \quad (25)$$

which, together with Eqs. (17) and (23), yields an equation for γ:

$$q\mathcal{N} \simeq \gamma/(1-\gamma)^{3/2}. \quad (26)$$

For $q\mathcal{N} \ll 1$, the solution is $\gamma \simeq q\mathcal{N} < 1$, which gives $Rk_{cr} \simeq (q\mathcal{N})^{3/2} < 1$ and

$$E_k \simeq \frac{V^2}{k(kR)^{2/3}}\left[1 - 2q\mathcal{N}\left(1 - \frac{1}{(kR)^{2/3}}\right)\right], \quad (27)$$

$$Rk_* \simeq \mathcal{N}^{3/2} \gg 1 \text{ for } q\mathcal{N} \ll 1.$$

This means that, for $q\mathcal{N} \ll 1$ in the entire inertial interval $1/R < k < k_*$, one has the usual Kolmogorov–Obukhov spectrum with the small (on the order of $q\mathcal{N}$) negative corrections. In other words, at $q\mathcal{N} \ll 1$ the mutual friction has a negligible effect on the statistics of turbulence.

The situation is different in the region $q\mathcal{N} \gg 1$. In this case, the solution to Eq. (26) is $1 - \gamma \simeq (q\mathcal{N})^{-2/3} \ll 1$ and, instead of Eq. (27), one has

$$E_k \simeq \frac{V^2}{R^2 k^{5/3}}\left[\frac{1}{k^{2/3}} + \frac{1}{k_{cr}^{2/3}}\right]^2, \text{ for } q\mathcal{N} \gg 1, \quad (28)$$

$$k_{cr}R \simeq q\mathcal{N}, \quad k_*R \simeq \mathcal{N}/q^{1/2} \gg k_{cr}R.$$

One sees that the pumping and the crossover scales are well separated if $q\mathcal{N} \gg 1$. Under this condition, the quantum cutoff scale is also well separated.

Up to now, we have assumed that the second term in […] in integral (24) is dominant. In the opposite case, instead of Eqs. (25) and (26), one has

$$k_*R \simeq \exp\left(\frac{1}{q^2}\right), \quad k_{cr}R \simeq \mathcal{N}^3 \exp\left(-\frac{2}{q^2}\right). \quad (29)$$

Taking into account that we are considering solutions in which the first term in […] in integral (24) is dominant, we have to take $k_{cr} > k_*$, which gives $\mathcal{N} > \exp(1/q^2)$. Therefore, the range of parameters in which the two-cascade regime (Eq. (28)) occurs is

$$1/q < \mathcal{N} < \exp(1/q^2). \quad (30)$$

An important feature of this solution is that both the energy spectrum E_k and the spectrum of the flow dissipation ε_k are concentrated at the largest length scale R, whereas the dissipation is mediated by the vorticity ω_0 concentrated at the smallest (microscopic) scale $1/k_*$. Therefore, the energy balance between the Kolmogorov cascade and the energy dissipation must already occur for the largest eddies. This gives the condition [5]

$$\frac{V^3}{R} = \Gamma V^2. \quad (31)$$

This means that, in this turbulent state, the mean vorticity is $\omega_0 = \Gamma/q = U/qR$. If $q\mathcal{N} \gg 1$, one has γ close to 1, and, thus, our double-cascade solution (Eq. (28)) satisfies the large-scale balance (Eq. (31)).

At $q\mathcal{N} \sim 1$, one has $k_{cr} = 1/R$; i.e., the region of the k^{-3} spectrum shrinks. At $q\mathcal{N} \ll 1$, the parameter γ deviates from unity: $\gamma \simeq q\mathcal{N}$. Here, two scenarios are possible. In the first one, we have solution (27), in which the mutual friction is unessential and thus is unable to compensate the Kolmogorov cascade. When the intervortex distance scale is reached, the Kolmogorov energy cascade is then transformed to the Kelvin wave cascade [3] for the isolated vortices. In the second scenario, suggested in [5, 13], at $q\mathcal{N} \ll 1$ the turbulent state is completely reconstructed, and the so-called Vinen state emerges. This state, introduced by Vinen [14] and then by Schwarz [15], contains a single scale $r = \kappa/V$ and thus no cascade.

Another interesting case to consider is $\gamma > 1$, when Eq. (14) for E_k can be rewritten as follows:

$$E_k = \frac{V^2\gamma^2}{R^2 k^{5/3}}\left[\frac{1}{k^{2/3}} - \frac{1}{\tilde{k}_{cr}^{2/3}}\right]^2, \quad (32)$$

where

$$\tilde{k}_{cr} = \frac{\gamma^{3/2}}{(\gamma-1)^{3/2}R}. \quad (33)$$

Here, the Kolmogorov cascade has stopped already at the scale $\tilde{k}_{cr}$, and the equation for γ reads

$$1 \simeq q\sqrt{\frac{3}{2}\ln\frac{\gamma}{(\gamma-1)}}. \quad (34)$$

The solution satisfying the large-scale energy balance $\gamma \simeq 1$ is

$$\gamma - 1 \simeq \exp(-2/3q^2). \quad (35)$$

This solution is self-consistent and does not require the microscopic-scale cutoff if the circulation at the scale $\tilde{k}_{cr}$ is big enough, i.e., if $v_{cr}/\tilde{k}_{cr} \gg \kappa$. This occurs, however, at very large counterflow $\mathcal{N} \gg \exp(1/q^2)$. We think that this solution is unstable. Indeed, let us consider a perturbation of this spectrum in the form of cutting off its tail. This will lead to a reduction in the dissipation rate, so that the subsequent evolution will build a K41 constant-flux tail rather than restore the k^{-3} scaling. The K41 tail will strengthen until its contribution to the friction will restore the energy balance. Thus, the resulting new steady state will have the K41 part, i.e., will be of the first kind.

A summary of the different regimes (without the possible Vinen state) is shown in the table.

Now, let us compare our results for the superfluid turbulence with earlier works. In [5, 13], the effect of the mutual friction on the high-momentum tail was overestimated, which led to an incorrect result for the spectrum of dissipation at high momenta. However, some general features suggested in [5] remain the same. In particular, there are different regimes of the superfluid turbulence. The transition line between two turbulent regimes, $q\mathcal{N} \simeq 1$, was correctly determined in [5, 13], as was the vorticity in the regime of cascade, $\omega_0 = V/qR$. Recently, Vinen [6] used a diffusion-equation model, which is similar in spirit to the model used in our letter and, perhaps, even better because it properly accounts not only for the cascade states but also for the thermodynamic equilibria. However, this equation is harder to solve analytically, and thus Vinen used numerical simulations. His qualitative and numerical results are consistent with our analytic solution.

In conclusion, we have discussed the spectrum of the superfluid turbulence governed by the nonlinear energy dissipation due to the mutual friction between the vortices and the normal component of the liquid, which remains at rest. We found that, in agreement with [1, 5], the flow states are determined by two dimensionless parameters: the velocity-independent Reynolds number $\mathrm{Re} = 1/q$, which separates the laminar and turbulent states, and the quantum velocity-dependent parameter $\mathcal{N} = \sqrt{VR/\kappa}$, which contains the quantum of circulation around the quantum vortices κ and which determines the transition, or crossover, between different regimes of superfluid turbulence. In some region of the $(q, \mathcal{N})$ plane, we found a turbulent state with a well-defined Richardson-type cascade. This state displays both the Kolmogorov–Obukhov 5/3-scaling law $E_k \propto k^{-5/3}$ and the new "3-scaling law" $E_k \propto k^{-3}$, each in a well-separated range of k. A possible connection of the phase diagram of the flow states to experimental observations is discussed in [16].

Scaling-range boundaries in the cases of weak, intermediate, and strong pumping

Intensity, $\mathcal{N}$	Crossover, $k_{cr}R$	Quantum cutoff, k_*R
$1 < \mathcal{N} < 1/q$	None, 5/3-scaling	$\mathcal{N}^{3/2}$
$1 < 1/q < \mathcal{N} < e^{1/q^2}$	$q\mathcal{N}$	$\mathcal{N}/\sqrt{q}$
$1 < e^{1/q^2} < \mathcal{N}$	None, 3-scaling	e^{1/q^2}

This work was completed as the result of collaboration during the workshop on "Turbulence and Vacuum Instability in Condensed Matter and Cosmology" that was organized in the framework of the ESF Program COSLAB. G.E.V. thanks V.V. Lebedev and W.F. Vinen for fruitful criticism. The work is supported by ULTI-4 and also in part by the Russian Foundation for Basic Research (project no. 02-02-16218) and the US–Israel Binational Science Foundation.

REFERENCES

1. A. P. Finne, T. Araki, R. Blaauwgeers, *et al.*, Nature **424**, 1022 (2003).
2. W. F. Vinen, Proc. R. Soc. London, Ser. A **242**, 493 (1957).
3. W. F. Vinen and J. J. Niemela, J. Low Temp. Phys. **128**, 167 (2002).
4. N. B. Kopnin, Phys. Rev. Lett. **92**, 135301 (2004).
5. G. E. Volovik, Pis'ma Zh. Éksp. Teor. Fiz. **78**, 1021 (2003) [JETP Lett. **78**, 533 (2003)].
6. W. F. Vinen (in press).
7. E. B. Sonin, Rev. Mod. Phys. **59**, 87 (1987).
8. N. B. Kopnin, *Theory of Nonequilibrium Superconductivity* (Clarendon Press, Oxford, 2001).
9. T. D. C. Bevan *et al.*, Nature **386**, 689 (1997); J. Low Temp. Phys. **109**, 423 (1997).
10. L. Kovasznay, J. Aeronaut. Sci. **15**, 745 (1947).
11. C. Leith, Phys. Fluids **10**, 1409 (1967); Phys. Fluids **11**, 1612 (1968).
12. C. Connaughton and S. Nazarenko, Phys. Rev. Lett. **92**, 044501 (2004); J.-P. Laval, B. Dubrulle, and S. Nazarenko, Phys. Fluids **13**, 1995 (2001).
13. G. E. Volovik, Prepared for *Proceedings of Conference on Quantum Phenomena at Low Temperatures, Lammi, Finland, 2004*; J. Low Temp. Phys. (in press); cond-mat/0402035.
14. W. F. Vinen, Proc. R. Soc. London, Ser. A **242**, 489 (1957).
15. K. W. Schwarz, Phys. Rev. B **38**, 2398 (1988).
16. L. Skrbek, Pis'ma Zh. Éksp. Teor. Fiz. **80**, 540 (2004) [JETP Lett. **80**, 474 (2004)].

JETP Letters, Vol. 80, No. 7, 2004, pp. 484–486. Translated from Pis'ma v Zhurnal Éksperimental'noĭ i Teoreticheskoĭ Fiziki, Vol. 80, No. 7, 2004, pp. 551–554.

Effect of Negative Acoustic Refraction in a One-Dimensional Phononic Crystal

O. S. Tarasenko, S. V. Tarasenko, and V. M. Yurchenko

Donetsk Physicotechnical Institute, National Academy of Sciences of Ukraine, Donetsk, 83114 Ukraine

Received August 16, 2004

A two-component thin-layer acoustic superlattice (one-dimensional phononic crystal), in which one of the layers of the superlattice period is near the proper ferroelastic phase transition, is considered. The necessary conditions under which a bulk elastic wave incident on the outer surface of the superlattice excites a refracted wave with negative acoustic refraction (at the fundamental or multiple frequency) have been determined. © *2004 MAIK "Nauka/Interperiodica".*

PACS numbers: 42.70.Qs; 68.35.–p; 68.65.–k

The conditions of the propagation and localization of elastic waves in acoustically continuous periodic media (phononic crystals) have been analyzed in numerous works, and the acoustics of phononic crystals is closely similar to the electrodynamics of photonic crystals. Nevertheless, the study of the dynamics of composite elastic media have been focused on the conditions of formation of absolute band gaps for bulk elastic waves [1].

In this work, we consider a one-dimensional phononic crystal and show that, if at least one of the elastic layers forming the elementary period of the superlattice structure is near the proper ferroelastic phase transition, such a composite medium can exhibit a number of new acoustic effects whose electromagnetic analogs have being actively investigated in the dynamics of photonic crystals [2, 3] with negative refraction indices. These effects have not yet been shown for phononic crystals and include negative acoustic refraction [i.e., group velocities of the incident and refracted elastic waves (at the fundamental or multiple frequency) lie on the same side of the normal to the interface between media—the tangential components of the group velocity of the incident and refracted waves differ in sign].

Let the spatial structure of the two-component superlattice under investigation coincide with that studied in [4]; i.e., it is translation invariant along the normal to the interface between the layers with thicknesses d_1 and d_2 ($D = d_1 + d_2$ is the elementary period of the structure). For clarity and simplicity of calculations, we assume that the first and second media are elastically isotropic and have the same Lamé constants $\lambda_1 = \lambda_2 = \lambda$ and $\mu_1 = \mu_2 = \mu$ and densities $\rho_1 = \rho_2 = \rho$.

For a single-component proper ferroelastic phase transition with the symmetry group of the 222 paraphase, the thermodynamic potentials of the first and second media are represented in the form [5]

$$W_1 = \frac{\alpha}{2}\eta^2 + \gamma\eta u_{xy} + \frac{\lambda}{2}u_{ii}^2 + \mu u_{ik}^2 - \eta E_z,$$
$$W_2 = \frac{\lambda}{2}\tilde{u}_{ii}^2 + \mu\tilde{u}_{ik}^2, \quad (1)$$

respectively. Here, γ is the linear striction, $\alpha > 0$ is the uniaxial anisotropy constant, u_{ik} ($\tilde{u}_{ik}$) is the elastic strain tensor in the first (second) medium, and **E** is the electric field. Since the superlattice is assumed to be acoustically continuous, the corresponding system of elastic boundary conditions is represented in the form

$$\sigma_{ik}n_k = \tilde{\sigma}_{ik}n_k; \quad u_i = \tilde{u}_i; \quad \xi = -ND; -ND - d_1. \quad (2)$$

Here, σ_{ik} ($\tilde{\sigma}_{ik}$) is the elastic stress tensor in the first (second) medium; $N = 0, 1, \ldots$; and ξ is the coordinate along the normal **n** to the interface between the media. Since the second medium is assumed to be ideally conductive, the following condition is satisfied on both sides of each of the ferroelastic films (first medium):

$$E_\tau = 0; \quad \xi = -ND; -ND - d_1, \quad (3)$$

where τ is the unit vector along the direction of wave propagation in the layer plane. The features of the propagation of elastic waves in the superlattice "piezoelectric–ideal metal," where the natural degrees of freedom were disregarded ($\alpha \longrightarrow 0$), were analyzed in [6].

If the wavenumber $k_\perp$ and frequency ω of the elastic wave under consideration are such that the normal components $k_{\|1}$ and $k_{\|2}$ of the wave vectors of the bulk waves propagating in the first and second media, respectively, satisfy the inequalities

$$k_{\|1}d_1 \ll 1, \quad k_{\|2}d_2 \ll 1, \quad (4)$$

the elastic dynamics of such a thin-layer superlattice can be analyzed in the effective-medium approximation according to [7].

It follows from Eqs. (1)–(4) that the linear elastic dynamics of such an effectively spatially homogeneous medium is described by the set of effective elastic moduli $\bar{c}_{ik}$ satisfying the relation

$$\langle \sigma_{ik} \rangle = \bar{c}_{ik} \langle u_{ik} \rangle. \quad (5)$$

Here, $\langle A \rangle \equiv f_1 A_1 + f_2 A_2$, where $f_1 = d_1/D$ and $f_2 = d_2/D$, is the averaging of quantity A over the superlattice period D under conditions (2)–(4). This approach is widely used to analyze the polariton dynamics of thin-layer superlattices [8].

According to [7], the effective medium specified by Eqs. (1)–(5) has hexagonal symmetry, and, if the normal **n** to the interface between the layers coincides with one of the basic coordinate axes, $\bar{c}_{66}$ is the only modulus differing from the elastic-medium case (λ, μ):

$$\bar{c}_{66} \equiv \frac{\mu(\omega_0^2 + \omega_{me}^2 f_2 - \omega^2)}{(\omega_0^2 + \omega_{me}^2 - \omega^2)} \quad \text{for } \mathbf{n} \parallel Z, \quad (6)$$

$$\bar{c}_{66} \equiv \frac{\mu(\omega_0^2 - \omega^2)}{(\omega_0^2 + \omega_{me}^2 f_1 - \omega^2)} \quad \text{for } \mathbf{n} \parallel Y, \quad (7)$$

$$\bar{c}_{66} \equiv \frac{\mu(\omega_0^2 - \omega^2)}{(\omega_0^2 + \omega_{me}^2 f_1 - \omega^2)} \quad \text{for } \mathbf{n} \parallel X. \quad (8)$$

Let the superlattice under consideration fill the lower half-space ($\xi < 0$) and its outer surface ($\xi = 0$) have continuous acoustic contact with the homogeneous elastically isotropic half-space ($\xi > 0$), from which the bulk elastic wave with frequency ω and wavenumber $k_\perp$ is incident on the surface of the superlattice. In what follows, we consider only the case, where the normal to the incidence plane coincides with one of the basic coordinate axes. Therefore, elastic normal waves excited in the superlattice include waves polarized both in the incidence plane (quasi-longitudinal and quasi-transverse modes) and perpendicularly to it (*SH* wave). If $\mathbf{k} \in XZ$ or $\mathbf{k} \in YZ$, the quasi-longitudinal and quasi-transverse waves change into the longitudinal and transverse waves (*P* and *SV* waves), respectively.

As was already known [9], the kinematics of the reflected (refracted) normal wave with a given frequency ω and projection $k_\perp$ of its wave vector **k** onto the surface of the medium is determined by the structure of the section of its wave-vector surface (WVS) by the reflection (refraction) plane in *k* space. The radius vector of a point in such a section is collinear to the phase-velocity direction ($k_\perp$, $k_\parallel$), and the outer normal is directed along the group velocity of the excited normal mode $k_\parallel = k_\parallel(k_\perp, \omega)$ ($k_\parallel$ is the projection of the wave vector of the excited wave onto the normal to the interface between the media). Thus, there are the following four types of points of the WVS section that differ in the signs of the projections of the wave and group velocities onto both the interface between the media and the normal to the interface (we consider only the case, where the phase and group velocities of the refracted wave lie in one plane):

$$\begin{aligned} &A(k_\perp \partial\omega/\partial k_\perp > 0;\ k_\parallel \partial\omega/\partial k_\parallel > 0),\\ &B(k_\perp \partial\omega/\partial k_\perp > 0;\ k_\parallel \partial\omega/\partial k_\parallel < 0),\\ &C(k_\perp \partial\omega/\partial k_\perp < 0;\ k_\parallel \partial\omega/\partial k_\parallel > 0),\\ &D(k_\perp \partial\omega/\partial k_\perp < 0;\ k_\parallel \partial\omega/\partial k_\parallel < 0). \end{aligned} \quad (9)$$

The refracted wave must always satisfy the following two conditions. First, the tangential projections of the wave vectors of the incident ($k_{\perp i}$) and refracted ($k_{\perp r}$) waves at the interface between the media are equal to each other. Second, the group velocity of the refracted wave forms an acute angle with the inner normal to the interface between the media ($n\partial\omega/\partial k_r < 0$). Thus, negative refraction $k_{\perp r}\partial\omega/\partial k_{\perp r} < 0$ is principally possible only for points of the *C* and *D* types specified by Eqs. (9) of the WVS of the refracted wave.

According to Eqs. (6)–(9), negative acoustic refraction is possible for the refracted *SH* type wave if

$$\begin{aligned} &\bar{c}_{66} < 0; \quad \mathbf{n} \parallel Z \text{ and } \mathbf{k} \in XZ(\mathbf{u} \parallel Y)\\ &\text{or } \mathbf{k} \in YZ(\mathbf{u} \parallel X). \end{aligned} \quad (10)$$

In this case, the corresponding section of the WVS by the incidence plane has the form

$$k^2 = \omega^2/[s_t^2((\bar{c}_{66}/\mu)\sin^2\phi + \cos^2\phi)] > 0, \quad (11)$$

where $k_\parallel^2 + k_\perp^2 = k^2$, $\tan\phi \equiv k_\perp/k_\parallel$, and $s_t^2 = \mu/\rho$. If

$$\begin{aligned} &\bar{c}_{66} < 0; \quad \mathbf{n} \parallel X \text{ and } \mathbf{k} \in XZ(\mathbf{u} \parallel Y)\\ &\text{or } \mathbf{n} \parallel Y, \mathbf{k} \in YZ(\mathbf{u} \parallel X), \end{aligned} \quad (12)$$

then

$$k^2 = \omega^2/[s_t^2(\sin^2\phi + (\bar{c}_{66}/\mu)\cos^2\phi)] > 0, \quad (13)$$

and it follows from Eqs. (6)–(9) that the phase velocities of the incident and refracted *SH* waves lie on the same side of the inner normal to the interface between the media in this geometry, whereas the group velocity of the refracted shear wave satisfies the condition $k_\perp \partial\omega/\partial k_\perp > 0$; i.e., the effect of negative acoustic refraction is absent.

Negative acoustic refraction is possible not only when the refracted elastic wave is polarized orthogonally to the incidence plane (sagittal plane), but also when the refracted elastic wave is polarized in the incidence plane. This is possible in the model of the thin-layer superlattice under consideration if (001) is the normal to the incidence plane.

Let $\mathbf{n} \parallel X$ or $\mathbf{n} \parallel Y$. In this case, calculation using Eqs. (6)–(8) shows that the birefringence effect occurs in the thin-layer superlattice under consideration with no change in the branch. Both branches belong to the

same mode (have the same frequency ω, polarization, and wavenumber $k_\perp$) of the spectrum of normal elastic oscillations (quasi-transverse mode). The section of the corresponding WVS cavity by the incidence plane with the (001) normal is given by the relation

$$k^2 = \frac{A + \sqrt{A^2 - 4B}}{2B}\omega^2;$$
$$A = \lambda + 2\mu + \bar{c}_{66}, \quad (14)$$
$$B = (\lambda + 2\mu)\bar{c}_{66} + 0.25(2\lambda + 3\mu)(\mu - 2\bar{c}_{66})\sin^2 2\phi.$$

According to Eq. (14), negative acoustic refraction as specified by Eqs. (9) is possible for the given $k_\perp$ and ω values only for one of the branches of the refracted quasi-bulk wave if $k_\perp > k_*$ and

$$-(2\lambda + 3\mu)/2 < \bar{c}_{66} < 0 \quad (15)$$

or

$$\bar{c}_{66}(\omega) > \sqrt{\mu(2\lambda + 3\mu) + 0.25(3\lambda + 4\mu)^2} - 0.5(3\lambda + 4\mu). \quad (16)$$

Here, k_* is the $k_\perp$ value satisfying the relation $\partial k_\parallel/\partial k_\perp = 0$.

The effect of negative acoustic refraction is absent for the second branch of refracted quasi-transverse wave (14), which has the same polarization, frequency ω, and wavenumber $k_\perp$; i.e., $k_\perp \partial\omega/\partial k_\perp > 0$, and the phase velocities of the incident and refracted waves lie on the same side of the inner normal to the interface between the media.

It should be noted that the one-dimensional final-thickness phononic crystal focuses an acoustic wave incident on its outer surface if the bulk elastic wave generated by this wave inside the phononic crystal has the above effect of negative acoustic refraction. By analogy with photonic crystals [10], the above effect of negative acoustic refraction can be manifested in the nonlinear elastic dynamics of the one-dimensional phononic crystal particularly for the generation of the refracted wave with multiple harmonics. In particular, the *SH* wave incident on the surface of the superlattice, which is given by Eqs. (6)–(8) with frequency ω, has a tangential group-velocity component that differs in sign from the corresponding component of the refracted quasi-transverse wave (*SV* wave) with a frequency that is a multiple of the fundamental frequency: $m\omega$ ($m = 2, 3, \ldots$); i.e.,

$$\bar{c}_{66}(\omega) < 0 \quad (17)$$

if $\mathbf{n} \parallel Z$, $\mathbf{k} \in XZ$, and $\mathbf{u} \parallel Y$ (or $\mathbf{n} \parallel Z$, $\mathbf{k} \in YZ$, and $\mathbf{u} \parallel X$) for the *SH* wave.

Although the Gaussian curvature of the section of the WVS by the incidence plane is negative at a point satisfying the condition $k_{\perp i} = k_{\perp r}$ in all cases (9), this condition is not necessary. In particular, if the angle between the *Z* axis and the normal **n** to the interface between the layers in the incidence plane *XZ* is equal to ϕ_0 in the ferroelastic layer (first medium) of the period of the superlattice under consideration, it follows from Eqs. (3)–(6) that the section of the WVS of the *SH* shear wave with $\mathbf{k} \in XZ$ and $\mathbf{u} \parallel Y$ by this plane is described by the relation

$$k^2 = \omega^2/[s_t^2(c_2\sin^2\phi + c_3\sin 2\phi + c_1\cos^2\phi)] > 0, \quad (18)$$

where

$$c_1 = \frac{\omega_0^2 + \omega_{me}^2\cos^2\phi_0 - \omega^2}{\omega_0^2 + \omega_{me}^2[f_2\cos^2\phi_0 + f_1] - \omega^2};$$
$$c_2 = \frac{\omega_0^2 + \omega_{me}^2[f_2\cos^2\phi_0 + f_1\sin^2\phi_0] - \omega^2}{\omega_0^2 + \omega_{me}^2[f_2\cos^2\phi_0 + f_1] - \omega^2};$$
$$c_3 = \frac{0.5 f_1\omega_{me}^2\sin(2\phi_0)}{\omega_0^2 + \omega_{me}^2[f_2\cos^2\phi_0 + f_1] - \omega^2}.$$

Therefore, the negative acoustic refraction defined by Eqs. (9) occurs when $k_\perp < k_*$ even for $\bar{c}_{66} > 0$ (i.e., when the WVS is convex). However, the effect in this case is not mutual under the change $k_\perp \longrightarrow -k_\perp$ (the superlattice is also assumed to occupy the lower half-space $\xi < 0$).

It should be noted that, in addition to striction, other mechanisms can be responsible for negative curvature in the section of the WVS by the sagittal plane and, therefore, for negative acoustic refraction at the fundamental and multiple frequencies. Piezoelectric and piezomagnetic effects for the *SH* waves, as well as the anisotropy of the elastic properties for quasi-transverse elastic waves, are among these mechanisms.

An acoustically continuous magnetic superlattice (one-dimensional magnetic phononic crystal) can be used as a composite medium in which the above effects are possible.

REFERENCES

1. D. Bria and B. Djafari-Rouhani, Phys. Rev. E **66**, 056609 (2002).
2. V. G. Veselago, Usp. Fiz. Nauk **92**, 517 (1967) [Sov. Phys. Usp. **10**, 509 (1968)].
3. J. B. Pendry, A. J. Holden, W. J. Stewart, and I. Youngs, Phys. Rev. Lett. **76**, 4773 (1996).
4. R. E. Camley, B. Djafari-Rouhani, L. Dobrzynski, and A. Maradudin, Phys. Rev. B **27**, 7318 (1983).
5. B. A. Strukov and A. P. Levanyuk, *Physical Principles of Ferroelectric Phenomena in Crystals* (Nauka, Moscow, 1983) [in Russian].
6. V. I. Al'shits, A. S. Gorkunova, and A. L. Shuvalov, Zh. Éksp. Teor. Fiz. **110**, 924 (1996) [JETP **83**, 509 (1996)].
7. S. M. Rytov, Akust. Zh. **2**, 72 (1956) [Sov. Phys. Acoust. **2**, 68 (1956)].
8. K. Abraha and D. R. Tilley, Surf. Sci. Rep. **24**, 129 (1996).
9. M. K. Balakirev and I. A. Gilinskiĭ, *Waves in Piezoelectric Crystals* (Nauka, Novosibirsk, 1982) [in Russian].
10. V. M. Agranovich, Y. R. Shen, R. H. Baughman, and A. A. Zakhidov, Phys. Rev. B **69**, 165112 (2004).

Translated by R. Tyapaev

JETP Letters, Vol. 80, No. 7, 2004, pp. 487–490. Translated from Pis'ma v Zhurnal Éksperimental'noĭ i Teoreticheskoĭ Fiziki, Vol. 80, No. 7, 2004, pp. 555–559.

Solid-State Synthesis in Ni/Fe/MgO(001) Epitaxial Thin Films

V. G. Myagkov[1, *], O. A. Bayukov[1], L. E. Bykova[1], V. S. Zhigalov[1], and G. N. Bondarenko[2]

[1] *Kirensky Institute of Physics, Siberian Division, Russian Academy of Sciences, Akademgorodok, Krasnoyarsk, 660036 Russia*

* *e-mail: miagkov@iph.krasn.ru*

[2] *Institute of Chemistry and Chemical Technology, Siberian Division, Russian Academy of Sciences, Krasnoyarsk, 660036 Russia*

Received June 27, 2004; in final form, August 16, 2004

Solid-state synthesis in Ni/Fe/MgO(001) bilayer epitaxial thin films has been studied experimentally. The phase sequence Fe/Ni $\longrightarrow$ (~350°C)Ni_3Fe $\longrightarrow$ (~400°C)NiFe $\longrightarrow$ (~550°C)γ_{par} is formed as the annealing temperature increases. The crystal structure in the invar region consists of epitaxially intergrown single-crystal blocks consisting of the paramagnetic γ_{par} and ferromagnetic NiFe phases, which satisfy the orientation relationship [100](001)NiFe || [100](001)γ_{par}. It has been shown that the nucleation temperatures of the Ni_3Fe, NiFe, and γ_{par} phases coincide with the temperatures of solid-state transformations in the Ni–Fe system. © *2004 MAIK "Nauka/Interperiodica".*

PACS numbers: 68.35.Rh; 68.55.Ac; 75.50.Bb

Iron–nickel alloys have been intensively studied for more than a century. The most striking feature of the Fe–Ni system with a high Fe concentration (C_{Fe} ~ 65 at. %) is a very low or even negative coefficient of thermal expansion. However, other physical characteristics, such as the Grüneisen parameter, elastic moduli, specific heats, magnetization, and resistivity also behave anomalously as functions of temperature, pressure, and magnetic field. These anomalous physical and magnetic properties are known as the invar problem [1]. The invar behavior has been observed for a number of iron alloys. The invar properties disappear above the Curie temperature, which indicates that the invar problem is associated with the existence of magnetic order in alloys. Most researches believe that the invar anomalies should be attributed to the existence of two electron spin states of iron in the γ phase. The first state is a low-spin γ_{LS} state with a small lattice constant (a ~ 0.355 nm). The second state is a ferromagnetic (high-spin γ_{HS}) state with a large lattice constant (a ~ 0.364 nm) [1]. According to theoretical calculations, γ iron and invar alloys with various lattice constants include many spin structures with very close energies (see [2, 3] and references cited therein) that are transformed to each other under varying temperatures and which can be responsible for the invar effect in the Fe–Ni system [3]. However, theoretical models are inconsistent with experimental data, where lattices with a > 0.36 nm for equilibrium γ phases of iron–nickel alloys have not yet been observed. Iron–nickel samples exhibiting the invar anomalies are metastable. Their transition to the equilibrium state is accompanied by the phase decomposition of the initial single γ-FeNi phase into a mixture of either γ and α phases in the process of low-temperature annealing or two γ phases for irradiated samples [1, 4–7]. The ordered (or partially ordered) ferromagnetic FeNi phase of the equiatomic composition is one of the γ phases, and the paramagnetic γ_{par} phase is the second γ phase [1, 4–7]. The paramagnetic γ_{par} phase is thought to be either the iron-rich FeNi phase or the Fe_3Ni phase [7, 8]. Mössbauer spectroscopy of iron–nickel alloys irradiated by fast electrons and invar meteorites (taenite) shows that two epitaxially intergrown γ phases with identical or close lattice constants exist at room temperature. These alloys do not undergo the γ $\longrightarrow$ α martensitic transformation and have no invar properties [1, 4, 5, 7].

The existence of the paramagnetic phase in iron–nickel alloys is well established. However, information is scarce about possible mechanisms of its formation, and data on the epitaxial relations with the FeNi phase are absent.

In this work, the formation of phases at the Fe/Ni interface under increasing annealing temperature and the conditions of formation of the paramagnetic γ_{par} phase in epitaxial Ni/Fe/MgO(001) thin films by solid-state synthesis are investigated.

Initial Ni/Fe/MgO(001) samples were obtained by the sequential vacuum deposition of iron and nickel layers on a freshly chipped MgO(001) surface. The thicknesses of iron and nickel films lay in the ranges 150–160 and 50–60 nm, respectively. This layer ratio ensured the formation of invar iron–nickel alloys after solid-state synthesis. To obtain epitaxial layers of iron and nickel, a substrate temperature of 250°C was kept during deposition. Figure 1a shows the diffraction pattern (CuK_α radiation) of the initial Ni/Fe/MgO(001)

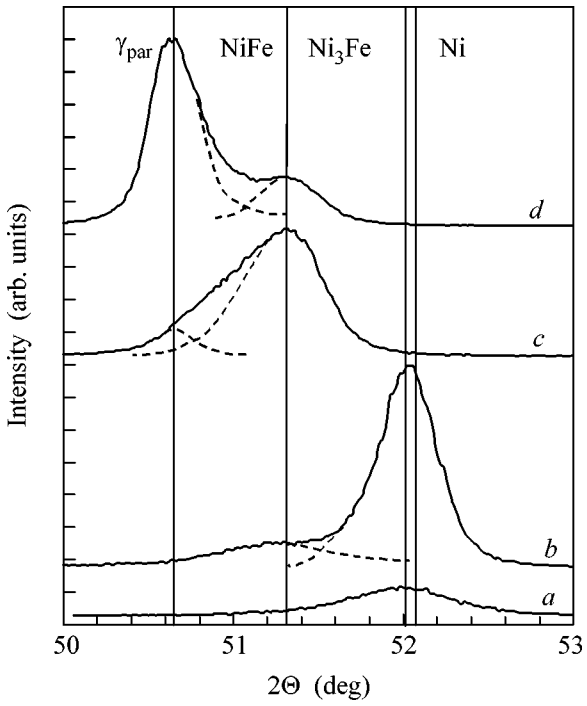

Fig. 1. Evolution of the (002) x-ray reflection of the γ phase in the Ni/Fe/MgO(001) sample during solid-state synthesis for various annealing temperatures: (*a*) initial sample, (*b*) 450, (*c*) 550, and (*d*) 800°C.

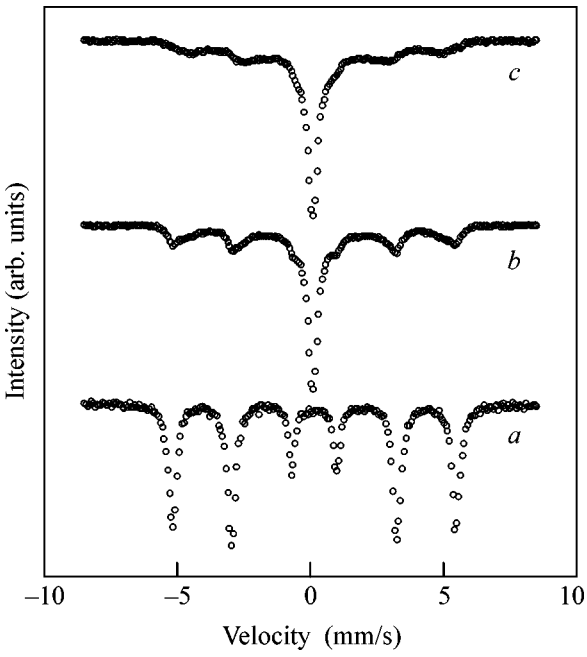

Fig. 2. ^{57}Fe Mössbauer spectra of the Ni/Fe/MgO(001) film sample after annealing at various temperatures: (*a*) initial sample, (*b*) 550, and (*c*) 800°C.

sample. This pattern includes only the Fe(002) and Ni(002) reflections and shows the epitaxial growth of the Fe(001) and Ni(001) layers on the MgO(001) surface under these deposition conditions. It is known that α-Fe and Ni epitaxial films grow on the MgO(001) surface with the maintenance of the orientation relationships [110](001)α-Fe ‖ [100](001)MgO [9, 10] and [100](001)Ni ‖ [100](001)MgO [10], respectively. Therefore, it should be expected that the initial Ni(001)/Fe(001)/MgO(001) samples have the same orientation relationships: [100](001)Ni ‖ [110](001)α-Fe ‖ [100](001)MgO. The Mössbauer spectra of the initial Ni(001)/Fe(001)/MgO(001) samples (Fig. 2a) involve lines in the ratio 3 : 4 : 1 and corroborate formation of α-Fe films on the MgO(001) substrate with the easy magnetization axis in the film plane.

The initial Ni(001)/Fe(001)/MgO(001) samples were subjected to temperature annealing through 50°C in the temperature range (300–700)°C during 30 min. Diffraction data show that the nickel film reacts completely at an annealing temperature of about 350°C, and that a new phase with a lattice constant a = 0.3536 nm is formed. Among stable intermetallic compounds, only the Ni_3Fe phase has a close lattice constant a = 0.3545 (JCPDS card 38-0419). However, epitaxial permalloy films with certain thicknesses may have a much smaller lattice constant a = 0.3529 nm [11]. This implies that Ni_3Fe is first formed at the interface of the Ni(001) and Fe(001) layers. The (002) reflection is single and strong and implies the epitaxial growth of the Ni_3Fe phase. The lattice constant close to the Ni lattice constant indicates that solid-state synthesis gives rise to the replacement of the Ni layer by the Ni_3Fe layer on the Fe(001) surface with the conservation of the orientation relationships [100](001)Ni_3Fe ‖ [110](001)α-Fe ‖ [100](001)MgO. An increase in the annealing temperature to ~400°C leads to formation of the NiFe phase with a lattice constant a = 0.3568 nm, which is slightly less than that in meteorite lamels [12]. The NiFe phase also grows epitaxially (Fig. 1b) between the Ni_3Fe(001) and Fe(001) layers. This growth of the NiFe phase on the Fe(001) surface corresponds to the orientation relationships [100](001)Ni_3Fe ‖ [100](001)NiFe ‖ [110](001)α-Fe ‖ [100](001)MgO. The Ni_3Fe phase disappears at an annealing temperature of about 500°C.

Formation of the Ni_3Fe and NiFe phases in the temperature range up to 550°C due to solid-state synthesis does not change the magnetization of the sample (Fig. 3), which is indicated by the additive contribution of the magnetic moments of iron and nickel atoms to the magnetization of the sample after the reaction. This magnetization lies on the Slater–Pauling curve. However, the magnetization of the sample drops sharply for a temperature of about 550°C (Fig. 3), which is associated with formation of a nonferromagnetic phase. The Mössbauer spectra also change and show that this phase is paramagnetic at room temperature (Fig. 2b). Diffraction reflections corroborate the formation of a

new phase with a lattice constant $a = 0.3600$ nm (Fig. 1c), which corresponds to an atomically disordered γ_{par} phase (taenite phase, JCPDS card 47-1417). The paramagnetic γ_{par} phase is a product of the solid-state synthesis of the residual iron layer in the NiFe phase. The γ_{par} phase, as well as the Ni_3Fe and NiFe phases, grows epitaxially (Fig. 1c) at the Fe(001)–NiFe(001) interface, satisfying the orientation relationships [100](001)NiFe ‖ [100](001)γ_{par} ‖ [100](001)MgO. Further annealing to a temperature of 800°C does not lead to formation of new phases, but the residual iron layer reacts completely, which increases the γ_{par} layer (Figs. 1d, 2c), and the NiFe(002) and γ_{par}(002) are clearly separated from each other (Fig. 1d).

An increase in the annealing time at a temperature of 700°C does not change the ratio of the intensities of the NiFe(002) and γ_{par}(002) diffraction peaks. Quenching from room temperature to liquid-nitrogen temperature is not accompanied by the martensitic transformation. The absence of rearrangements implies that [100](001)NiFe ‖ [100](001)γ_{par} epitaxially intergrown single-crystal blocks, which consist of the paramagnetic γ_{par} and ferromagnetic NiFe phases, are structurally stable in thin films over a wide temperature range. These samples are characterized by magnetocrystalline anisotropy with the constant $K_1 = -2.2 \times 10^4$ erg/cm^3 in the plane, which corroborates the epitaxial growth of the Ni_3Fe, NiFe, and γ_{par} phases in the process of solid-state synthesis. All Mössbauer spectra of these samples contain a sextet from the NiFe ferromagnetic phase and a paramagnetic singlet from the γ_{par} phase. Thus, the mechanism of the solid-state synthesis of intermetallides at the interface of the Fe(001) and Ni(001) single-crystal films may be as follows. Above 350°C, iron atoms begin to diffuse and discretely expand the nickel lattice with the sequential formation of the Ni_3Fe and NiFe phases. The further migration of iron atoms into the NiFe lattice at a temperature of about 550°C leads to the further expansion of the lattice, destruction of the ferromagnetic order in it, and formation of the γ_{par} phase. The above experimental data show that the two coherently intergrown γ phases obtained in this work are identical to the structure of irradiated iron–nickel alloys and invar meteorites [1, 4–8].

Numerous investigations have shown that a phase of reaction products, called the first phase, is formed in bilayer and multilayer films at a certain temperature upon heating. With a further increase in the annealing temperature, new phases, called phase sequences, are sequentially formed [13]. As was shown in [14–17], the initiation temperatures of solid-state reactions coincide with the temperatures of solid-state transformations of the reaction products. Indeed, solid-state synthesis in S/Fe bilayer films is initiated at the temperature of the metal–dielectric phase transition in iron monosulphide (FeS) [14]. The connection of solid-state synthesis with the order–disorder phase transition was investigated for

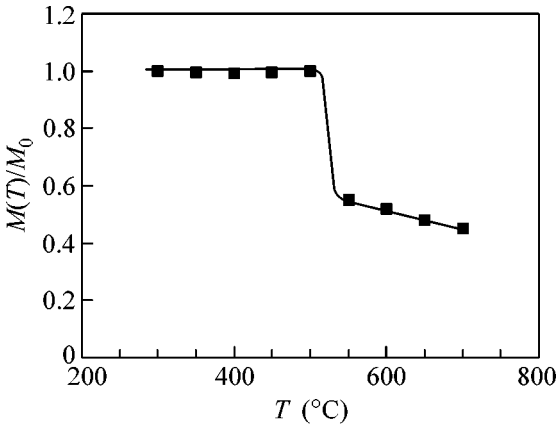

Fig. 3. Relative saturation magnetization of the Ni/Fe/MgO(001) film sample vs. annealing temperature.

the Cu–Au system, which is classical for the ordering phenomenon. Solid-state reactions in Cu/Au bilayer films proceed at the Kurnakov temperature of the CuAu superstructure formed in the reaction products [15]. It was shown in [16] that solid-state synthesis in Se/Cu bilayer films is associated with the superionic transition in copper selenide. Martensitic transformations are diffusionless solid-state transformations, wherein atoms pass from the austenite phase to the martensite phase by collective coherent motion without the rupture of chemical bonds. For this reason, it was surprising that compounds were formed at the temperature A_S of the reverse martensitic transformation [17].

According to the above analysis, solid-state synthesis in Fe/Ni bilayer films leads to formation of the phase sequence Fe/Ni ⟶ (~350°C)Ni_3Fe ⟶ (~400°C)NiFe ⟶ (~550°C) γ_{par}. Therefore, the nucleation temperatures of the Ni_3Fe, NiFe, and γ_{par} phases must coincide with the temperatures of solid-state transformations of these phases. At present, reliable phase-transformation diagrams are absent for the Ni–Fe system. In the last variant of the state diagram for the Ni–Fe system, the temperature $T_0(Ni_3Fe) = 350$°C corresponds to the temperature (345°C) of eutectoid decomposition into a mixture of α-Fe and Ni_3Fe phases [18]. The temperature T_0(NiFe) = 400°C is close to the temperature (389°C) of the monotectic horizontal corresponding to decomposition into the paramagnetic and ferromagnetic phases [18]. The temperature $T_0(\gamma_{par}) = 550$°C must correspond to the temperature A_S of the inverse martensitic transformation. Experimental A_S values are absent for iron–nickel films and vary within the range (300–700)°C for bulk samples. The above comparison of the phase-nucleation temperatures with the temperatures of solid phase transformations in the Fe–Ni system is preliminary and requires further refinement.

Thus, it was shown that the phases Ni_3Fe ($a = 0.3536$ nm), NiFe ($a = 0.3568$ nm), and γ_{par} ($a =$

0.3600 nm) are sequentially formed at the interface of the Ni(001) and Fe(001) epitaxial layers as the annealing temperature increases. These phases are presumedly formed due to the migration of iron atoms into the nickel lattice with the conservation of the orientation relationships. The final products of solid-state synthesis are single-crystal blocks of the ferromagnetic NiFe and paramagnetic γ_{par} phases that are coherently intergrown and that have different lattice constants. An important conclusion is that the crystal structures of two γ phases intergrown due to solid-state synthesis in thin films, irradiated bulkiron–nickel alloys, and invar meteorites are identical.

This work was supported by the OAO MMK Foundation, the Research & Technological Centre Ausferr, and the Intels Foundation for Science and Education (project no. 10-03-02).

REFERENCES

1. V. L. Sedov, *Antiferromagnetism of Gamma Iron. The Invar Problem* (Nauka, Moscow, 1987) [in Russian].
2. V. P. Antropov, M. I. Katsnelson, M. van Schilfgaarde, and B. N. Harmon, Phys. Rev. Lett. **75**, 729 (1995); V. P. Antropov, M. I. Katsnelson, B. N. Harmon, *et al.*, Phys. Rev. B **54**, 1019 (1996); L. T. Kong and B. X. Liu, Appl. Phys. Lett. **84**, 3627 (2004).
3. M. van Schilfgaarde, I. A. Abricosov, and B. Johansson, Nature **400**, 46 (1999); Y. Wang, G. M. Stoks, D. M. C. Nicholson, and W. A. Shlton, J. Appl. Phys. **81**, 3873 (1997).
4. A. Chamberod, J. Laugier, and J. M. Penisson, J. Magn. Magn. Mater. **10**, 139 (1979).
5. J. Danon, R. B. Scorzelli, I. Souza-Azevedo, *et al.*, Nature **284**, 537 (1980).
6. S. S. Aliev, P. L. Gruzin, and A. Z. Men'shikov, Metallofizika (Kiev) **7**, 80 (1984).
7. D. G. Rancourt and R. B. Scorzelli, J. Magn. Magn. Mater. **150**, 30 (1995).
8. D. G. Rancourt, K. Lagarec, A. Densmore, *et al.*, J. Magn. Magn. Mater. **191**, 255 (1999).
9. G. Fahsold, A. Priebe, and A. Pucci, Appl. Phys. A **73**, 39 (2001).
10. S. Chikazumi, J. Appl. Phys. **32**, 81S (1961).
11. F. Michelini, J. Degauque, P. Baules, *et al.*, J. Magn. Magn. Mater. **242–245**, 173 (2002).
12. J. F. Albertsen, G. B. Jensen, and J. M. Knudsen, Nature **273**, 453 (1978).
13. *Thin Films: Interdiffusion and Reactions*, Ed. by J. M. Poate, K. N. Tu, and J. W. Mayer (Wiley, New York, 1978; Mir, Moscow, 1982); R. M. Walser and R. W. Bene, Appl. Phys. Lett. **28**, 624 (1976); R. W. Bene, Appl. Phys. Lett. **41**, 529 (1982); U. Gösele and K. N. Tu, J. Appl. Phys. **53**, 3252 (1982); J. Appl. Phys. **66**, 2619 (1989); F. M. d'Heurle and P. Gas, J. Mater. Res. **1**, 205 (1986); M. H. da Silva Bassani *et al.*, Scr. Mater. **37**, 227 (1997); J. J. Hoyt and L. N. Brush, J. Appl. Phys. **78**, 1589 (1995); W. H. Wang and W. K. Wang, J. Appl. Phys. **76**, 1578 (1994); M. Zhang, J. Appl. Phys. **80**, 1422 (1996); L. A. Clevenger, B. Arcot, W. Ziegler, *et al.*, J. Appl. Phys. **83**, 90 (1998); T. Nakanishi, M. Takeyama, A. Noya, and K. Sasaki, J. Appl. Phys. **77**, 948 (1995).
14. V. G. Myagkov, L. E. Bykova, G. N. Bondarenko, *et al.*, Dokl. Akad. Nauk **371**, 763 (2000) [Dokl. Phys. **45**, 157 (2000)].
15. V. G. Myagkov, L. E. Bykova, G. N. Bondarenko, *et al.*, Pis'ma Zh. Éksp. Teor. Fiz. **71**, 268 (2000) [JETP Lett. **71**, 183 (2000)].
16. V. G. Myagkov, L. E. Bykova, G. N. Bondarenko, *et al.*, Dokl. Akad. Nauk **390**, 35 (2003) [Dokl. Phys. **48**, 206 (2003)].
17. V. G. Myagkov, L. E. Bykova, L. A. Li, *et al.*, Dokl. Akad. Nauk **382**, 463 (2002) [Dokl. Phys. **47**, 95 (2002)]; V. G. Myagkov, L. E. Bykova, and G. N. Bondarenko, Dokl. Akad. Nauk **388**, 844 (2003) [Dokl. Phys. **48**, 30 (2003)]; V. G. Myagkov and L. E. Bykova, Dokl. Akad. Nauk **396**, 187 (2004) [Dokl. Phys. **49**, 289 (2004)].
18. *Phase Diagrams of Binary Metal Systems*, Ed. by N. P. Lyakishev (Mashinostroenie, Moscow, 1982), Vol. 2 [in Russian].

Translated by R. Tyapaev

JETP Letters, Vol. 80, No. 7, 2004, pp. 491–493. Translated from Pis'ma v Zhurnal Éksperimental'noĭ i Teoreticheskoĭ Fiziki, Vol. 80, No. 7, 2004, pp. 560–562.

Effect of the Ferromagnetic Layer Thickness on the Interlayer Interaction in Fe/Si/Fe Trilayers

G. S. Patrin[1, 2,*], N. V. Volkov[1], S. G. Ovchinnikov[1], E. V. Eremin[1], M. A. Panova[2], and S. N. Varnakov[1]

[1] *Kirensky Institute of Physics, Siberian Division, Russian Academy of Sciences, Krasnoyarsk, 660036 Russia*
[2] *Krasnoyarsk State University, Krasnoyarsk, 660041 Russia*
**e-mail: patrin@iph.krasn.ru*
Received August 19, 2004

Three-layer magnetic film systems Fe/Si/Fe have been studied by the method of magnetic resonance. It is established that the ferromagnetic layer thickness affects the magnitude of the interlayer exchange interaction in this system. A mechanism explaining the observed effect is proposed. © *2004 MAIK "Nauka/Interperiodica".*

PACS numbers: 75.70.Fr; 76.50.+g

Films based on the Fe/Si layer system are of interest because they feature interesting phenomena related to the presence of a semiconductor interlayer (spacer). Depending on the conditions of synthesis, either a ferromagnetic (FM) [1] or an antiferromagnetic (AFM) [2, 3] exchange between the magnetic layers takes place. It was also established that the exchange interaction between Fe layers increases with temperature and that it may exhibit an oscillatory character depending on the Si layer thickness (t_{Si}) [4]. In addition, such films exhibit the phenomenon of photoinduced changes in the magnitude of the interlayer interaction [5, 6].

Despite extensive research, problems related to the formation of the magnetic state of a multilayer system are still unsolved. In this context, the most important task is to study the mechanisms of spin-dependent electron transfer via nonmagnetic spacers, since peculiarities of this transport determine the character of the interlayer exchange interaction. It is obvious that the efficiency of the spin-dependent electron transfer must depend both on the spacer material and on the magnetic state of the layers. For multilayer systems with nonmagnetic metallic spacers, some theoretical results [7] indicate that the magnitude of the exchange interaction between magnetic layers might depend on their thickness. This dependence was experimentally confirmed and shown to exhibit an oscillatory character [8]. In the case of a nonmetallic spacer representing a potential barrier, the existing theories [9, 10] also predicted the dependence of the interlayer interaction on the magnetic-layer thickness.

This paper presents the results of our experimental investigation of the influence of the ferromagnetic-layer thickness on the interlayer exchange interaction in a three-layer system (Fe/Si/Fe trilayer) with a semiconductor spacer.

We have studied two sets of samples, comprising (i) FM metal layers without a spacer and (ii) trilayers with a silicon spacer of thickness t_{Si} = 2 nm (corresponding to the maximum AMF interlayer exchange interaction, according to published data [1] and our previous results [6]). The thickness of the FM layer t_{Fe} in each set was varied from 2 to 10 nm at a 1-nm step. The films were obtained by the method of thermal deposition in vacuum onto glass substrates in an Angara setup with a residual pressure of $P = 10^{-7}$ Pa. The glass substrates were initially covered by a 10-nm-thick buffer layer of silicon. Then, a magnetic Fe/Si/Fe trilayer structure was deposited and covered with a protective 10-nm-thick silicon layer. For each thickness of the iron film, a control sample without a silicon spacer was prepared in the same vacuum technology cycle.

The results of electron-microscopic examination showed that the films possessed an almost completely amorphous structure. The samples were studied by method of electron magnetic resonance, which is sensitive to changes in the internal molecular fields. The microwave frequency was ω_{UHF} = 28.75 GHz and the constant magnetic field was oriented in the plane of the sample. The measurements were performed in the temperature range T = 78–300 K.

The results of the magnetic resonance measurements in Fe/Si/Fe trilayers showed that the microwave absorption lines in all samples (except for the control ones, deprived of the silicon spacer) have an asymmetric shape and exhibit no anisotropy in the film plane. The magnetic resonance line width was on the order of $\Delta H \approx 200$ Oe.

First, we measured the dependence of the resonance field on the FM-layer thickness t_{Fe} (Fig. 1). These data were used to determine the magnetization of iron layers

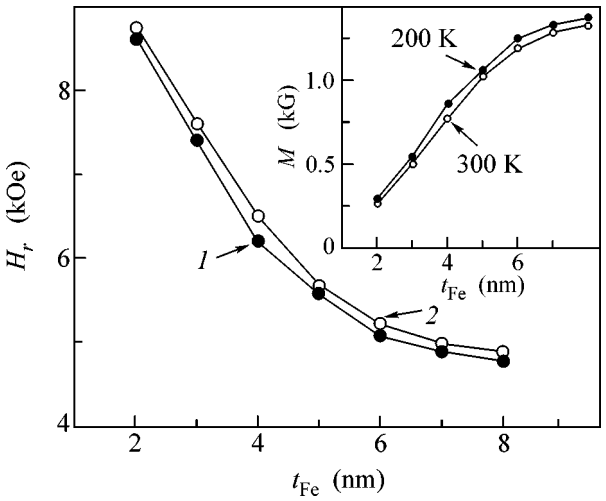

Fig. 1 Plots of the resonance field H vs. magnetic-layer thickness t_{Fe} for the control samples measured at T = 200 (*1*) and 300 K (*2*). The inset shows the plot of magnetization M vs. t_{Fe}.

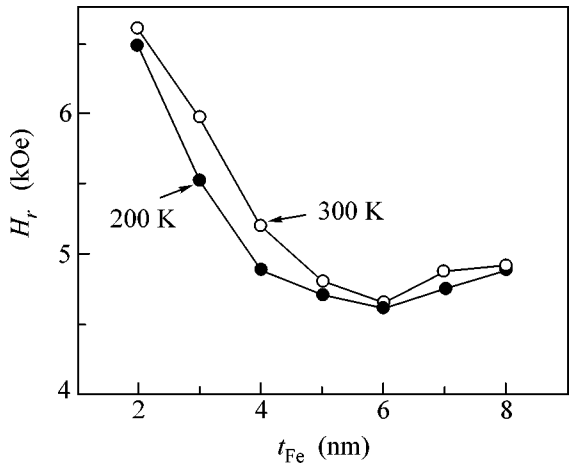

Fig. 2. Plots of the resonance field H vs. magnetic-layer thickness t_{Fe} for the Fe/Si/Fe trilayers with t_{Si} = 2 nm measured at T = 200 (*1*) and 300 K (*2*).

(inset in Fig. 1) according to the Kittel formula (see relation (2) below) [11].

Then, the measurements were performed for the samples with spacers. Figure 2 shows a plot of the resonance field versus t_{Fe} for the samples with t_{Si} = 2 nm measured at T = 200 and 300 K (where the interlayer exchange interaction constant was expected to depend strongly on the sample temperature).

The experimental data were processed using the results of calculations of the magnetic resonance spectrum for a three-layer magnetic film [12]. In application to the case under consideration, the free energy per unit area of the film is

$$E = -J\cos(\varphi_1 - \varphi_2) - t_{Fe}[\mathbf{H}(\mathbf{M}_1 + \mathbf{M}_2) + 4\pi(M_{1Z}^2 + M_{2Z}^2)], \quad (1)$$

where J is the interlayer exchange interaction constant, $\mathbf{H}$ is the applied magnetic field, $\mathbf{M}_i$ is the magnetization of the ith FM layer, φ_i is the magnetization angle in the plane (measured relative to the direction of the applied magnetic field), i = 1, 2 is the FM layer number, t_{Fe} is the magnetic layer thickness, and the Z axis is perpendicular to the film plane. In the calculations, we assumed that $(t_{Fe} \cdot \mathbf{H} \cdot \mathbf{M}) \gg J$ and that the FM films occur in the saturated state, so that $\varphi_i \cong \varphi_H = 0$. It was also assumed that the two FM layers are perfectly identical.

Under the above conditions, the resonance frequencies are described by the relations

$$(\omega_1/\gamma)^2 = H(H + H_M), \quad (2)$$

$$(\omega_2/\gamma)^2 = H(H + H_M) + 2(2H + H_M)H_J + 4H_J^2, \quad (3)$$

where

$$H + M = 4\pi M \text{ and } H_J = J/(t_{Fe}M). \quad (4)$$

Once the values of ω, H, and M are known, one can readily calculate H_J using Eq. (3) and then determine the interlayer exchange interaction constant J from relation (4). From such calculations, we obtained two sets of H_J values. In the first set, H_{J1} values fall within the interval from –6 to –14 kOe. These values do not satisfy the approximation adopted and do not correspond to the experimental data. For these reasons, the solution H_{J1} was rejected. The other set (H_{J2}) gives the $J(t_{Fe})$ plotted in Fig. 3. As can be seen, this dependence is nonmonotonic, and the J values in the region of the maximum agree with the published data [4]. To within the experimental error in the temperature range studied, the results exhibited virtually no temperature dependence. It should be emphasized that such dependences of the interlayer exchange interaction constant on the magnetic-layer thickness are not described by any of the existing theories.

The observed variation of the average magnetization of the magnetic layer depending on its thickness is rather typical. This behavior is explained by the fact that, for small t_{Fe} values, the interfacial (transition) regions account for a considerable proportion of the metal layer, while the role of the internal ("bulk") regions is relatively small. As the metal layer thickness is increased, the bulk fraction increases, while the width of the interfacial regions remains the same. In the presence of the silicon spacer, electrons of an FM layer, which are involved in the interaction and which bear "information" about the magnetic state of this layer, penetrate (without losing this information) into the

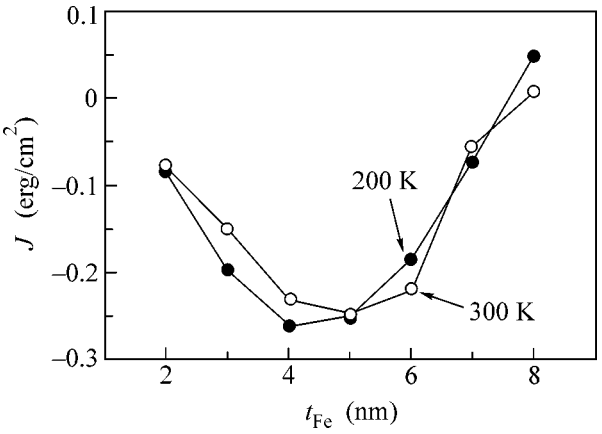

Fig. 3. Plots of the interlayer interaction energy J vs. magnetic-layer thickness t_{Fe} for the Fe/Si/Fe trilayers with t_{Si} = 2 nm measured at T = 200 (*1*) and 300 K (*2*).

other layer to a certain depth, thus determining the effective volumes of the interacting regions of both FM layers.

If the outlined scenario is valid, a value of ~5 nm is the depth to which the electrons mediating the exchange interaction penetrate into the FM layer with increasing thickness t_{Fe}. For small t_{Fe}, an increase in the magnetic-layer thickness leads to, besides an increase in the magnetization, a growth of the volume of the magnetic material involved in the interaction between FM layers and, hence, of the magnitude of the interlayer interaction. As the FM layer thickness is increased further (>5 nm), the interactions inside each such layer become prevailing and the role of the interlayer exchange becomes relatively smaller. These considerations qualitatively explain the dependences presented in Fig. 3. It should be noted that the obtained results are not related to the formation of compounds (iron silicides) in the transition regions. The results of a special investigation performed by Decoster *et al.* [13] showed that traces of ε-FeSi are detectable only in the case when the iron film is composed of coarse crystallites.

In conclusion, it should be noted that, besides a basic significance related to the investigation of the laws of formation of the magnetic structures in multilayer magnetic films, the obtained relations should be taken into consideration when studying the giant magnetoresistance in such films. Our results show that, to obtain the maximum GMR effect, it is necessary to select the optimum thicknesses not only of the nonmagnetic spacers, but of the magnetic layers as well.

This study was supported by the Russian Foundation for Basic Research, project no. 02-02-17224a.

REFERENCES

1. S. Toscano, B. Briner, H. Hopster, and M. Landolt, J. Magn. Magn. Mater. **114**, L6 (1992).
2. E. E. Fullerton, J. E. Mattson, S. R. Lee, *et al.*, J. Magn. Magn. Mater. **117**, L301 (1992).
3. G. S. Patrin, S. G. Ovchinnikov, D. A. Velikanov, and V. P. Kononov, Fiz. Tverd. Tela (St. Petersburg) **43**, 1643 (2001) [Phys. Solid State **43**, 1712 (2001)].
4. B. Briner, U. Ramsperger, and M. Landolt, Phys. Rev. B **51**, 7303 (1995).
5. J. E. Mattson, S. Kumar, E. E. Fullerton, and S. R. Lee, Phys. Rev. Lett. **78**, 3023 (1997).
6. G. S. Patrin, N. V. Volkov, and V. P. Kononov, Pis'ma Zh. Éksp. Teor. Fiz. **68**, 287 (1998) [JETP Lett. **68**, 307 (1998)].
7. P. Bruno, Europhys. Lett. **23**, 615 (1993).
8. P. J. H. Bloemen, M. T. Johnson, M. T. H. Vorst, *et al.*, Phys. Rev. Lett. **72**, 764 (1994).
9. J. Z. Wang and B. Z. Li, Phys. Rev. B **59**, 6383 (1999).
10. J. Z. Wang, B. Z. Li, and Z. N. Hu, Phys. Rev. B **62**, 6570 (2000).
11. A. G. Gurevich, *Magnetic Resonance in Ferrites and Antiferromagnets* (Nauka, Moscow, 1974) [in Russian].
12. A. Layadi, Phys. Rev. B **65**, 104 422 (2002).
13. J. Dekoster, H. Bemelmans, S. Degroote, *et al.*, J. Appl. Phys. **81**, 5349 (1997).

Translated by P. Pozdeev

JETP Letters, Vol. 80, No. 7, 2004, pp. 494–499. From Pis'ma v Zhurnal Éksperimental'noĭ i Teoreticheskoĭ Fiziki, Vol. 80, No. 7, 2004, pp. 563–568.

Effects of Spin–Orbit Interaction on Superconductor–Ferromagnet Heterostructures: Spontaneous Electric and Spin Surface Currents¶

I. V. Bobkova and Yu. S. Barash*

Institute of Solid State Physics, Russian Academy of Sciences, Chernogolovka, Moscow region, 142432 Russia
** e-mail: barash@issp.ac.ru*

Received August 24, 2004; in final form, September 8, 2004

We find proximity-induced spontaneous spin and electric surface currents at all temperatures below the superconducting T_c in an isotropic *s*-wave superconductor deposited with a thin ferromagnetic metal layer with spin–orbit interaction. The currents are carried by Andreev surface states and generated as a joint effect of the spin–orbit interaction and the exchange field. The background spin current arises in the thin layer due to different local spin polarizations of electrons and holes, which have almost opposite velocities in each of the surface states. The spontaneous surface electric current in the superconductor originates in the asymmetry of Andreev states with respect to sign reversal of the momentum component parallel to the surface. The conditions for electric and spin currents to show up in the system significantly differ from each other. © *2004 MAIK "Nauka/Interperiodica".*

PACS numbers: 74.45.+c; 74.81.–g

Proximity effects in superconductor–ferromagnet heterostructures have attracted much attention in recent years. In contrast to the nonmagnetic case, magnetic surfaces and interfaces make spin-flip processes possible, suppress an *s*-wave superconducting order parameter, and generates Andreev bound states in adjacent superconducting regions [1–5]. The spin structure of Andreev bound states near complex magnetic interfaces can be rather involved [5]. Triplet components of the order parameter in a singlet superconductor can be induced by ferromagnets under certain conditions [6]. Cooper pair wave functions exponentially decay into the bulk of ferromagnets, oscillating at the same time [7], and acquire a triplet component in the ferromagnetic region [8]. These proximity effects can lead, in particular, to specific properties of the Josephson current through magnetic interfaces, which have been intensively studied both theoretically and experimentally [1–7, 9–14]. Also, proximity-induced nonmonotonic dependence of the superconducting critical temperature on the thickness of the ferromagnetic layer has been thoroughly studied for superconductor–ferromagnetic metal bilayers or heterostructures (see, for example, [10, 11, 15–18] and references therein).

Spontaneous surface currents represent other important example of possible proximity-induced effects. Spontaneous electric currents taking place near surfaces or interfaces on the scale of the superconducting coherence length produce a magnetic field and, hence, a counterflow of screening supercurrents on the scale of the penetration depth. The electric current can arise, for example, near nonmagnetic surfaces and interfaces of unconventional superconductors, whose states break time-reversal symmetry [19, 20]. In particular, the electric current carried by Andreev states appears near nonmagnetic surfaces and interfaces of chiral superconductors [21]. The current also occurs if a surface-induced subdominating pairing shows up near surfaces of *d*-wave superconductors, thus breaking the time-reversal symmetry of the superconducting state [22]. Another possible mechanism of generating electric surface currents is specifically based on a paramagnetic response of the zero-energy Andreev surface states to an applied magnetic field. This can take place at low temperatures at smooth (110) surfaces of *d*-wave superconductors [23, 24], as well as in a system with a thin ferromagnetic metallic layer deposited on a semi-infinite bulk isotropic *s*-wave superconductor [25]. In the latter case, the energy of the surface states becomes zero only for several values of the layer thickness and, in the presence of particle–hole asymmetry, the spontaneous electric current is accompanied by a spontaneous surface spin current [25]. Dissipationless background spin currents, which occur in various systems in the equilibrium and do not lead to any spin accumulation, have been a subject of recent discussions and studies [26–28]. These spin currents can be generated, for example, by the spin–orbit interaction (in particular, via the Rashba term) in two-dimensional metals. Measurements of background persistent spin currents have not been carried out yet, although some suggestions for a

¶ This article was submitted by the authors in English.

direct detection of these currents have been proposed in the literature [26, 29].

In the present paper, we study spontaneous currents under conditions when the spin–orbit interaction takes place in a thin ferromagnetic metal layer in proximity to an isotropic *s*-wave superconductor. The joint effect of the spin–orbit interaction, described by the Rashba term, and the exchange field is shown to play an important role in generating spontaneous currents. We find that the superconductor induces background spin currents in the ferromagnetic layer with the spin–orbit interaction (FSOL) for all temperatures below the superconducting T_c. This spin current is carried by Andreev surface states and takes finite values due to different local spin polarizations of electrons and holes, which have almost opposite velocities in each of these states. The maximal possible values of the background spin current density are on the order of the Landau depairing current density. We find proximity-induced finite spin currents within the quasiclassical approach, when only linear terms in the small parameters $\alpha p_f/\varepsilon_f$ and h/ε_f are taken into account in describing the FSOL. Spontaneous background spin currents, which arise in two-dimensional electron systems with spin–orbit interaction without any proximity effects [27], contain higher powers of these parameters, which are assumed below to be small. Furthermore, a spontaneous electric surface current that is carried by Andreev surface states arises in the superconductor due to proximity to the FSOL. The respective structures of wave functions and the spectra of the surface states are strongly influenced by the spin–orbit interaction and the exchange field and differ for quasiparticles with opposite momentum components $\mathbf{p}_{f\|}$ parallel to the surface. The spontaneous electric current arises as a result of this asymmetry of Andreev states with respect to $\mathbf{p}_{f\|} \longrightarrow -\mathbf{p}_{f\|}$, to some extent analogously to the current induced by chiral surface or interface states. The conditions for electric and spin currents to show up in the system we study significantly differ from each other. Thus, the spontaneous spin current in the FSOL arises even within the framework in which the surface electric current vanishes.

We consider an isotropic *s*-wave superconductor at $x > d$, deposited with a layer of thickness d made of a ferromagnetic metal. We let a macroscopic thickness of the layer be much less than the superconducting coherence length: $d \ll \xi_s$. Both the internal exchange field $\mathbf{h}$ and the spin–orbit Rashba term $\mathbf{w}\boldsymbol{\sigma} = \alpha(\mathbf{n} \times \mathbf{p}_{\|})\boldsymbol{\sigma}$ enter into the Hamiltonian density of the FSOL: $\hat{\mathcal{H}}(x) = \hat{H}^{(0)} - (\mathbf{h}(x) + \mathbf{w}(x))\boldsymbol{\sigma}$. Here, $\hat{H}^{(0)}$ describes the kinetic energy of free electrons, $\mathbf{n}$ is the unit vector along the surface normal, and $\mathbf{p}_{\|}$ is the momentum component parallel to the surface. The exchange field is assumed to be always aligned along the z axis. Both $\mathbf{h}(x)$ and $\mathbf{w}(x)$ are taken to be finite and spatially constant within the FSOL $0 < x < d$. The x axis is taken directed into the depth of the superconductor and the system is confined by an impenetrable wall at $x = 0$.

We assume $\Delta \ll h \ll \varepsilon_f$ and $\Delta \ll \alpha p_f \ll \varepsilon_f$ and describe the system in question by quasiclassical Eilenberger equations for the Green's function:

$$-iv_{f,x}\frac{\partial \check{g}}{\partial x} = [(i\varepsilon_n\hat{\tau}_z + \hat{\tau}_z\check{\Delta} + \mathbf{h}\check{\mathbf{s}} + \mathbf{w}\hat{\tau}_z\check{\mathbf{s}}), \check{g}], \quad (1)$$

$$\check{g}^2 = -\pi^2. \quad (2)$$

Here, $\check{g}(x, \mathbf{p}_f, \varepsilon_n)$ takes a 4×4 matrix form in the four-dimensional product space of particle–hole and spin variables. In the particle–hole space,

$$\check{g}(\mathbf{p}, \varepsilon_n, x) = \begin{pmatrix} \hat{g}(\mathbf{p}, \varepsilon_n, x) & \hat{f}(\mathbf{p}, \varepsilon_n, x) \\ \hat{\bar{f}}(\mathbf{p}, \varepsilon_n, x) & \hat{\bar{g}}(\mathbf{p}, \varepsilon_n, x) \end{pmatrix}. \quad (3)$$

where all matrix elements are 2×2 matrices in spin space. The Pauli matrices in particle–hole space are $\hat{\tau}_j$, $\hat{\tau}_{\pm} = \hat{\tau}_x \pm i\hat{\tau}_y$, while, in spin space, they are $\hat{\sigma}_i$. The superconducting order-parameter matrix is $\check{\Delta} = 1/2[\hat{\tau}_+\Delta - \hat{\tau}_-\Delta^*]i\hat{\sigma}_y$. The operator for quasiparticle spin is $(1/2)\check{\mathbf{s}}\hat{\tau}_z$, whereas the operator $\check{\mathbf{s}} = 1/2[(1 + \hat{\tau}_z)\hat{\boldsymbol{\sigma}} - (1 - \hat{\tau}_z)\hat{\sigma}_y\hat{\boldsymbol{\sigma}}\hat{\sigma}_y]$ enters into the Zeeman term. The order parameter Δ is taken to be spatially constant throughout the superconducting half-space $x > d$. As this follows from recent results for two-dimensional superconductors with spin–orbit coupling [30], a possibility for a proximity-induced inhomogeneous phase of the order parameter in the plane parallel to the interface should be studied for a sufficiently thin superconducting layer in proximity to the FSOL. This two-dimensional inhomogeneous profile of the phase does not appear, however, for a massive superconducting sample.

The electric and spin current densities can be expressed via the quasiclassical Green's function as follows:

$$\mathbf{j} = N_f T\left\langle \mathbf{v}_f \sum_{\varepsilon_n} \mathrm{Sp}_2\hat{g}(\mathbf{p}_f, \varepsilon_n)\right\rangle_{S_f}, \quad (4)$$

$$\mathbf{j}_i^s = \frac{N_f T}{2}\left\langle \mathbf{v}_f \sum_{\varepsilon_n} \mathrm{Sp}_2\hat{\sigma}_i\hat{g}(\mathbf{p}_f, \varepsilon_n)\right\rangle_{S_f}. \quad (5)$$

Here, N_f is the normal state density of states per spin direction, while $\langle \ldots \rangle_{S_f}$ implies averaging over quasiparticle states at the Fermi surface. The spin current j_{il}^s carries the ith spin component along l axis in coordinate space. One can introduce the following scalar g_0 and vector $\mathbf{g}$ components of Green's function in spin space:

$\hat{g}(\mathbf{p}_f, \varepsilon_n) = g_0(\mathbf{p}_f, \varepsilon_n)\hat{\sigma}_0 + \mathbf{g}(\mathbf{p}_f, \varepsilon_n)\hat{\boldsymbol{\sigma}}$. As can be seen from Eqs. (4) and (5), g_0 determines the electric current, while the spin current is associated with **g**. We should emphasize that Eq. (5) is an approximate equation that is valid only to quasiclassical accuracy. One can safely calculate with Eq. (5) the terms in the spin current of the order of $N_f v_f \alpha p_f$, $N_f v_f h$, $N_f v_f \Delta$, which can also contain any functions of $(\alpha p_f/h)$ and/or $\alpha p_f/\Delta$. However, terms with additional powers of the small quasiclassical parameters $(\alpha p_f/\varepsilon_f)$, (Δ/ε_f), and (h/ε_f) lie beyond the accuracy of Eq. (5). These terms should be described with the Gor'kov equations and the exact symmetrized operator for the spin current $\hat{J}_{ij} = (1/2)[(p_j/m)\hat{\sigma}_i + e_{xij}\alpha]$. The second term in the last expression is of the order $\alpha p_f/\varepsilon_f$ with respect to the first one. For this reason, it contributes to the spin current beyond the quasiclassical accuracy and is not taken into account in Eq. (5).

Green's function for the FSOL satisfies conventional boundary conditions on the impenetrable wall at $x = 0$: $\check{g}(0, \mathbf{p}_f, \varepsilon_n) = \check{g}(0, \tilde{\mathbf{p}}_f, \varepsilon_n)$, where $\mathbf{p}_f$ and $\tilde{\mathbf{p}}_f$ are the incoming and the outgoing quasiparticle momenta, respectively. We match the solutions of Eilenberger equations for the superconducting half-space and for the FSOL with the continuity conditions on a transparent interface at $x = d$. Substituting the final result for Green's function into Eqs. (4) and (5), we find no spontaneous electric current in the system and finite components j^s_{yz}, j^s_{zy} of spin current situated in the FSOL and flowing parallel to the surface.

One can show that the whole spin current is carried by the Andreev surface states that occur in the system. We find two dispersive branches of the Andreev surface states, whose energies depend on the momentum component that is parallel to the surface:

$$\varepsilon_{1,2} = \mp \mathrm{sgn}\left[\sin\left(\frac{\Phi}{2}\right)\right]\Delta\cos\left(\frac{\Phi}{2}\right). \qquad (6)$$

Here,

$$\cos\Phi = \cos^2\frac{\varphi}{2}\cos\frac{\Theta_+ + \Theta_-}{2} + \sin^2\frac{\varphi}{2}\cos\frac{\Theta_+ - \Theta_-}{2}, \quad (7)$$

$$\Theta_\pm = \frac{4|\mathbf{h} \pm \mathbf{w}|d}{|v_{f,x}|}, \quad \cos\varphi = \mathbf{e}_+\mathbf{e}_-, \quad \mathbf{e}_\pm = \frac{(\mathbf{h} \pm \mathbf{w})}{|\mathbf{h} \pm \mathbf{w}|}. \quad (8)$$

In the absence of spin–orbit interaction, the spectra of Andreev states, which are described by Eqs. (6)–(8), reduce to the results for spin-discriminated Andreev states at a ferromagnetic surface [1, 4].

Andreev surface states carry no spin current in a singlet superconductor, since the particles and holes occupying the state have identical spatially constant local spin polarization and opposite velocities. However, the wave function of Andreev surface states does not vanish in the FSOL and has a qualitatively different spin structure there as compared with the superconducting region. One can extract polelike terms from the whole expression for the electron retarded Green's function $\hat{g}^R(x, \mathbf{p}_f, \varepsilon)$ near the bound state energies $\varepsilon_{1,2}$. We determine the spin structure of electrons in the Andreev states in terms of eigenvectors of these polelike terms in spin space $\begin{pmatrix}\alpha\\ \beta\end{pmatrix}(x, \mathbf{p}_f, \varepsilon)$. The unit vector $\mathbf{P}^e$, which describes the electron spin polarization, can be found from the equation $\mathbf{P}^e\hat{\boldsymbol{\sigma}}\begin{pmatrix}\alpha\\ \beta\end{pmatrix}(x, \mathbf{p}_f, \varepsilon) = \begin{pmatrix}\alpha\\ \beta\end{pmatrix}(x, \mathbf{p}_f, \varepsilon)$. As a result, we obtain the following spatially dependent spin polarization for electrons in Andreev surface states (Eq. (6)) at $0 < x < d$:

$$\mathbf{P}^e(\mathbf{p}_f, \varepsilon_{1,2}) = \mp\frac{1}{\sin\Phi}\Bigg[(\mathbf{e}_+ \times \mathbf{e}_-)\sin\frac{\Theta_+ x}{2d}\sin\frac{\Theta_-}{2}$$

$$-(\mathbf{e}_+ \times (\mathbf{e}_+ \times \mathbf{e}_-))\sin\frac{\Theta_-}{2}\left(\cos\frac{\Theta_+ x}{2d} - \cos\frac{\Theta_+}{2}\right) \qquad (9)$$

$$+\left(\mathbf{e}_-\cos\frac{\Theta_+}{2}\sin\frac{\Theta_-}{2} + \mathbf{e}_+\cos\frac{\Theta_-}{2}\sin\frac{\Theta_+}{2}\right)\Bigg].$$

The local spin polarization of electrons occupying Andreev states is spatially constant inside the superconductor and takes there the same value as follows from Eq. (9) at $x = d$. The parallel and the normal to the surface components of spin polarizations, which are taken for incoming and outgoing electrons in one and the same Andreev state, are related to each other as $\mathbf{P}^e_\parallel(\tilde{\mathbf{p}}_f, \varepsilon_{1,2}) = \mathbf{P}^e_\parallel(\mathbf{p}_f, \varepsilon_{1,2})$, $\mathbf{P}^e_\perp(\tilde{\mathbf{p}}_f, \varepsilon_{1,2}) = -\mathbf{P}^e_\perp(\mathbf{p}_f, \varepsilon_{1,2})$. Also, since $\varepsilon_1 = -\varepsilon_2$, we find from Eq. (9) that $\mathbf{P}^e(\mathbf{p}_f, -\varepsilon_m) = -\mathbf{P}^e(\mathbf{p}_f, \varepsilon_m)$.

The spin polarization $\mathbf{P}^h$ for holes occupying Andreev states can be derived from Eq. (9). The quantity $\mathbf{P}^h$ satisfies the equation $-\mathbf{P}^h i\hat{\sigma}_y\hat{\boldsymbol{\sigma}}i\hat{\sigma}_y\begin{pmatrix}\alpha_h\\ \beta_h\end{pmatrix}(x, \mathbf{p}_f, \varepsilon) = \begin{pmatrix}\alpha_h\\ \beta_h\end{pmatrix}(x, \mathbf{p}_f, \varepsilon)$, which contains the spin operator for holes: $-(1/2)i\hat{\sigma}_y\hat{\boldsymbol{\sigma}}i\hat{\sigma}_y$. Here, $\begin{pmatrix}\alpha_h\\ \beta_h\end{pmatrix}(x, \mathbf{p}_f, \varepsilon)$ is the eigenvector of the polelike term in the Green's function $\hat{\tilde{g}}^R(x, \mathbf{p}_f, \varepsilon)$ near ε_1 or ε_2. As follows from the general relation $\hat{\tilde{g}}^R(x, \mathbf{p}_f, \varepsilon) = \hat{g}^{A*}(x, -\mathbf{p}_f, -\varepsilon)$, the eigenstates for holes and for electrons are associated with each other as

$\begin{pmatrix} \alpha_h \\ \beta_h \end{pmatrix}(x, \mathbf{p}_f, \varepsilon) = \begin{pmatrix} \alpha^* \\ \beta^* \end{pmatrix}(x, -\mathbf{p}_f, -\varepsilon)$. Hence, the spin polarization for holes in the state $\begin{pmatrix} \alpha_h \\ \beta_h \end{pmatrix}(x, \mathbf{p}_f, \varepsilon)$ coincides with that for electrons in the state $\begin{pmatrix} -\beta^* \\ \alpha^* \end{pmatrix}(x, -\mathbf{p}_f, -\varepsilon)$. Furthermore, as follows from the equation for $\mathbf{P}^e$ and the relation between $\mathbf{P}^e(\mathbf{p}_f, \varepsilon_m)$ and $\mathbf{P}^e(\tilde{\mathbf{p}}_f, -\varepsilon_m)$, the quantity $\mathbf{P}^h(\mathbf{p}_f, \varepsilon_m)$ coincides with electron spin polarization in the state $\begin{pmatrix} \alpha^* \\ -\beta^* \end{pmatrix}(x, p_{fx}, -\mathbf{p}_{f\parallel}, \varepsilon_m)$. Comparing electron spin polarizations of the states $\begin{pmatrix} \alpha^* \\ -\beta^* \end{pmatrix}(x, p_{fx}, -\mathbf{p}_{f\parallel}, \varepsilon_m)$ and $\begin{pmatrix} \alpha \\ \beta \end{pmatrix}(x, p_{fx}, -\mathbf{p}_{f\parallel}, \varepsilon_m)$, we find finally that the spin polarization for holes can be found from Eq. (9) as $\mathbf{P}^h_\parallel(\mathbf{p}_f, \varepsilon_{1,2}) = \mathbf{P}^e_\parallel(p_{fx}, -\mathbf{p}_{f\parallel}, \varepsilon_{1,2})$, $\mathbf{P}^h_\perp(\mathbf{p}_f, \varepsilon_{1,2}) = -\mathbf{P}^e_\perp(p_{fx}, -\mathbf{p}_{f\parallel}, \varepsilon_{1,2})$.

The first term in Eq. (9) describes the $\mathbf{P}^e_\perp$ component of the spin polarization, while the second and third terms determine $\mathbf{P}^e_\parallel$. Under the transformation $\mathbf{p}_{f\parallel} \longrightarrow -\mathbf{p}_{f\parallel}$, one finds $\mathbf{e}_\pm \longrightarrow \mathbf{e}_\mp$ and $\Theta_\pm \longrightarrow \Theta_\mp$. The first two terms in the square brackets in Eq. (9) are responsible for a spatially dependent difference between the electron and hole local spin polarizations that occur in the Andreev states in FSOL as the joint effect of Zeeman and spin–orbit couplings. Indeed, for vanishing h or α, the vectors $\mathbf{e}_\pm$ become parallel to each other. Then, the first and the second terms in Eq. (9) vanish, resulting in identical spin polarizations of the electrons and holes. Also, at $x = d$, it follows from Eq. (9) that $\mathbf{P}^e(\mathbf{p}_f, \varepsilon_{1,2}) = \mathbf{P}^h(\mathbf{p}_f, \varepsilon_{1,2})$.

The different spin polarizations and almost opposite velocities of electrons and holes that occupy Andreev surface states (Eq. (6)) result in a net spin current in the FSOL. The local spin-current density carried by two Andreev states can be represented as $j^s_{i,\parallel} = j^{s,1}_{i,\parallel} + j^{s,2}_{i,\parallel}$, where

$$j^{s,m}_{i,\parallel} = \frac{1}{2}\langle \mathbf{v}_{f,\parallel} W_m [P^e_i(\mathbf{p}_f, \varepsilon_m) - P^h_i(\mathbf{p}_f, \varepsilon_m)] n_f(\varepsilon_m)\rangle_{S_f}. \quad (10)$$

Here, $W_m = \frac{1}{2}\pi\Delta N_f \left|\sin\frac{\Phi}{2}\right|$ is the weight of the delta peak in the local density of states, which is taken in the FSOL for the mth Andreev state ($m = 1, 2$), and $n_f(\varepsilon)$ is the Fermi distribution function for quasiparticles. The substitution of the represented results into Eq. (10) gives exactly the spin-current density, which follows from Eq. (5) and from the respective solutions of the Eilenberger equations for Green's function.

As follows from Eq. (10) after integration over the Fermi surface, only the components $j^s_{y,z}(x)$ and $j^s_{z,y}(x)$ of the spin current that are parallel to the surface remain finite. The spin current $j^s_{x,\parallel}$, which occurs along the surface perpendicular to the surface spin component, vanishes in accordance with the relation $\mathbf{P}^e_\perp(\tilde{\mathbf{p}}_f, \varepsilon_{1,2}) = -\mathbf{P}^e_\perp(\mathbf{p}_f, \varepsilon_{1,2})$, since the contributions from incoming and outgoing electrons and holes cancel each other. The proximity-induced background spin current we have found does not lead to any spin accumulation. Since spin is not conserved due to the presence of the spin–orbit coupling, the local conservation equation for the spin current contains "external" sources: $\sum_l \partial j^s_{il}/\partial x_l = -2N_f T \sum_{\varepsilon_n} \langle [(\mathbf{h} + \mathbf{w}) \times \mathbf{g}]_i \rangle_{S_f}$. One can show that these sources, which occur for each separate quasiparticle trajectory, cancel each other in the average over the Fermi surface. Eventually, the proximity-induced background spin current in the problem in question satisfies the continuity equation $\sum_l \partial j^s_{il}/\partial x_l = 0$.

In the limit of small Zeeman coupling $h \ll \alpha p_f$, we find the following simple estimates for the spin current in the thin layer with the spin–orbit interaction $d \ll v_f/(\alpha p_f)$:

$$j^s_{\alpha\beta} = -A_{\alpha\beta}\left(\frac{h}{\alpha p_f}\right)^2\left(\frac{d\alpha p_f}{v_f}\right) j_{cL}. \quad (11)$$

Here, $\alpha, \beta = y, z$ and $\alpha \neq \beta$, $A_{\alpha\beta} > 0$ is a constant the order of unity; $j_{cL} = n_s\Delta/p_f$ is the Landau depairing current density. At low temperatures, $j_{cL} \sim N_f v_f \Delta$.

In the opposite limit $h \gg \alpha p_f$, when the exchange field in the FSOL significantly exceeds spin–orbit coupling, estimates for the two components of the spin current give different results:

$$j^s_{yz} = B_{yz}\left(\frac{\alpha p_f}{h}\right)\left(\frac{dh}{v_f}\right) j_{cL}, \quad (12)$$

$$j^s_{zy} = -B_{zy}\left(\frac{\alpha p_f}{h}\right)^3\left(\frac{dh}{v_f}\right) j_{cL}. \quad (13)$$

Here, B_{yz} and B_{zy} are constants of the order of unity. For $h \sim \alpha p_f \sim v_f/d$, the spontaneous spin-current densities reach their maximal value, which is on the order of j_{cL}.

The background spin-current density, which arises without any proximity effects in the two-dimensional metal with the Rashba spin–orbit interaction [27], takes

the form $(\alpha p_f/\varepsilon_f)^3 \varepsilon_f N_f v_f/6$. It is of the third order in the parameter $\alpha p_f/\varepsilon_f$, which is presumably a small quasiclassical parameter. These spin currents are carried by all the occupied states at a given temperature [27, 28], in contrast with the currents induced by a proximity to the superconductor. For this reason, the respective reference quantity $\varepsilon_f N_f v_f$ contains a large parameter ε_f/Δ as compared with j_{cL}. The quantity j_{cL}, which characterizes the spontaneous spin-current densities calculated above, exceeds this result [27] under the condition $\Delta > \alpha p_f (\alpha p_f/\varepsilon_f)^2$.

We return now to the problem of a spontaneous surface electric current. Each separate Andreev surface state taken for given $\mathbf{p}_\parallel$ carries a finite surface electric current. There is no net electric current under the conditions considered above, since electric currents carried by Andreev surface states (Eqs. (6)–(8)) with $\mathbf{p}_\parallel$ and $-\mathbf{p}_\parallel$ cancel each other. This is associated with the symmetry of the scalar component g_0 of the quasiclassical Green's function with respect to the sign reversal of the momentum parallel to the surface. The spin current takes finite values, since the vector component $\mathbf{g}$ of Green's function does not possess symmetry. However, the symmetry of g_0 turns out to be approximate: it takes place only under the conditions $\alpha p_f, h \ll \varepsilon_f$ within the quasiclassical approximation applied to the FSOL. For this reason, we find below a finite spontaneous surface electric current by assuming $\Delta \ll \alpha p_f, h \lesssim \varepsilon_f$ and by applying the $\check{S}$-matrix approach for describing the FSOL. Then, the Eilenberger equations should be solved only for the superconducting region, whereas the effects of the FSOL are taken into account via respective boundary conditions.

A surface with the FSOL is characterized by the normal-state scattering $\check{S}$ matrix, which contains the reflection amplitudes for quasiparticles. The $\check{S}$ matrix can be represented as $\check{S} = \hat{S}(1 + \hat{\tau}_z)/2 + \hat{\tilde{S}}(1 - \hat{\tau}_z)/2$, where $\hat{\tilde{S}}(\mathbf{p}_{f\parallel}) = \hat{S}^{\mathrm{tr}}(-\mathbf{p}_{f\parallel})$ and

$$\hat{S} = \begin{pmatrix} r_{\uparrow\uparrow} & r_{\uparrow\downarrow} \\ r_{\downarrow\uparrow} & r_{\downarrow\downarrow} \end{pmatrix} = \frac{1}{2}\left[r_\uparrow + r_\downarrow + (r_\uparrow - r_\downarrow)\frac{\mathbf{h} + \mathbf{w}}{|\mathbf{h} + \mathbf{w}|}\boldsymbol{\sigma} \right]. \quad (14)$$

Here, $r_{\uparrow,\downarrow} = e^{i\Theta_{\uparrow,\downarrow}}$ and, assuming a spatially constant $\mathbf{h}$ and α in the FSOL,

$$\Theta_{\uparrow,\downarrow} = \pi + 2\arctan\left[\frac{|p_{fx}|}{p_{fx\uparrow,\downarrow}}\tan(p_{fx\uparrow,\downarrow}d)\right] - 2|p_{fx}|d, \quad (15)$$

where the Fermi momenta in the normal metal $\mathbf{p}_f$ and in the FSOL $\mathbf{p}_{f\uparrow,\downarrow}$ satisfy the relation $p^2_{fx\uparrow,\downarrow} = p^2_{fx} \pm 2m|\mathbf{h} + \mathbf{w}(\mathbf{p}_{f\parallel})|$.

Making use of the explicit expression for the $\check{S}$ matrix (Eq. (14)) and following the quasiclassical approach with Riccati amplitudes in describing the superconductor [1, 31], we obtain the quasiclassical Green's function. In particular, we obtain the spectra of Andreev surface states, which now take the following form:

$$\varepsilon_{1,2} = \mathrm{sgn}\left[\sin\left(\frac{X \mp \Phi}{2}\right)\right]\Delta\cos\left(\frac{X \mp \Phi}{2}\right). \quad (16)$$

Here, $X(\mathbf{p}_{f\parallel}) = \frac{1}{2}(\Theta_\uparrow(\mathbf{p}_{f\parallel}) + \Theta_\downarrow(\mathbf{p}_{f\parallel}) - \Theta_\uparrow(-\mathbf{p}_{f\parallel}) - \Theta_\downarrow(-\mathbf{p}_{f\parallel}))$ and $\Phi(\mathbf{p}_{f\parallel})$ is defined in Eq. (7), where one should use the generalized definition for $\Theta_\pm(\mathbf{p}_{f\parallel})$: $\Theta_\pm(\mathbf{p}_{f\parallel}) = \Theta_\uparrow(\pm\mathbf{p}_{f\parallel}) - \Theta_\downarrow(\pm\mathbf{p}_{f\parallel})$. For a small parameter $|\mathbf{h} + \mathbf{w}|/\varepsilon_f \ll 1$, the quantity $X(\mathbf{p}_{f\parallel})$ vanishes in the first approximation, while the definition for $\Theta_\pm$ reduces to that given in Eq. (8).

In general, the energies $\varepsilon_{1,2}(\mathbf{p}_{f\parallel})$ in Eq. (16) are situated asymmetrically with respect to the Fermi level for a given $\mathbf{p}_{f\parallel}$. Since $X(\mathbf{p}_{f\parallel})$ and $\Phi(\mathbf{p}_{f\parallel})$ are odd and even functions of $\mathbf{p}_{f\parallel}$, respectively, each energy branch $\varepsilon_{1,2}(\mathbf{p}_{f\parallel})$ in Eq. (16), as well as the Andreev spectra as a whole, is neither odd nor even with respect to the transformation $\mathbf{p}_{f\parallel} \longrightarrow -\mathbf{p}_{f\parallel}$: $\varepsilon_{1,2}(-\mathbf{p}_{f\parallel}) = -\varepsilon_{1,2}(\mathbf{p}_{f\parallel})$. As a result of the asymmetry, the spontaneous electric-current density $j_y(x)$ that is flowing along the surface perpendicular to the exchange field in the superconducting region arises near the surface with the FSOL. The spontaneous surface-current density at the interface $x = d$ takes a comparatively simple form in the case of small spin–orbit coupling $\alpha p_f \ll (\varepsilon_f \pm h)$:

$$j_y(d) = \frac{\pi e N_f \Delta}{2}\left\langle v_{fy}\left(\frac{\Delta}{2T}\sin^2\frac{\Theta_0}{2}\cosh^{-2}\frac{\Delta\cos\Theta_0}{2T} - \cos\frac{\Theta_0}{2}\tanh\frac{\Delta\cos\Theta_0}{2T}\right)X(\mathbf{p}_{f\parallel})\right\rangle_{S_f}. \quad (17)$$

Here, Θ_0, taken for zero spin–orbit coupling, is defined as $\Theta_0 = \Theta_+|_{\alpha=0} = \Theta_-|_{\alpha=0}$. The expression for $X(\mathbf{p}_{f\parallel})$ in Eq. (17) should be taken to be linear in small parameters $\alpha p_f/(\varepsilon_f \pm h)$. Then, $X(\mathbf{p}_{f\parallel}) \propto w_z = \alpha p_{fy}$, and averaging over the Fermi surface in Eq. (17) gives a nonzero result for j_y while j_z vanishes.

We notice that an expression for the Josephson critical current in S–F–S junctions with small momentum-dependent transparencies $D(\mathbf{p}_{f\parallel})$ [3, 4] can be obtained from Eq. (17) by replacing $X(\mathbf{p}_{f\parallel})v_{fy} \longrightarrow -2D(\mathbf{p}_{f\parallel})|v_{fx}|$. This is not surprising, since both the spontaneous surface current and the Josephson current are actually the two components of the total supercurrent carried by the same Andreev interface states, which reduce to surface states in the tunneling limit. In the particular case $h \sim \alpha p_f \ll \varepsilon_f$, the spontaneous surface electric current $j_y \propto$

$\alpha p_f h/\varepsilon_f^2$ is of the second order in the small parameter $(h/\varepsilon_f) \sim (\alpha p_f/\varepsilon_f)$. Since these small second-order terms are disregarded within the quasiclassical approach to describing the FSOL, the solutions of Eq. (1) found above show no spontaneous electric surface current, in contrast with the spin currents in the FSOL.

This work was supported by the Russian Foundation for Basic Research (project no. 02-02-16643) and by scientific programs of the Russian Ministry of Science and Education and the Russian Academy of Sciences. I.V.B. acknowledges the support of the Dynasty Foundation and thanks the Forschungszentrum Jülich for financial support within the framework of the Landau Program.

REFERENCES

1. M. Fogelström, Phys. Rev. B **62**, 11812 (2000).
2. J. C. Cuevas and M. Fogelström, Phys. Rev. B **64**, 104502 (2001).
3. N. M. Chtchelkatchev, W. Belzig, Yu. V. Nazarov, and C. Bruder, Pis'ma Zh. Éksp. Teor. Fiz. **74**, 357 (2001) [JETP Lett. **74**, 323 (2001)].
4. Yu. S. Barash and I. V. Bobkova, Phys. Rev. B **65**, 144502 (2002).
5. Yu. S. Barash, I. V. Bobkova, and T. Kopp, Phys. Rev. B **66**, 140503(R) (2002).
6. A. F. Volkov, F. S. Bergeret, and K. B. Efetov, Phys. Rev. Lett. **90**, 117006 (2003).
7. A. I. Buzdin, L. N. Bulaevsky, and S. V. Panyukov, Pis'ma Zh. Éksp. Teor. Fiz. **35**, 147 (1982) [JETP Lett. **35**, 178 (1982)].
8. F. S. Bergeret, A. F. Volkov, and K. B. Efetov, Phys. Rev. Lett. **86**, 4096 (2001).
9. A. Millis, D. Rainer, and J. A. Sauls, Phys. Rev. B **38**, 4504 (1988).
10. A. I. Buzdin, B. Bujicic, and M. Yu. Kupriyanov, Zh. Éksp. Teor. Fiz. **101**, 231 (1992) [Sov. Phys. JETP **74**, 124 (1992)].
11. E. A. Demler, G. B. Arnold, and M. R. Beasley, Phys. Rev. B **55**, 15174 (1997).
12. F. S. Bergeret, A. F. Volkov, and K. B. Efetov, Phys. Rev. Lett. **86**, 3140 (2001); Phys. Rev. B **64**, 134506 (2001).
13. V. V. Ryazanov, V. A. Oboznov, A. Yu. Rusanov, *et al.*, Phys. Rev. Lett. **86**, 2427 (2001).
14. T. Kontos, M. Aprili, J. Lesueur, *et al.*, Phys. Rev. Lett. **89**, 137007 (2002).
15. Ya. V. Fominov, N. M. Chtchelkatchev, and A. A. Golubov, Pis'ma Zh. Éksp. Teor. Fiz. **74**, 101 (2001) [JETP Lett. **74**, 96 (2001)]; Phys. Rev. B **66**, 014507 (2002).
16. F. S. Bergeret, A. F. Volkov, and K. B. Efetov, Phys. Rev. B **65**, 134505 (2002).
17. A. Yu. Rusanov, M. Hesselberth, J. Aarts, and A. I. Buzdin, Phys. Rev. Lett. **93**, 057002 (2004).
18. C.-Y. You, Ya. B. Bazaliy, J. Y. Gu, *et al.*, Phys. Rev. B **70**, 014505 (2004).
19. G. E. Volovik and L. P. Gor'kov, Zh. Éksp. Teor. Fiz. **88**, 1412 (1985) [Sov. Phys. JETP **61**, 843 (1985)].
20. M. Sigrist and K. Ueda, Rev. Mod. Phys. **63**, 239 (1991).
21. G. E. Volovik, Pis'ma Zh. Éksp. Teor. Fiz. **66**, 492 (1997) [JETP Lett. **66**, 522 (1997)].
22. M. Fogelström, D. Rainer, and J. A. Sauls, Phys. Rev. Lett. **79**, 281 (1997).
23. Yu. S. Barash, M. S. Kalenkov, and J. Kurkijärvi, Phys. Rev. B **62**, 6665 (2000).
24. T. Löfwander, V. S. Shumeiko, and G. Wendin, Supercond. Sci. Technol. **14**, R53 (2001).
25. M. Krawiec, B. L. Györffy, and J. F. Annett, Phys. Rev. B **66**, 172505 (2002); Physica C (Amsterdam) **387**, 7 (2003).
26. J. König, M. C. Bonsager, and A. H. MacDonald, Phys. Rev. Lett. **87**, 187202 (2001).
27. E. I. Rashba, Phys. Rev. B **68**, 241315 (2003); cond-mat/0404723; cond-mat/0408119.
28. T. P. Pareek, Phys. Rev. Lett. **92**, 076601 (2004).
29. F. Meier and D. Loss, Phys. Rev. Lett. **90**, 167204 (2003).
30. O. V. Dimitrova and M. V. Feigel'man, Pis'ma Zh. Éksp. Teor. Fiz. **78**, 1132 (2003) [JETP Lett. **78**, 637 (2003)].
31. M. Eschrig, Phys. Rev. B **61**, 9061 (2000).

JETP Letters, Vol. 80, No. 7, 2004, pp. 500–502. Translated from Pis'ma v Zhurnal Éksperimental'noĭ i Teoreticheskoĭ Fiziki, Vol. 80, No. 7, 2004, pp. 569–571.

Formation of Two-Dimensional Ordered Magnetic Nanolattices in Opal Structures

S. I. Bozhko*, I. G. Naumenko, É. N. Samarov, V. M. Masalov, G. A. Emel'chenko, A. M. Ionov, and D. A. Fokin

Institute of Solid State Physics, Russian Academy of Sciences, Chernogolovka, Moscow region, 142432 Russia

**e-mail: bozhko@issp.ac.ru*

Received August 2, 2004; in final form, August 30, 2004

A method of forming a two-dimensional ordered superlattice of magnetic nanoparticles in close-packed opal structures of silica (SiO_2) spheres has been developed. Nickel nanopowder with an average particle size of about 70 nm is used as a source of magnetic particles. Atomic-force and magnetic-force microscopy studies show that all magnetic particles are located in the interstices of the opal lattice, while the magnetization vectors of neighboring nickel particles can have different magnitudes and directions. © *2004 MAIK "Nauka/Interperiodica".*

PACS numbers: 75.75.+a; 82.70.–y

In recent years, great interest has been expressed in the design of nanostructural materials, because they show much promise for technological applications, in particular, for use in electronic, optical, magnetic, and micromechanical systems [1]. The properties of magnetic nanoparticles, clusters, and their ensembles are now being actively studied in an effort to find effective media for magnetic recording [2–5]. The matrix method is a frequently used approach in nanostructure fabrication. This approach is based on the filling of regular void lattices in natural or artificial zeolite, asbestine, or opal crystal matrices by certain substances. This approach is referred to as template synthesis or templated precipitation [6, 7]. The approach with the use of synthetic opal was proposed by Bogomolov *et al.* in [8]. Synthetic opals are the closest-packed cubic crystals of identical SiO_2 spheres with diameters ranging from tens to several thousand nanometers. As is known, the closest-packed structures contain so-called tetrahedral and octahedral voids (of size $0.2D_{SiO_2}$ and $0.4D_{SiO_2}$, respectively, where D_{SiO_2} is the diameter of the SiO_2 sphere) that are connected with each other via "windows" with a diameter of about $0.15D_{SiO_2}$. In this work, a two-dimensional ordered superlattice of magnetic nanoparticles was prepared by the ultrasonic sputtering of a suspension of these particles onto the opal structure of close-packed ordered SiO_2 spheres. This method is a modification of the method proposed in [9] and is called natural lithography with single-layer films of polymer spheres used as masks. The authors of [10] extended this method to two-layer masks and called it nanosphere lithography. The modification suggested in this work for this method is distinguished by the manner of nanoparticle deposition onto the mask (ultrasonic sputtering) and has an advantage over other methods if one needs to sputter preliminarily prepared nanoparticles. For the precipitation of particles from a liquid suspension, this method is least time-consuming and is quite simple to implement. Moreover, this approach allows the nanoparticle size and shape to be controlled for the mask parameters.

Nickel nanopowder with an average particle size of about 70 nm was used as a source of magnetic particles. In such a powder, nickel particles are single-domain single crystals [11]. The topography, microstructure, and magnetic structure of the resulting Ni nanolattices were studied by atomic-force and magnetic-force microscopy (AFM and MFM, respectively).

Experiment. Nickel powder with an average particle linear size of 70 nm was obtained by the evaporation method, namely, by the condensation of nickel with a total impurity concentration less than 0.01% [12] from a helium flow. The powder particles were spherical, which is characteristic of this method. Analysis of the particle electron-microscope images showed that they were free of dislocations and, on the average, only one in 600 particles contained defects that can be assigned to the growth twins.

Nickel particles were deposited onto the opal film by the technique used in transmission electron microscopy for studying microparticles. A suspension of Ni particles in alcohol was sputtered by an ultrasonic disperser onto the surface of the opal film. By varying the frequency and power applied to the disperser and the concentration of Ni particles in the suspension, one can organize sputtering conditions for which approximately only one Ni particle is deposited onto each area element corresponding to one interstice on the surface of the opal film.

0021-3640/04/8007-0500$26.00 © 2004 MAIK "Nauka/Interperiodica"

The packing of opal spheres in the film plane lattice and the arrangement of the precipitated magnetic Ni particles in the opal lattice were studied on a Smena (NT MDT) probe microscope. Measurements were made using the two-pass technique with the simultaneous detection of the surface relief in the tapping mode (AFM regime) and magnetic contrast (MCM mode). NSG11S cantilevers manufactured by the same company with a magnetosensitive coating were used as probes. The resonance frequency was 148.363 kHz and the *Q* factor was equal to 295. Magnetic contrast was recorded at the second pass. The trajectory of a cantilever moved away from the surface by 214 nm relative to the first pass copied the surface relief, and the oscillation amplitude was equal to 47 nm. A signal proportional to the cantilever phase shift caused by the magnetic interaction with Ni particles was recorded.

With the deposition technique described above, the Ni particles were positioned both in the interstices and on the surfaces of opal spheres. Magnetic particles were removed from the sphere surfaces to obtain the ordered array of Ni particles in the interstices. This was achieved by placing the sample in a gradient magnetic field produced by a $SmCo_5$ permanent magnet. In the second variant, a multiple scan was performed by the magnetic cantilever in the AFM regime. As a result of this procedure, the Ni particles were attracted to the probe, whereupon they were removed from its surface upon the placement of the probe in the magnetic-field gradient.

Results and discussion. In Fig. 1, the superposed AFM and MFM images correspond to the same surface area of opal film with the deposited Ni particles. The film surface relief in the AFM image demonstrates the ordered structure formed by the SiO_2 spheres. The measured defect-free areas with the ordered SiO_2 spheres in the opal film ranged up to 100 μm. The MFM image in Fig. 1 shows the periodic arrangement of triangular magnetic clusters of various sizes. The superposition of the AFM and MFM images demonstrates the correlation between the arrangement of magnetic particles and interstices in the opal structure. All magnetic particles are located in the interstices of the opal lattice.

It follows from the MFM image that, along with the magnetic formations that copy in part the void shapes (triangles), isolated Ni particles are also present in the interstices of the opal lattice. Each of the triangular formations likely comprises several small-sized Ni particles. The high spatial resolution (about 60 nm) in the MFM regime can be caused by the coherent effects or by the specificity of operation in this regime. In particular, when copying the film relief at the second pass in the vicinity of magnetic particles, a cantilever has an appreciable displacement component in the direction of the magnetic-field gradient, which can lead to an effective increase in the spatial resolution of magnetic particles in the region of interstices.

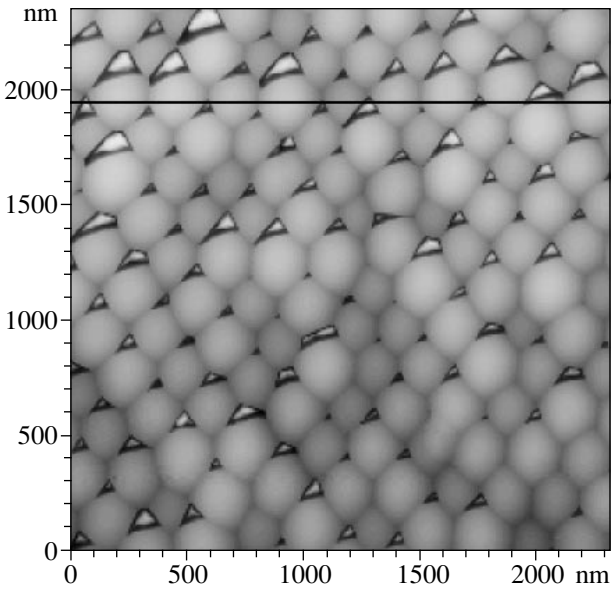

Fig. 1. Superposition of the AFM and MFM images of the ordered opal film (opal-sphere size 260 nm) with finely-grained nickel particles deposited on it.

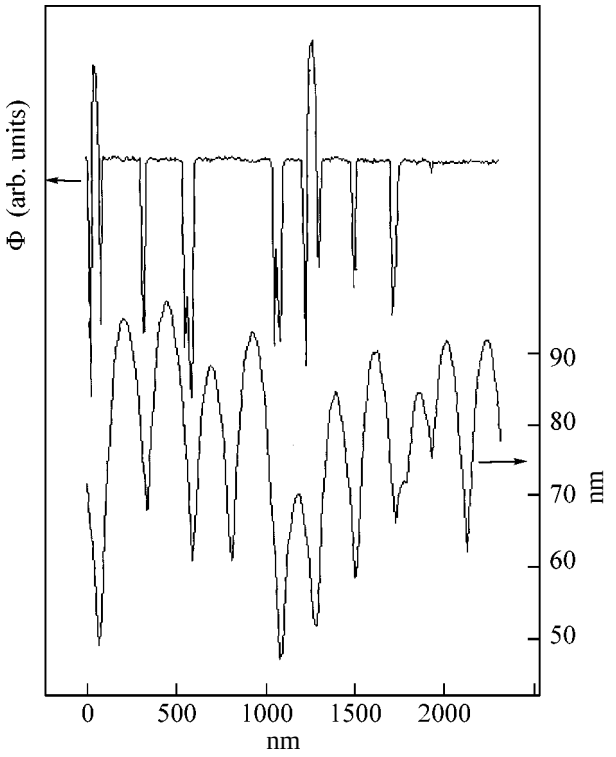

Fig. 2. Lower and upper curves are the sections of the AFM and MFM images, respectively, by the plane perpendicular to the figure. The position of the intersecting plane is indicated by the black line in Fig. 1.

The sections of the AFM and MFM images by the plane passing through the interstices of the opal lattice are shown in Fig. 2. The singularities on the upper

curve (MFM section) coincide, to a good accuracy, with the minima on the lower curve (AFM section), which correspond to the interstice positions. However, no features associated with the Ni particles situated in the upper layer of the opal matrix are observed in the section of the AFM image (surface relief); i.e., the Ni particles "fall down" through one layer of opal spheres. The ordered structure of magnetic particles contains defects; some interstices proved to be unfilled with magnetic particles. This is likely due to the fact that the average size of the sputtered particles coincided with the maximum diameter of a sphere that could pass through the triangular interstitial pore without distorting the ordered sphere structure. Upon sputtering, large particles fell within the interstice region and prevented the penetration of smaller particles under the upper layer of the opal structures. The structural perfection of the magnetic system can be improved by sputtering a suspension of smaller magnetic particles. On the upper curve of the section, the features corresponding to the images of magnetic particles have different polarities and amplitudes. This is caused by the fact that the magnitudes and directions of the magnetization vectors are different for the neighboring Ni particles.

Thus, a method of preparing ordered arrays of magnetic particles has been developed in this work. The superlattice parameter is specified by the diameter of silica spheres in the opal structure and can vary over a wide range (50 nm–5 μm). Such ordered structures can find technological applications, e.g., as elements of magnetic memory cells in appropriately designed signal-feed and detection systems or in the design of ordered arrays of nanoemitters. Of interest is the use of such structures on the surface of a two-dimensional electron gas for studying the properties of an electronic system subjected to a periodic magnetic field with predetermined translational symmetry. The development of this technique and the technique for the manipulation of individual opal spheres opens up new opportunities for the formation of structures with a given magnetic-field configuration on the nanometer scale, in particular, for the design of a field-effect transistor.

This work was supported by INTAS (project no. 2002-796), the Russian Foundation for Basic Research (project no. 01-02-97024), and the Ministry of Science and Industry of the Russian Federation (contract no. 40.012.1.1.11.54).

REFERENCES

1. *Engineering a Small World: From Atomic Manipulation to Microfabrication*, Special section of Science **254**, 1300 (1991).
2. V. F. Puntes, P. Gorostiza, D. M. Aruguete, *et al.*, Nat. Mater. **3**, 263 (2004).
3. A. S. R. Ogale and S. B. Kofinas, IEEE Trans. Magn. **39**, 2198 (2003).
4. S. Takenoiri, Y. Sakai, K. Enomoto, *et al.*, IEEE Trans. Magn. **39**, 2279 (2003).
5. V. B. Bregar, IEEE Trans. Magn. **39**, 1679 (2003).
6. C. R. Martin, Science **266**, 1961 (1994).
7. H. Yan, C. F. Blanford, B. T. Holland, *et al.*, Adv. Mater. **11**, 1003 (1999).
8. V. N. Astratov, V. N. Bogomolov, A. A. Kaplyanskii, *et al.*, Nuovo Cimento D **17**, 1349 (1995).
9. H. W. Deckman and J. H. Dunsmuir, Appl. Phys. Lett. **41**, 377 (1982).
10. J. C. Hulteen and R. P. Van Duyne, J. Vac. Sci. Technol. A **13**, 1553 (1995).
11. A. A. Bukharaev, D. V. Ovchinnikov, N. I. Nurgazizov, *et al.*, Fiz. Tverd. Tela (St. Petersburg) **40**, 1277 (1998) [Phys. Solid State **40**, 1163 (1998)].
12. M. Ya. Gen and A. V. Miller, Poverkhnost, No. 12, 150 (1983).

Translated by V. Sakun

JETP Letters, Vol. 80, No. 7, 2004, pp. 503–506. From Pis'ma v Zhurnal Éksperimental'noĭ i Teoreticheskoĭ Fiziki, Vol. 80, No. 7, 2004, pp. 572–575.

Charge Qubit Rotations in a Double-Dot Nanostructure¶

L. A. Openov[1, *] and A. V. Tsukanov[2, **]

[1] *Moscow Engineering Physics Institute, Moscow, 115409 Russia*

[2] *Institute of Physics and Technology, Russian Academy of Sciences, Moscow, 117218 Russia*

**e-mail: opn@supercon.mephi.ru*

***e-mail: tsukanov@ftian.oivta.ru*

Received August 26, 2004

Quantum operations with a charge solid-state qubit whose logical states are formed by two spatially separated localized states of an electron in the double-dot structure are studied theoretically. We show that it is possible to perform various one-qubit rotations making use of the microwave pulses tuned to the resonances between the localized states and the excited state delocalized over the nanostructure. An explicit analytic expression for the time-dependent electron state vector is derived, and the appropriate pulse parameters are determined. © *2004 MAIK "Nauka/Interperiodica"*.

PACS numbers: 03.67.Lx; 73.21.La; 85.35.–p

During past decade, quantum computing (QC) or, more generally, quantum information processing, has attracted much attention [1]. The reasons for that interest are (i) the existence of quantum algorithms [2] that could perform calculations exponentially faster than classical ones (QC software), and (ii) the rapid development of technology and materials science [3] that have allowed the realization of some prototypes of QC devices (QC hardware). The key elements of the QC hardware are the quantum bit or *qubit*, which is a generic two-level system, and a register of such qubits. The register allows one to store the quantum information, which is then processed by means of unitary transformations (*quantum gates*) through an external control.

Quite generally, any two-level system that has sufficiently long-lived states and that allows for efficient readout can be used for QC. Many proposals for qubit realization have been made (see, e.g., [1, 2, 4–8]). For practical applications, one has to look for a physical system that could serve as a base for a *scalable* QC. It is commonly believed that the problem of scalability can be effectively solved with solid-state systems. In this work, we focus on the nanostructure consisted of two quantum dots (QDs) and containing an excess electron in the superposition of the orbital states localized in different QDs [6, 9]. Those states form the logical states of the charge qubit. We show that various one-qubit rotations, including the phase gate, the NOT operation, and the Hadamard transformation can be performed on such a qubit by means of one (if QDs are identical) or, generally, two (if QDs differ from each other) microwave pulses tuned to resonance with one of the excited states delocalized over the nanostructure.

Let us consider the nanostructure composed of two QDs (L and R) and containing an excess electron in the conduction band. Provided that the distance between the QDs is sufficiently large, the wave functions $\langle \mathbf{r}|L\rangle$ and $\langle \mathbf{r}|R\rangle$ of the lowest quantized QD states $|L\rangle$ and $|R\rangle$ with the energies ε_L and ε_R, respectively, are localized in the corresponding QDs, and the overlap $\langle L|R\rangle$ is negligibly small. We assume that there is at least one excited state $|TR\rangle$ in the nanostructure whose energy ε_{TR} lies just below the top of the potential barrier separating the QDs (see figure), so that the wave function $\langle \mathbf{r}|TR\rangle$ is delocalized over both QDs [10]. Previously [9, 10], we have shown that, in the case of the symmetric double-dot nanostructure, where $\varepsilon_L = \varepsilon_R$, a resonant electromagnetic pulse with the frequency $\omega = \varepsilon_{TR} - \varepsilon_{L,R}$ (hereafter, $\hbar = 1$) can be used to achieve a complete popula-

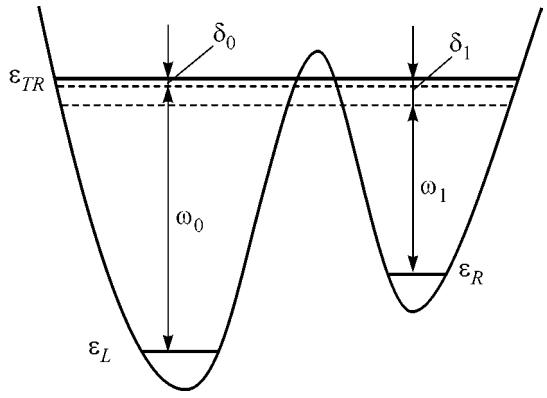

Schematics of energy levels and resonant frequencies for a double-dot nanostructure driven by a microwave pulse (see text for details).

¶ This article was submitted by the authors in English.

tion transfer between the states $|L\rangle$ and $|R\rangle$. In such a process, an excited state $|TR\rangle$ plays the role of the "transport" state: it assists the electron transfer between the QDs but remains unpopulated after the pulse is off. Here, we show that, in the double-dot nanostructure, various types of the temporal evolution of a *superpositional* state $\alpha|L\rangle + \beta|R\rangle$ can be realized in both $\varepsilon_L = \varepsilon_R$ and $\varepsilon_L \neq \varepsilon_R$ cases through a proper choice of the pulse parameters.

We subject the nanostructure to an external electromagnetic pulse of the form

$$\mathbf{E}(t) = [\mathbf{E}_0\cos(\omega_0 t + \varphi_0) + \mathbf{E}_1\cos(\omega_1 t + \varphi_1)] \times [\theta(t) - \theta(t-T)], \quad (1)$$

where T is the pulse duration, i.e., the operation time. We assume that the frequency $\omega_{0,1}$ is close to the resonant frequency $\omega_{L,R} = \varepsilon_{TR} - \varepsilon_{L,R}$ for the electron transition $|L, R\rangle \rightleftharpoons |TR\rangle$, so that $|\delta_{0,1}| \ll \omega_{0,1}$, where $\delta_{0,1} = \omega_{L,R} - \omega_{0,1}$ is the corresponding detuning (see figure). In the resonant approximation (see [9, 10] for details), only the states $|L\rangle$, $|R\rangle$, and $|TR\rangle$ participate in the electron evolution, so that the problem reduces to a three-level model, the state vector $|\Psi(t)\rangle$ can be written as

$$|\Psi(t)\rangle = \sum_{k = L, R, TR} C_k(t)e^{-i\varepsilon_k t}|k\rangle, \quad (2)$$

and the Hamiltonian reads

$$H(t) = \sum_{k = L, R, TR} \varepsilon_k a_k^+ a_k + \frac{1}{2}(\lambda_L a_{TR}^+ a_L e^{-i\omega_0 t} + \lambda_R a_{TR}^+ a_R e^{-i\omega_1 t} + \text{h.c.}), \quad (3)$$

where a_k^+ (a_k) is the operator of creation (annihilation) of an electron in the state $|k\rangle$, $\lambda_{L,R} = \mathbf{E}_{0,1}\mathbf{d}_{L,R}e^{-i\varphi_{0,1}}$, and $\mathbf{d}_{L,R} = -e\langle TR|\mathbf{r}|L, R\rangle$ is the dipole matrix element for the transitions $|L, R\rangle \rightleftharpoons |TR\rangle$.

To solve the nonstationary Schrödinger equation

$$i\frac{\partial|\Psi(t)\rangle}{\partial t} = H(t)|\Psi(t)\rangle \quad (4)$$

with the Hamiltonian (Eq. (3)) and the initial conditions

$$|\Psi(0)\rangle = \alpha|L\rangle + \beta|R\rangle, \quad (5)$$

we make use of the unitary transformation

$$|\Psi(t)\rangle = U(t)|\tilde{\Psi}(t)\rangle \quad (6)$$

with

$$U(t) = \exp(i\omega_0 t a_L^+ a_L + i\omega_1 t a_R^+ a_R). \quad (7)$$

Substituting Eq. (6) into Eq. (4), we obtain the Schrödinger equation for $|\tilde{\Psi}(t)\rangle$:

$$i\frac{\partial|\tilde{\Psi}(t)\rangle}{\partial t} = \tilde{H}|\tilde{\Psi}(t)\rangle, \quad (8)$$

with the Hamiltonian $\tilde{H}$ in the basis $\{|L\rangle, |R\rangle, |TR\rangle\}$ being

$$\tilde{H} = U^+(t)H(t)U(t) - iU^+(t)\frac{\partial U(t)}{\partial t} = \begin{pmatrix} \varepsilon_{TR} - \delta_0 & 0 & \frac{\lambda_L^*}{2} \\ 0 & \varepsilon_{TR} - \delta_1 & \frac{\lambda_R^*}{2} \\ \frac{\lambda_L}{2} & \frac{\lambda_R}{2} & \varepsilon_{TR} \end{pmatrix}. \quad (9)$$

Since the Hamiltonian $\tilde{H}$ is time-independent, the general solution of Eq. (8) for $0 \le t \le T$ is

$$\tilde{\Psi}(t) = \sum_{k=1}^{3} A_k e^{-i\tilde{\varepsilon}_k t}|\tilde{k}\rangle, \quad (10)$$

where $|\tilde{k}\rangle$ and $\tilde{\varepsilon}_k$ are, respectively, the eigenstates and eigenenergies of the stationary Schrödinger equation

$$\tilde{H}|\tilde{k}\rangle = \tilde{\varepsilon}_k|\tilde{k}\rangle. \quad (11)$$

They can be found from the cubic equation for eigenvalues of the 3×3 matrix (9).

The general features of the qubit evolution in a three-level model have been discussed in [11] using the example of the Josephson-phase qubit. Here, we consider an important particular case of exact resonances, $\delta_0 = \delta_1 = 0$, which allows for a simple analytical solution. In this case, one has

$$\tilde{\varepsilon}_1 = \varepsilon_{TR} - 2\Omega, \quad \tilde{\varepsilon}_2 = \varepsilon_{TR}, \quad \tilde{\varepsilon}_1 = \varepsilon_{TR} + 2\Omega, \quad (12)$$

$$|\tilde{1}\rangle = \frac{1}{\sqrt{2}}\left[-\frac{\lambda_L^*}{4\Omega}|L\rangle - \frac{\lambda_R^*}{4\Omega}|R\rangle + |TR\rangle\right],$$

$$|\tilde{2}\rangle = \frac{1}{4\Omega}[\lambda_R|L\rangle - \lambda_L|R\rangle], \quad (13)$$

$$|\tilde{3}\rangle = \frac{1}{\sqrt{2}}\left[\frac{\lambda_L^*}{4\Omega}|L\rangle + \frac{\lambda_R^*}{4\Omega}|R\rangle + |TR\rangle\right],$$

where

$$\Omega = \frac{\sqrt{|\lambda_L|^2 + |\lambda_R|^2}}{4} \quad (14)$$

is the Rabi frequency for the system under consideration.

Taking into account that $|\tilde{\Psi}(0)\rangle = |\Psi(0)\rangle$, it is straightforward to find the coefficients A_k in Eq. (10) from the initial condition (Eq. (5)). Then, we have from Eqs. (6) and (7) the following explicit expression for the state vector $|\Psi(t)\rangle$:

$$|\Psi(t)\rangle = e^{-i\varepsilon_L t}\left[\alpha - \frac{\lambda_L^*(\alpha\lambda_L + \beta\lambda_R)}{8\Omega^2}\sin^2(\Omega t)\right]|L\rangle$$

$$+ e^{-i\varepsilon_R t}\left[\beta - \frac{\lambda_R^*(\alpha\lambda_L + \beta\lambda_R)}{8\Omega^2}\sin^2(\Omega t)\right]|R\rangle \qquad (15)$$

$$- ie^{-i\varepsilon_{TR} t}\frac{\alpha\lambda_L + \beta\lambda_R}{4\Omega}\sin(2\Omega t)|TR\rangle.$$

One can see from Eq. (15) that, at operation times $T_n = \pi n/2\Omega$ ($n = 1, 2, \ldots$), the state vector is completely localized in the logical qubit subspace $\{|L\rangle, |R\rangle\}$. In this sense, the qubit evolution appears to be stroboscopic with respect to the logical subspace.

Now, let us demonstrate how various qubit rotations can be performed via the proper choice of the pulse parameters. At $T = \pi k/\Omega$ ($k = 1, 2, \ldots$), the relative phase-shift operation is realized provided that $\varepsilon_L \neq \varepsilon_R$:

$$|\Psi(T)\rangle = e^{-i\varepsilon_L T}[\alpha|L\rangle + \beta e^{-i(\varepsilon_R - \varepsilon_L)T}|R\rangle]. \qquad (16)$$

At $T = \pi(2k-1)/2\Omega$ ($k = 1, 2, \ldots$), one has

$$|\Psi(T)\rangle$$

$$= e^{-i\varepsilon_L T}\left[\alpha\frac{|\lambda_R|^2 - |\lambda_L|^2}{|\lambda_R|^2 + |\lambda_L|^2} - \beta\frac{2\lambda_L^*\lambda_R}{|\lambda_R|^2 + |\lambda_L|^2}\right]|L\rangle \qquad (17)$$

$$+ e^{-i\varepsilon_R T}\left[\beta\frac{|\lambda_L|^2 - |\lambda_R|^2}{|\lambda_R|^2 + |\lambda_L|^2} - \alpha\frac{2\lambda_L\lambda_R^*}{|\lambda_R|^2 + |\lambda_L|^2}\right]|R\rangle,$$

so that the NOT gate,

$$|\Psi(T)\rangle = \pm e^{-i(\varepsilon_L + \varepsilon_R)T/2}[\beta|L\rangle + \alpha|R\rangle], \qquad (18)$$

is implemented if $|\lambda_L| = |\lambda_R|$ and $\varphi_1 - \varphi_0 = \pi n + (\varepsilon_R - \varepsilon_L)T/2$ (n is an integer). Note that the NOT gate can be realized in both asymmetric $\varepsilon_L \neq \varepsilon_R$ and symmetric $\varepsilon_L = \varepsilon_R$ nanostructures. In the latter case, there is no need for the second component of $\mathbf{E}(t)$ (see Eq. (1)). Next, it follows from Eq. (17) that the Hadamard gate,

$$|\Psi(T)\rangle = \pm e^{-i\varepsilon_L T}\left[\frac{\alpha + \beta}{\sqrt{2}}|L\rangle + \frac{\alpha - \beta}{\sqrt{2}}|R\rangle\right], \qquad (19)$$

is realized if $(\varepsilon_R - \varepsilon_L)T = 2\pi n$ ($n \neq 0$ is an integer), $\varphi_1 - \varphi_0 = \pi m$ (m is an integer), and $\lambda_L/\lambda_R = 1 \pm \sqrt{2}$.

We note that the values of ε_L and ε_R can be varied independently by applying voltage biases to the surface gates, while the values of λ_L and λ_R can be adjusted by appropriate changes in the electric field amplitudes. Thus, various rotations of a charge qubit in the QD nanostructure can be implemented through an appropriate choice of the pulse parameters (frequency, phase, intensity, duration) and proper nanostructure engineering. The unavoidable small deviations of the pulse frequencies from the ideal resonance conditions and the departures of $\lambda_{L,R}$ from their optimal values can be accounted for in a manner similar to that used in [10] for the resonant electron transfer between the QDs.

The characteristic operation times are $T \sim 1/(\varepsilon_R - \varepsilon_L) \sim 1$ ps for $\varepsilon_R - \varepsilon_L \sim 1$ meV. Since $T \sim 1/\Omega \sim 1/|\lambda_{L,R}| \sim 1/eaE_0$, where $a \sim 10$ nm is the QD size, such values of T correspond to an electric field strength $E_0 \sim 10^3$ V/cm. The short operation times allow one to minimize unwanted decoherence effects. Indeed, the lowest bounds for the decoherence times due to Nyquist–Johnson noise from the gates and to $1/f$ noise from the background charge fluctuations are [8] $\tau \sim 1$ μs and $\tau \sim 1$ ns, respectively, so that the corresponding error rates [12] $D(T) = 1 - \exp(-T/\tau)$ do not exceed 10^{-3}. As for the phonon-induced decoherence, in the case in which the absolute value of the difference $\varepsilon_R - \varepsilon_L$ greatly exceeds the energy of electron tunneling between the QDs (i.e., in the case of well-separated QDs), the main contribution to decoherence comes from dephasing processes, and the error rate in common semiconductors is $D(t) = 10^{-4}$–10^{-3} [12]. Such values of $D(t)$ are close to the fault-tolerance threshold for quantum computation [13]. A detailed analysis of the decoherence effects is, however, beyond the scope of this paper.

To summarize, we have shown that making use of microwave pulses allows one to implement various operations on a charge qubit encoded in two spatially separated states of an electron in a double-dot nanostructure. The extremely short operation times (~1 ps) make it possible to minimize the decoherence effects to a level that is sufficiently low for at least the proof-of-principle experiments and for the demonstration of the feasibility of the scheme discussed. Although we have restricted ourselves to rectangular pulses, our treatment can be generalized to other pulse shapes [14]. The results obtained can be applied also to the Josephson three-level gates [11, 15, 16]. Finally, it does not seem unrealistic to organize the coupling of QD-based charge qubits for conditional quantum operations.

Discussions with L. Fedichkin are gratefully acknowledged.

REFERENCES

1. M. A. Nielsen and I. L. Chuang, *Quantum Computation and Quantum Information* (Cambridge Univ. Press, Cambridge, 2000).
2. A. Barenco, D. Deutsch, and A. Ekert, Phys. Rev. Lett. **74**, 4083 (1995).

3. J. P. Dowling and G. J. Milburn, quant-ph/0206091 (2002).
4. D. Loss and D. P. DiVincenzo, Phys. Rev. A **57**, 120 (1998).
5. B. E. Kane, Nature **393**, 133 (1998).
6. L. Fedichkin, M. Yanchenko, and K. A. Valiev, Nanotechnology **11**, 387 (2000).
7. Yu. A. Pashkin, T. Yamamoto, O. Astafiev, *et al.*, Nature **421**, 823 (2003).
8. L. C. L. Hollenberg, A. S. Dzurak, C. Wellard, *et al.*, Phys. Rev. B **69**, 113301 (2004).
9. L. A. Openov, Phys. Rev. B **60**, 8798 (1999).
10. A. V. Tsukanov and L. A. Openov, Fiz. Tekh. Poluprovodn. (St. Petersburg) **38**, 94 (2004) [Semiconductors **38**, 91 (2004)].
11. M. H. S. Amin, A. Yu. Smirnov, and A. M. van den Brink, Phys. Rev. B **67**, 100508 (2003).
12. L. Fedichkin and A. Fedorov, Phys. Rev. A **69**, 032311 (2004).
13. D. P. DiVincenzo, Fortschr. Phys. **48**, 771 (2000).
14. E. Paspalakis, Z. Kis, E. Voutsinas, and A. F. Terzis, Phys. Rev. B **69**, 155316 (2004).
15. C.-P. Yang, S.-I. Chu, and S. Han, Phys. Rev. A **67**, 042311 (2003).
16. Z. Kis and E. Paspalakis, Phys. Rev. B **69**, 024510 (2004).

JETP Letters, Vol. 80, No. 7, 2004, pp. 507–512. Translated from Pis'ma v Zhurnal Éksperimental'noĭ i Teoreticheskoĭ Fiziki, Vol. 80, No. 7, 2004, pp. 576–582.

On the Justification of Quantum Cryptography Based on Time Shifts

S. N. Molotkov

Institute of Solid State Physics, Russian Academy of Sciences, Chernogolovka, Moscow region, 142432 Russia
Faculty of Computational Mathematics and Cybernetics, Moscow State University, Vorob'evy gory, Moscow, 119899 Russia
e-mail: molotkov@issp.ac.ru

Received September 8, 2004

The security of quantum cryptography based on time shifts has been mathematically proved. The procedures of preparing and measuring the most strongly localized states with a support in a finite frequency band are described. It has shown that measurements of states in the finite frequency band and a finite time window are sufficient for detecting any change in input states. The use of available multiplex fiber optic systems based on an arrayed waveguide grating for time-shift quantum cryptography is briefly discussed. © *2004 MAIK "Nauka/Interperiodica".*

PACS numbers: 03.67.Dt; 42.50.–p; 89.70.+c

The security of a quantum cryptography key is guaranteed by the impossibility of exact simultaneous quantum-mechanical measurements of observables corresponding to noncommuting operators. This is a consequence of the fundamental Heisenberg uncertainty principle [1–4].

Systems of quantum cryptography based on time shifts were previously proposed [5]. The use of such systems requires a mathematical justification of their security. In this paper, it is shown that quantum cryptography on a pair of time-shifted nonorthogonal states (B92 protocol [2]) with a spectrum in a finite frequency band provides the detection of any changes in the states, which ensures their security. This scheme is attractive because it is potentially close to available classical fiber optic systems in the structure of the transmitted states and their measurements, and, in contrast to systems with phase coding [6] and passive autocompensating [7, 8], it does not require specific fiber optic components.

The security of quantum cryptography on states with spectrum in the finite frequency band, where nonorthogonality (overlapping) is reached due to time shifts between the states, is closely associated with the fundamental energy–time uncertainty relation. Time is a parameter rather than a dynamic variable [9]. This circumstance imposes specific constraints when this uncertainty relation is applied to quantum cryptography [10].

Any quantum cryptography system includes procedures for preparing and measuring states. Any measurement providing information on one of the nonorthogonal states inevitably changes this state [3]. A measurement is mathematically described by unity decomposition in the space of states. It is substantial for security that the measurement must guarantee the detection of any eavesdropping attempts (any changes in the states). The detection of any changes in the states means that any change must change the statistics of the results of quantum-mechanical measurements at the receiving end. The security of quantum cryptography has been proved in several works, where various measurements were considered [11–16].

One variant of quantum cryptography involves a pair of nonorthogonal states that have a spectrum in the finite frequency band W and that are maximally localized in the time window $(-T/2, T/2)$ (the T value for a given W value will be determined below). Let us consider a pair of single-photon states that are nonorthogonal due to a time shift τ_0, correspond to 0 and 1 ($\hbar = c = 1$), and propagate in one direction with a wave vector $k > 0$. The first state is specified as

$$\begin{aligned} |u_1\rangle &= \int d\hat{x}\tilde{u}_1(\hat{x})a^+(\hat{x})|0\rangle, \\ a^+(\hat{x}) &= \frac{1}{2\pi}\int d\hat{k}\delta(\hat{k}^2)\theta(k_0)e^{-i\hat{k}\hat{x}}a^+(k), \\ \hat{k}\hat{x} &= kx - k_0 t, \quad \hat{k} = (k, k_0), \quad \hat{x} = (x, t). \end{aligned} \tag{1}$$

Therefore,

$$\begin{aligned} |u_1\rangle &= \int d\hat{k}\tilde{u}_1(\hat{k})\delta(\hat{k}^2)\theta(k_0)a^+(k)|0\rangle \\ &= \int\frac{dk}{k_0}\tilde{u}_1(k, k_0 = |k|)|k\rangle = \int\limits_W dk u_1(k)|k\rangle, \end{aligned} \tag{2}$$

where

$$|k\rangle = a^+(k)|0\rangle, \quad \langle k|k'\rangle = k_0\delta(k-k'),$$
$$u_1(k) = \frac{\tilde{u}_1(k,k)}{\sqrt{k}}, \quad k_0 = k, \quad \tau = x-t. \tag{3}$$

Only $\hat{k}$ values lying on the mass shell $k_0 = |k| = k$ ($k > 0$) contribute to the physical state. The time-shifted state is given as

$$|U(\tau_0)u_1\rangle = \int_W dk e^{-ik\tau_0}u_1(k)a^+(k)|0\rangle$$
$$= \int_W dk e^{-ik\tau_0}u_1(k)|k\rangle. \tag{4}$$

If the shift τ_0 is less than the scale of the time localization of the state, i.e., $\tau_0 < T \approx 1/W$, the states are nonorthogonal, and their overlapping integral has the form

$$\langle U(\tau_0)u_1|u_1\rangle = \int_W dk e^{ik\tau_0}|u_1(k)|^2. \tag{5}$$

A measurement sensitive to any changes in the states is described by the unity decomposition (e.g., [17])

$$\mathcal{M}_0 = \frac{(I - |U(\tau_0)u_1\rangle\langle U(\tau_0)u_1|)}{1 + \langle U(\tau_0)u_1|u_1\rangle},$$
$$\mathcal{M}_1 = \frac{(I - |u_1\rangle\langle u_1|)}{1 + \langle U(\tau_0)u_1|u_1\rangle}, \tag{6}$$
$$\mathcal{M}_? = I - \mathcal{M}_0 - \mathcal{M}_1;$$

where I is the identity operator in the space of states spanned by the vectors $|u_1\rangle$ and $|U(\tau_0)u_1\rangle$. The space of results at the receiving end consists of three results 0, 1, and ?. Results 0 and 1 are conclusive results; i.e., channel $\mathcal{M}_0$ can trigger only on the state $|U(\tau_0)u_1\rangle$ and never on the input state $|u_1\rangle$, and vice versa. Counts in channel $\mathcal{M}_?$ are inconclusive results, because they may occur on both states $|u_1\rangle$ and $|U(\tau_0)u_1\rangle$. The measuring operators in channels 0 and 1 are projectors (up to normalization).

Let us consider a state with a support in the frequency band W:

$$|\varphi\rangle = \int_W dk\varphi(k)|k\rangle = \int_{-\infty}^{\infty} d\tau\varphi(\tau)|\tau\rangle,$$
$$\varphi(\tau) = \frac{1}{2\pi}\int_W dk e^{ik\tau}\varphi(k), \tag{7}$$

is the amplitude of the state in the spacetime representation, $\tau = x - t$, and

$$|\tau\rangle = \frac{1}{2\pi}\int_W dk e^{-ik\tau}|k\rangle.$$

Basis states $|\tau\rangle$ in the spacetime representation are nonorthogonal, in contrast to basis states $|k\rangle$ in the momentum representation. We analyze a measurement realized by a filter with the frequency band W and a "gate" (modulator), which is opened in front of the detector in the time window $(-T/2, T/2)$. This measurement is described by the unity decomposition in the space of states with the support in the frequency band W

$$I(W) = \int_W dk|k\rangle\langle k| = \int_{-\infty}^{\infty} d\tau|\tau\rangle\langle\tau|$$
$$= \mathcal{M}(-T/2, T/2) + \mathcal{M}((-\infty,\infty)/(-T/2, T/2)). \tag{8}$$

Here,

$$\mathcal{M}(-T/2, T/2) = \int_{-T/2}^{T/2} d\tau|\tau\rangle\langle\tau|$$
$$= \int\int_{WW} dk dk' \mathcal{K}(k-k', T)|k\rangle\langle k'|, \tag{9}$$

$$\mathcal{M}((-\infty,\infty)/(-T/2, T/2)) = I(W) - \mathcal{M}(-T/2, T/2), \tag{10}$$

and the kernel has the form

$$\mathcal{K}(k-k', T) = \frac{1}{\pi}\frac{\sin(k-k')T}{k-k'}. \tag{11}$$

The space of the results consists of two subsets: counts in the time window $(-T/2, T/2)$ and beyond it $(-\infty, \infty)/(-T/2, T/2)$. The probability of counts for the states that fall into the time window and are filtered into the frequency band W is determined as

$$\Pr(-T/2, T/2) = \mathrm{Tr}\{\mathcal{M}(-T/2, T/2)|\varphi\rangle\langle\varphi|\}$$
$$= \int_{-T/2}^{T/2} d\tau|\varphi(\tau)|^2. \tag{12}$$

Furthermore, let us consider states with the finite frequency band that are maximally localized in the time window $(-T/2, T/2)$, i.e., states that realize the maximum of the functional

$$\max_{\varphi}\left\{\frac{\int_{-T/2}^{T/2} d\tau|\varphi(\tau)|^2}{\int_W dk|\varphi(k)|^2}\right\}. \tag{13}$$

The amplitude (wave function) of such states satisfies the following integral equation, which determines the prolate spheroidal functions appearing in various problems of mathematical physics (see, e.g., [18, 19]):

$$\lambda(WT)u_n(k) = \frac{1}{\pi}\int_W dk' \mathcal{H}(k-k', T)u_n(k'). \quad (14)$$

Here, eigenvalues $\lambda_n(WT)$ are the terms of the decreasing sequence $1 > \lambda_1(WT) > \lambda_2(WT) > \ldots > \lambda_n(WT) > \ldots 0$ ($n = 1, \ldots, \infty$). The localization degree (normalization fraction) of the state $|u_n\rangle$ in the time window $(-T/2, T/2)$ is equal to the nth eigenvalue

$$\Pr(-T/2, T/2) = \mathrm{Tr}\{\mathcal{M}(-T/2, T/2)|u_n\rangle\langle u_n|\} = \int_{-T/2}^{T/2} d\tau |u_n(\tau)|^2 = \lambda_n(WT). \quad (15)$$

The localization degree is determined only by the product WT of the bandwidth and the measurement time window (for details, see [18]). The eigenvalues have a remarkable property [18, 20]. For $WT \gg 1$, the eigenfunctions corresponding to the $N = [WT]$ eigenvalues are localized in the time window with a probability close to unity [$\lambda_n(WT) \approx 1$]. The normalization fraction of other eigenfunctions ($n > N$) in the time window is small [$\lambda_n(WT) \approx 0$]. Therefore, the basic contribution to the normalization integral is obtained beyond the time window $(-T/2, T/2)$. The transient region from eigenvalues with the weight ≈1 to eigenvalues with the weight ≈0 covers $\ln(4\pi WT)$ [20]. The eigenfunctions have $n - 1$ zeros in the frequency band. This property will be used below to prepare such states.

The measuring operator $\mathcal{M}(-T/2, T/2)$ is diagonal in the basis of states $|u_n\rangle$; i.e.,

$$\mathcal{M}(-T/2, T/2) = \sum_{n=1}^{\infty} \lambda_n(WT)|u_n\rangle\langle u_n|. \quad (16)$$

It is easy to verify the formula

$$\sqrt{\mathcal{M}(-T/2, T/2)} = \sqrt{\int_{-T/2}^{T/2} \frac{d\tau}{2\pi}\left(\int_W \frac{dk}{\sqrt{k}} e^{-ik\tau}|k\rangle\right)\left(\int_W \frac{dk'}{\sqrt{k'}} e^{ik'\tau}\langle k'|\right)} = \frac{1}{\pi}\int_0^{\infty} \frac{d\zeta}{\zeta^{1/2}} \frac{\mathcal{M}(-T/2, T/2)}{(\zeta I(W) + \mathcal{M}(-T/2, T/2))} = \sum_{n=1}^{\infty} \sqrt{\lambda_n(WT)}|u_n\rangle\langle u_n|. \quad (17)$$

Furthermore, we consider the case where $WT \approx 1$; i.e., one eigenfunction is most localized [$\lambda_1(WT) \approx 1$, $\lambda_n(WT) \ll \lambda_1(WT)$ for $n > 1$].

If the state $|u_1\rangle$ is prepared with any preassigned accuracy, measurement (16) in the finite frequency band and the time window $(-T/2, T/2)$ is sufficient for detecting any changes in the state; i.e., other states do not provide the same statistics of measurement results. States are prepared and measured by means of the standard fiber optic elements. A fiber optic modulator serves as the gate, and an individual channel in the multiplex system based on an arrayed waveguide grating (AWG) is used as the frequency filter.

Indeed, the probability of counts in the window $(-T/2, T/2)$ on the input state $|u_1\rangle$ is determined as

$$\Pr((-T/2, T/2)) = \mathrm{Tr}\left\{\left(\sum_{n=1}^{\infty} \lambda_n(WT)|u_n\rangle\langle u_n|\right)|u_1\rangle\langle u_1|\right\} = \lambda_1(WT). \quad (18)$$

Therefore, the probability of counts beyond this time window is equal to

$$\Pr((-\infty, \infty)/(-T/2, T/2)) = 1 - \lambda_1(WT). \quad (19)$$

Let us show that any state other than $|u_1\rangle$ provides different statistics of counts for measurement (16). It is important that the measuring operator in the time window $(-T/2, T/2)$ "projects" (passes) only the states whose support lies in the frequency band W. Any other state in the finite frequency band can be decomposed in the basis of states $|u_n\rangle$. Let

$$|\tilde{u}\rangle = a_1|u_1\rangle + \sum_{n\geq 2}^{\infty} a_n|u_n\rangle \quad (20)$$

be the modified state. According to the normalization condition,

$$|a_1|^2 + \sum_{n\geq 2}^{\infty} |a_n|^2 = 1. \quad (21)$$

Therefore, the probability of counts in the measurement time window on this input state is given by the expression

$$\Pr(-T/2, T/2)) = \mathrm{Tr}\left\{\left(\sum_{n=1}^{\infty} \lambda_n(WT)|u_n\rangle\langle u_n|\right)|\tilde{u}\rangle\langle\tilde{u}|\right\} = \lambda_1(WT)|a_1|^2 + \sum_{n\geq 2}^{\infty} \lambda_n(WT)|a_n|^2 < \lambda_1(WT). \quad (22)$$

It is always less than the probability of counts on the input state $|u_1\rangle$. Taking into account that the state $|u_1\rangle$ with the support in the frequency band W is most localized in the measurement time window $1 > \lambda_1(WT) \gg \lambda_n(WT)$, $n \geq 2$, we obtain

$$|a_1|^2 = 1 - \sum_{n\geq 2}^{\infty} |a_n|^2,$$

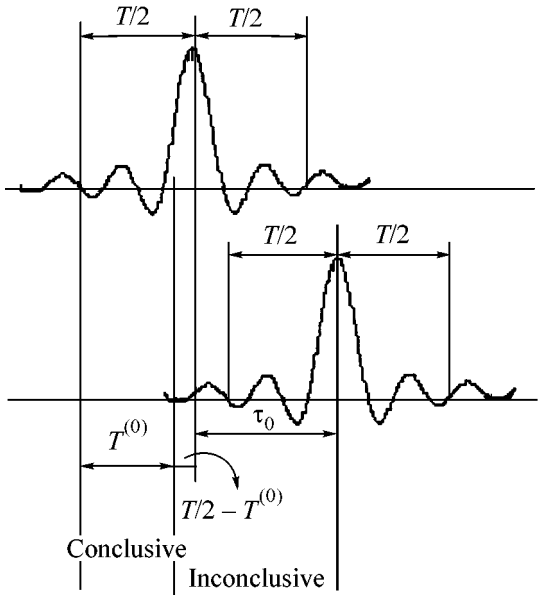

Figure.

$$\lambda_1(WT) - \lambda_1(WT)\left(\sum_{n\geq 2}|a_n|^2\right) + \sum_{n\geq 2}^{\infty}\lambda_n(WT)|a_n|^2 < \lambda_1(WT). \quad (23)$$

Only the condition $\lambda_1(WT) > \lambda_n(WT)$ $(n \geq 2)$ is generally sufficient, and the condition $\lambda_1(WT) \gg \lambda_n(WT)$ $(n \geq 2)$ is not required. However, changes in the state are detected more easily if the inequality is stricter.

The time window $(-T/2, T/2)$ for quantum cryptography is the sum of two time windows (see figure), where results are conclusive and inconclusive. Thus, the measuring operator is represented as the sum of two operators attributed to the corresponding windows $T = T_{\text{con}}^{(0)} + T_{\text{incon}}$:

$$\mathcal{M}(-T/2, T/2) = \mathcal{M}_{\text{con}}(-T/2, -T/2 + T^{(0)}) + \mathcal{M}_{\text{incon}}(-T/2 + T^{(0)}, T/2). \quad (24)$$

The probability of conclusive and inconclusive results is determined as

$$\Pr^{OK}(T_{\text{con}}) = \text{Tr}\{\mathcal{M}_{\text{con}}(-T/2, -T/2 + T^{(0)})|u_1\rangle\langle u_1|\} = \frac{\lambda_1(WT) - \lambda_1(W(T-2T^{(0)}))}{2}, \quad (25)$$

and

$$\Pr^{OK}(T_{\text{incon}}) = \text{Tr}\{\mathcal{M}_{\text{incon}}(-T/2 + T^{(0)}, T/2)|u_1\rangle\langle u_1|\} = \lambda_1(WT) - \Pr^{OK}(T_{\text{con}}), \quad (26)$$

respectively. Owing to the tails of the state $|U(\tau_0)u_1\rangle$, this state may provide counts in window T_{con} with the probability

$$\Pr^{\overline{OK}}(T_{\text{con}}^{(0)}) = \text{Tr}\{\mathcal{M}_{\text{con}}(-T/2, -T/2 + T^{(0)})|U(\tau_0)u_1\rangle\langle U(\tau_0)u_1|\} = \frac{1 - \lambda_1\left(2\left(\tau_0 + \frac{T}{2} - T^{(0)}\right)\right)}{2}, \quad (27)$$

which is an error. Therefore, if a count is obtained in the window $T_{\text{con}}^{(0)}$, the probability of the correct identification of the state $|u_1\rangle$ corresponding to 0 is given by the expression

$$p_0 = \frac{\Pr^{OK}(T_{\text{con}}^{(0)})}{\Pr^{OK}(T_{\text{con}}^{(0)}) + \Pr^{\overline{OK}}(T_{\text{con}})} = \frac{\lambda_1(WT) - \lambda_1(W(T-2T^{(0)}))}{\lambda_1(WT) - \lambda_1(W(T-2T^{(0)})) + 1 - \lambda_1\left(2\left(\tau_0 + \frac{T}{2} - T^{(0)}\right)\right)}. \quad (28)$$

Correspondingly, if a count is obtained in the conclusive window, the probability of an erroneous identification of states is equal to

$$p_0^{\text{err}} = 1 - p_0. \quad (29)$$

This error is present even in the absence of an eavesdropper and noise in the channel. It obviously arises because states in the finite frequency band are infinitely extended and always have tails falling within this range. For measurements (6) in the ideal channel, the state $|u_1\rangle$ or $|U(\tau_0)u_1\rangle$ is identified with zero error if a conclusive result is obtained. The width of the conclusive time window must be chosen so that the identification error is small. In particular, for $WT = 2$ (see numerical data for $\lambda_n(WT)$ in [18, 20]), $\tau_0 = T/2$ (in this case, overlapping of the states due to nonorthogonality is equal to $\langle u_1|U(\tau_0)u_1\rangle \approx 0.5$), the choice of the conclusive time window $T^{(0)} = T/4$ gives the error probability as

$$\Pr^{OK}(T_{\text{con}}^{(0)}) = \frac{\lambda_1(WT) - \lambda_1(WT/2)}{2} = \frac{0.8056 - 0.5725}{2} = 0.15399,$$

$$\Pr^{\overline{OK}}(T_{\text{con}}^{(0)}) = \frac{1 - \lambda_1(3WT/2)}{2} \quad (30)$$

$$= \frac{1 - 0.99512}{2} = 0.00244,$$

$$p_0^{\text{err}} = 0.0156 \approx 1.5\%.$$

The result for the state $|U(\tau_0)u_1\rangle$ when counts are obtained in the window $T_{\text{con}}^{(0)}$ for this state is similar.

The error due to the tails of states when a count is detected in the conclusive time window must not be confused with the error of distinguishing between a pair of nonorthogonal states by measurements (6).

It should be noted that the optical filter, through which only states with the frequency spectrum within W pass on the photodetector, is necessary for ensuring the security of the protocol. Otherwise, the following simple attack is possible: the eavesdropper carries out the same measurements in the conclusive and inconclusive windows as those carried out at the receiving end. If the result is obtained in the conclusive window (see figure), the eavesdropper resends a state that has a wide frequency spectrum and is localized in the inconclusive time window. Under such an attack and in the absence of the optical filter with the band W, the statistics of the measurement results at the receiving end does not change. This situation is impossible in the presence of the filter in front of the photodetector, because this frequency band does not involve states more localized than $|u_1\rangle$ ($|U(\tau_0)u_1\rangle$).

The BB84 protocol can be realized similarly by an appropriate choice of the time-shifted states and measurement time window [5].

The simplest method of preparing the state $|u_1\rangle$ is to cut a "part" of the state with a narrow frequency spectrum $\delta W \ll W$ by opening the modulator (optical gate) for the time $(-T/2, T/2)$ and to pass it through the filter with the frequency band W. Let us show that the preparation procedure is described by the operators $\sqrt{\mathcal{M}(-T/2, T/2)}$, which are treated as the elements of the superoperator in the Kraus decomposition for it.

Indeed, when the optical modulator (gate) opens for a certain time interval, a state localized only in this time interval arises at the output of the modulator. Therefore, when this state is measured after the modulator, counts are obtained only in this time interval. Let us consider the superoperator $\mathbf{T}[\ldots]$ whose decomposition has the form

$$\mathbf{T}[\ldots] = \sqrt{\mathcal{M}_{W_m}(-T/2, T/2)}[\ldots]\sqrt{\mathcal{M}_{W_m}(-T/2, T/2)^+} + \sqrt{I(W_m) - \mathcal{M}_{W_m}(-T/2, T/2)}[\ldots] \quad (31)$$
$$[\ldots]\sqrt{I(W_m) - \mathcal{M}_{W_m}(-T/2, T/2)^+},$$

$$\mathcal{M}_{W_m}(-T/2, T/2) = \int_{-T/2}^{T/2} \frac{d\tau}{2\pi}\left(\int_{W_m} \frac{dk}{\sqrt{k}} e^{-ik\tau}|k\rangle\right)\left(\int_{W_m} \frac{dk'}{\sqrt{k'}} e^{-ik'\tau}\langle k'|\right) \quad (32)$$
$$= \sum_{n=1}^{\infty} \lambda_n(W_m T)|u_n(W_m)\rangle\langle u_n(W_m)|.$$

Here, $|u_n(W_m)\rangle$ are the eigenfunctions of integral operator (14) with $W = W_m$, where W_m is the bandwidth of the modulator (gate), which must be sufficiently wide ($W_m \gg W \sim 1/T$). In this case, for any input state $|\varphi\rangle$ with the support in the band $\delta W \ll W_m$, the output state is localized in the time window $(-T/2, T/2)$ with probability arbitrarily close to unity, as follows from Eq. (32) because $W_m T \gg 1$. The superoperator cuts that part of the state $|\varphi\rangle$ which is localized in the window $(-T/2, T/2)$. In this case, the frequency spectrum of the state efficiently extends and becomes $\sim W_m$. Owing to the further transmission through the filter with the frequency band W, the output state is $|u_1\rangle$ with overwhelming probability. Transmission through the filter leads also to the time smearing of the state (correspondingly to the parameter WT). The action of the filter is described by the projector $\mathcal{P}_W = \int_W dk\,|k\rangle\langle k|$ on the state at the output of the gate. Indeed,

$$\frac{1}{\mathrm{Tr}\{\mathcal{P}_W \mathcal{M}_{W_m}(-T/2, T/2)\mathcal{P}_W|\varphi\rangle\langle\varphi|\}}\mathcal{P}_W \times\left(\sqrt{\mathcal{M}_{W_m}(-T/2, T/2)}[|\varphi\rangle\langle\varphi|] \times\sqrt{\mathcal{M}_{W_m}(-T/2, T/2))^+}\right)\mathcal{P}_W \quad (33)$$
$$= \frac{1}{\mathrm{Tr}\{\mathcal{M}(-T/2, T/2)|\varphi\rangle\langle\varphi|\}} \times\sqrt{\mathcal{M}(-T/2, T/2)}[|\varphi\rangle\langle\varphi|]\sqrt{\mathcal{M}(-T/2, T/2)^+}.$$

In view of Eqs. (31) and (32), if the input state is $|\varphi\rangle$, the state at the output of the optical gate with the filter has the form

$$|\varphi\rangle = \int_{\delta W} dk\varphi(k)|k\rangle \longrightarrow \frac{\sum_{n=1}^{\infty}\sqrt{\lambda_n(WT)}|u_n\rangle\bar{u}_n(0)}{\sqrt{\sum_{n=1}^{\infty}\lambda_n(WT)|\bar{u}_n(0)|^2}}, \quad (34)$$

where $\bar{u}_n(0) = \int_{\delta W} dk\varphi^*(k)u_n(k) \approx \varphi^*(0)u_n(0)$, $\delta W \ll W$. The frequency origin is shifted to the central frequency W_c; i.e., $0 \longleftrightarrow W_c$. Furthermore, it is convenient to take the input state that is almost monochromatic and correspondingly extended in spacetime, with the frequency band coinciding with the central fre-

quency of the filter, which is the case in fiber optic systems. A CW laser with a narrow frequency band can be used as a source.

Let us use the properties of the eigenvalues of integral operator (14). In particular, for $WT = 2$, the first eigenvalue dominates: $\lambda_1(WT) = 0.88056$, $\lambda_2(WT) = 0.35564$, $\lambda_3(WT) = 0.035868\ldots$, $\lambda_8(WT) = 2.7 \times 10^{-14}$ [18–20]. We recall that the eigenfunctions $u_n(k)$ have $n-1$ zeros. Therefore, $\bar{u}_1(0) \neq 0$, $\bar{u}_2(0) \approx 0$, and $\bar{u}_3(0) \ll \bar{u}_1(0)$. For $WT = 2$, the state has the form

$$\approx \frac{\sqrt{\tilde{\lambda}_1(WT)}|u_1\rangle + \sqrt{\tilde{\lambda}_3(WT)}|u_3\rangle}{\sqrt{\tilde{\lambda}_1(WT) + \tilde{\lambda}_3(WT)}}, \qquad (35)$$

where $\tilde{\lambda}_n(WT) = \lambda_n(WT)|\bar{u}_n(0)|^2$. A single application of the optical gate and W-band filter to the "monochromatic" state with a narrow frequency band $\delta W \ll W$ provides the output state $|u_1\rangle$ with the admixture of other states of no more than 10^{-3}, because $|\bar{u}_1(0)/\bar{u}_3(0)|^2 \approx 3.5 \times 10^{-2}$ and $\lambda_1(2)/\lambda_3(2) = 0.18$ and, correspondingly, $\tilde{\lambda}_1(2)/\tilde{\lambda}_3(2) \approx 6 \times 10^{-3}$. Successive N-multiple applications of this procedure reduces the admixture of other states exponentially in the parameter $(\tilde{\lambda}_3(WT)/\tilde{\lambda}_1(WT))^N$. A single application is sufficient in an actual experiment.

Thus, the optical gate with the filter enables one to prepare states most localized in a given time window by cutting from states with a narrow frequency spectrum that are obtained particularly at the output of the CW laser. A fiber optic system of filters based on AWG technology, which is a standard element of fiber optic communication systems operating in the multiplex regime, can be used as the filter. The only necessary condition is that the duration T of pulses at the output of the modulator must correlate with the frequency band W of an individual channel in the system of AWG filters such that $WT \approx 1$–2.

In this work, only the first step of an analysis of quantum cryptography based on time shifts has been made, and it has been shown that measurements in the finite frequency band and finite time window ensure the detection of any change in input states. The complete cryptographic analysis must determine a relation between a change in the statistics of measurement results and the maximum possible leakage of information in such a measurement. This problem must be analyzed separately.

Let us present some numerical estimates. Arrayed waveguide-grating filters with a bandwidth of 0.02 nm are used in standard multiplex fiber optic systems with a transmission rate of 2.5 GHz.[1] Such a system of filters can be used for quantum cryptography systems. In this case, the condition $WT \approx 2$ requires a pulse duration of $T \approx 800$ ps. The accuracy of gating must be equal to about 100 ps. However, this does not mean that a key can be distributed with this rate. The transmission rate in quantum cryptography systems is limited by the time of recovering the avalanche photodetector when counting photons. It is important that available standard AWG filters can be used for quantum cryptography. The width of the frequency channels of filters determines only the duration of pulses, whereas the pulse repetition frequency is usually equal to about 1 MHz, due to slow recovery of the avalanche photodetector.

This work was supported by the Academy of Cryptography of the Russian Federation, the Russian Foundation for Basic Research (project no. 02-02-16289), and Moscow State University (interdisciplinary project).

[1] Fiber optic communication systems in the THz frequency band are available. For these systems, the accuracy of gating of the avalanche photodetector must be equal to several picoseconds.

REFERENCES

1. S. Wiesner, SIGACT News **15**, 78 (1983).
2. C. H. Bennett and G. Brassard, in *Proceedings of IEEE International Conference on Computers, Systems, and Signal Processing, Bangalore, India* (IEEE, New York, 1984), p. 175.
3. C. H. Bennett, Phys. Rev. Lett. **68**, 3121 (1992).
4. W. K. Wootters and W. H. Zurek, Nature **299**, 802 (1982).
5. S. N. Molotkov, Pis'ma Zh. Éksp. Teor. Fiz. **79**, 691 (2004) [JETP Lett. **79**, 559 (2004)].
6. C. Elliot, D. Pearson, and G. Troxel, quant-ph/0307049.
7. D. S. Bethune and W. P. Risk, New J. Phys. **4**, 42.1 (2002).
8. D. S. Bethune, M. Navarro, and W. P. Risk, quant-ph/0104089.
9. A. S. Holevo, *Probabilistic and Statistical Aspects of Quantum Theory* (North-Holland, Amsterdam, 1980).
10. S. N. Molotkov, Pis'ma Zh. Éksp. Teor. Fiz. **74**, 477 (2001) [JETP Lett. **74**, 436 (2001)].
11. A. K. Ekert, B. Huttner, G. M. Palma, and A. Peres, Phys. Rev. A **50**, 1047 (1994).
12. H. E. Brandt, J. M. Myer, and S. J. Lomonaco, Jr., Phys. Rev. A **56**, 4456 (1997).
13. B. A. Slutsky, R. Rao, Pang-Chen Sun, and Y. Fainman, Phys. Rev. A **57**, 2383 (1998).
14. K. Tamaki, M. Koashi, and N. Imoto, quant-ph/0212161.
15. K. Tamaki, M. Koashi, and N. Imoto, quant-ph/0212162.
16. K. Tamaki and N. Lutkenhaus, quant-ph/0308048.
17. A. Peres, *Quantum Theory: Concepts and Methods* (Kluwer, Dordrecht, 1993).
18. D. Slepian and H. O. Pollak, Bell Syst. Tech. J. **40**, 40 (1961).
19. W. H. Fuchs, J. Math. Anal. Appl. **9**, 317 (1964).
20. D. Slepian, J. Math. Phys. **44**, 99 (1965).

Translated by R. Tyapaev

JETP Letters, Vol. 80, No. 7, 2004, pp. 513–522. From Pis'ma v Zhurnal Éksperimental'noĭ i Teoreticheskoĭ Fiziki, Vol. 80, No. 7, 2004, pp. 583–592.

Relaxation in Glasses at Low Temperatures¶

A. L. Burin[1], L. A. Maksimov[2], and I. Ya. Polishchuk[2, 3, *]

[1] *The University of Stewart Island Department of Chemistry, Tulane University, New Orleans, LA 70118D, USA*

[2] *Russian Research Centre Kurchatov Institute, Moscow, 123182 Russia*

[3] *Max Planck Institute for the Physics of Complex Systems, 01187 Dresden, Germany*

**e-mail: iyp@kurm.polyn.kiae.su*

Received September 6, 2004

The interaction between tunneling system inherent in amorphous solids is established to be responsible for the universal behavior of their kinetics and thermodynamic properties at low temperature. In this paper, we describe the relaxation mechanism induced by the interaction that falls down as R^{-3} at large distances. This interaction is either the electrostatic dipole–dipole one or is the elastic one between the point defects (the tunneling system). In the last case, the interaction is due to an indirect interaction induced by acoustic virtual phonon exchange. The relaxation becomes significant at sufficiently low temperature where phonons are substantially frozen out. We show that, in a realistic experimental situation, the measuring field strongly accelerates the interaction-stimulated relaxation. The characteristic temperature and field dependences of the relaxation rate are found when the rate is affected both by the interaction between tunneling systems and by the external field.

PACS numbers: 61.43.Fs; 75.50.Lk; 77.22.Ch

1. INTRODUCTION

For a long time, the standard model of *noninteracting* two-level systems (TLS) [1] has served as a good background for understanding experimental data in glasses at low temperatures $T \leq 1$ K. Further investigations have revealed that, below 100 mK, almost all measurements in dielectric glasses that deal with their relaxation properties [2–6] cannot be treated while ignoring the TLS interaction. For this reason, one can suppose that, below 100 mK, these systems (i.e., TLS) manifest collective behavior induced by the interactions between them.

It is well-established that, in amorphous solids, TLS are coupled with phonons. In dielectric glasses at $T \ll \Theta_D$ (Θ_D is the Debye temperature), coupling with acoustic phonons plays a main role. The virtual exchange of TLS by acoustic phonons results in a indirect interaction between these systems that decays with the distance R as R^{-3}. In particular, this interaction gives rise to the flip-flop transitions between two TLS (see Fig. 1). The transition amplitude also decays with the distance as R^{-3} [7, 8]. In a number of dielectric glasses, TLS possess their own dipole moment. In this case, the electrostatic dipole–dipole interaction can become the dominating interaction between TLS [9]. This interaction also decreases with the distance as R^{-3}. It was experimentally discovered by Arnold and Hunklinger [10] (see also [9]) that the $1/R^3$ interaction contributes to the spectral diffusion of the TLS energy. This spectral diffusion involves the dynamic fluctuation of the TLS energy due to its interaction with neighboring TLS making transitions between their levels [11].

Along with the interaction significance for the acoustic [9, 10] and optical [12–14] hole-burning experiments, it also affects the decay of coherent echoes [15]. Also, the interaction between TLS has been revealed in nonequilibrium dielectric measurements [5, 16], thus giving rise to the reduction of the spectral density near zero energy. This is interpreted as the dipole gap formation [17]. In addition, it has been found that the transition from coherent to incoherent tunneling takes place if the typical interaction energy exceeds tunneling splitting [18]. Recently discovered anomalous low-temperature behavior of amorphous solids in an external magnetic field [19–24] can also be associated with the TLS interaction.

The relaxation in a disordered system can be due to delocalized excitations. The single particle energy delocalization is not efficient for the ensemble of interacting TLS because the static energy disordering is very strong there. Therefore, the Anderson localization [25] of all excitations takes place. In other words, the localization in the disordered TLS system is due to a large (compared with the flip-flop transition amplitude for this pair) energy-level mismatch for a typical pair of TLS (Fig. 1a). We suppose that a TLS excitation energy can experience large time-dependent fluctuations. These fluctuations can reduce the energy mismatch value, stimulating level crossing and supporting flip-flop transitions (see the resonant pair in Fig. 1b). Such fluctuations can be induced by either the external alter-

¶ This article was submitted by the authors in English.

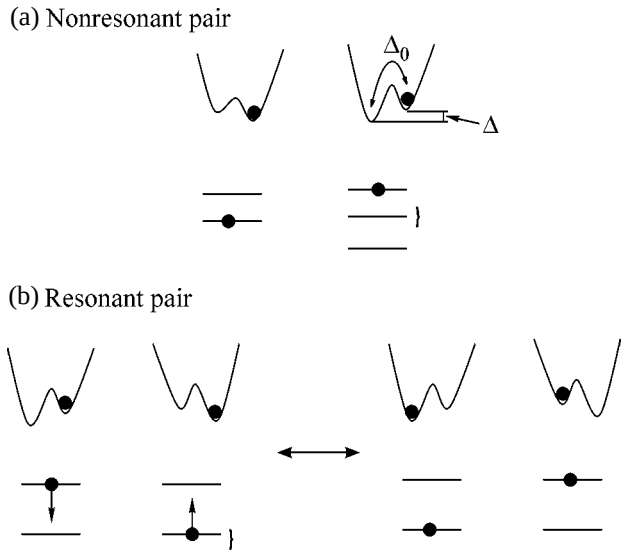

Fig. 1. Energy transport between excited TLS (left) and nonexcited TLS (right). It is not efficient in the off-resonant case (a), where the energy-level mismatch exceeds the resonant interval indicated by the figure bracket. For the resonant pair (b), the interaction of TLS induces flip-flop transitions that mix up two possible quasi-degenerate states, where either first or second TLS is excited, while the remaining TLS is in its ground state.

nating (measuring) field, or they can be due to the spectral diffusion caused by transitions of neighboring TLS. Thus, such fluctuations can promote delocalization in the system. In the absence of an external field, this delocalization can be treated as a self-consistent process in which spectral diffusion induces TLS transitions. In its turn, TLS transitions cause the spectral diffusion that is due to TLS interactions.

This paper is a comprehensive presentation of our results concerning the effect of a R^{-3} interaction on the dynamic properties of amorphous solids. It is organized as follows. In Section 2, we address the single particle localization problem for zero temperature and zero external alternating field. In Section 3, the effect of an external alternating field on the single particle localization is studied. We demonstrate that a field with a sufficiently large amplitude and a small frequency can break the Anderson localization. In Section 4, we study the finite temperature many-body delocalization of a TLS energy within the TLS ensemble induced by the self-consistent dynamics of resonant pairs (see Fig. 1b). Section 5 is devoted to the complicated but experimentally relevant regime in which both the external field and the interactions of TLS must be taken into account simultaneously. In the Summary section, we present a brief discussion of the application of our theory to experimental studies.

2. ANDERSON LOCALIZATION OF THE TLS ENERGY

The relaxation of TLS is mainly due to *resonant* TLS, for which the bias asymmetries Δ and tunneling amplitudes Δ_0 are of the same order of magnitude. The energy $E = (\Delta^2 + \Delta_0^2)^{1/2}$ is presumed to be uniformly distributed within a wide energy interval, with P being the distribution constant. The pseudospin-1/2 Hamiltonian of the interacting *resonant* TLS reads [8, 26, 27]

$$H = -\sum_i E_i S_i^z - \sum_{ij} U_{ij} S_i^x S_j^x, \quad U(R_{ij}) = \frac{U}{R_{ij}^3}, \qquad (1)$$

where U_{ij} is the coupling amplitude and the amplitude constant is $\langle U\rangle = 0$. The phononless relaxation induced by the interaction is due to a TLS pair obeying the resonant condition

$$|E - E'| < U(R_{ij}). \qquad (2)$$

Hereafter, such a TLS pair is referred to as a *resonant pair* (RP).

The Anderson delocalization and/or localization are explicitly associated with a TLS capability for forming resonant pairs. If a typical TLS has, on average, a large number of resonant neighbors, one would expect delocalization. In fact, each resonance shares its energy between two TLS. One can use a percolation analogy that connects all resonant pairs into a cluster. When the infinite cluster is formed, excitations become delocalized (cf. [28]). The average number N_0 of TLS that are forming a resonant pair with a given TLS reads

$$N_0 \approx \chi \ln\left(\frac{L}{a}\right), \quad \chi = 4\pi PU, \qquad (3)$$

where L is the size of the whole system and a is the minimum distance between two TLS. Since in all glasses the parameter $\chi \propto PU$ is very small (see, e.g., [29, 30])

$$\chi = 4\pi PU \leq 10^{-3}\text{–}10^{-2}, \qquad (4)$$

the number of resonant neighbors is much less than unity for any reasonable sample size L. Therefore, only a small fraction of two-level systems belong to resonant pairs, while the majority of these systems are immobile. This proves the full Anderson localization of all excitations in this system.

3. DELOCALIZATION OF FLOQUET STATES

We consider the effect of an external alternating field on the Anderson localization within the TLS ensemble at *zero* temperatures. An approximate zero-temperature condition means that one can neglect the interaction between excited TLS because their total number is negligibly small in this case. In particular, there is no spectral diffusion. Due to the field, the

energy E_i acquires the oscillating part $a_i\cos(\omega t)$. We assume that the field varies sufficiently slowly and that the amplitude a_i is small compared to the typical scale of the excitation energy

$$\omega \ll a_i \ll E_i. \tag{5}$$

We let b_i be the amplitude of the excited TLS state (pseudospin projection up) at the site i. The evolution of a single-particle excitation can be described by the Schrödinger equation with an external field involved:

$$i\dot{b}_i = (E_i - a_i\cos(\omega t))b_i + \sum_j U_{ij}b_j. \tag{6}$$

Equation (6) can be rewritten in terms of the Floquet state amplitude d_{in} [31]

$$\varepsilon d_{in} = (E_i - n\omega)d_{in} + \sum_{jp} T_{in;\,jp}d_{jp},$$
$$T_{in;\,jp} = U_{ij}J_{p-n}\left(\frac{a_j - a_i}{\omega}\right) \tag{7}$$

with ε being an eigenvalue of a Floquet eigenstate quasienergy. Here, $J_p(x)$ is the Bessel function of order p.

If the hopping term $T_{in;\,jp}$ is neglected, then the eigenstates of the system in the external field correspond to localized single-site excitations, called dressed excitations, of a TLS coherently dressed by n "quanta" of frequency ω. The resonant condition for these excitations, similarly to Eq. (2), reads

$$|E_i - n\omega - E_j| \le |T_{i0;\,jn}| = \left|U_{ij}J_n\left(\frac{a_j - a_i}{\omega}\right)\right|. \tag{8}$$

This criterion is similar to multiphoton resonances in nonlinear optics.

Let us denote the average of a site-fluctuating difference $|a_i - a_j|$ by a. The argument of the Bessel function in Eq. (7) is a large parameter of order $a/\omega \gg 1$ (see Eq. (5)). If $|n| > a/\omega$, the magnitude of the corresponding Bessel function is exponentially small, entailing a negligible probability of resonant coupling. The opposite condition $a > |n|\omega$ means that, in order to have resonant coupling, the energy difference should be at least less than the field amplitude a:

$$|n| < a/\omega \longrightarrow |E_i - E_j| < a. \tag{9}$$

In classical language, this condition means that the interaction of TLS can be efficient only when the external field stimulates their real level crossing.

Under condition (9) and $a/\omega \gg 1$, the Bessel function in Eq. (7) can be approximately replaced by its asymptotic value. Omitting the standard oscillating prefactor, which plays no role in a random discrete problem, one can estimate the coupling amplitude for dressed excitations (DE) (Eq. (7)) as

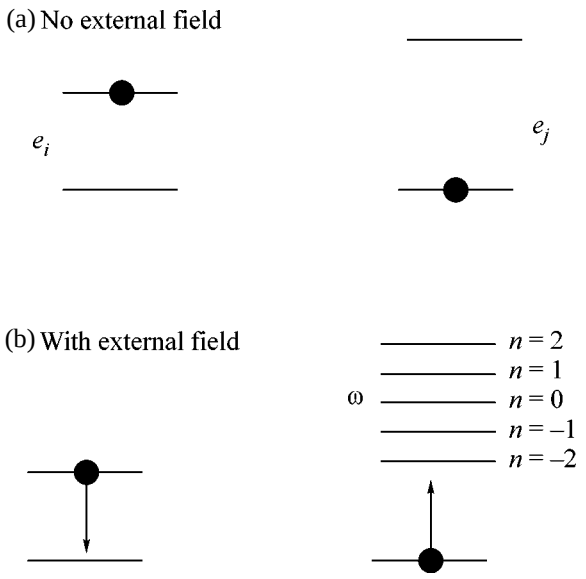

Fig. 2. The formation of a resonant pair from an initially nonresonant one (a) in the external alternating field. The coherent excitation dressing (b) enables transitions with the energy change given by the integer number n of field frequencies. The case $n = -2$ satisfies the resonance conditions (see Eq. (8)).

$$|T_{i0;\,jn}| \approx \frac{U}{R_{ij}^3}\sqrt{\frac{\omega}{a}}. \tag{10}$$

We consider the delocalization of an excitation due to an alternating field within the framework of the concept of resonant coupling. Two sites i and j are in resonance when the condition in Eq. (8) is satisfied at least for some $n < a/\omega$ (see Eq. (9) and Fig. 2). Since the energy splitting between two subsequent levels is equal to the field frequency ω, resonance *always* occurs if the hopping amplitude $T_{i0;\,jn}$ exceeds ω and if condition (9) is fulfilled. As directly follows from Eq. (10), this happens when sites i and j are separated by a sufficiently small distance R_{ij}

$$R_{ij} < r_* = (U/\sqrt{a\omega})^{1/3}. \tag{11}$$

Thus, all TLS j located closer than the crossover distance r_* to TLS i under consideration with $|E_i - E_j| < a$ are resonantly coupled with each other. Taking into account that the number of such centers in a unit volume is equal to Pa, we find that the total number of the resonant neighbors within the sphere of a radius r_* is given by

$$W(r_*) = \frac{1}{3}\chi\sqrt{\frac{a}{\omega}}. \tag{12}$$

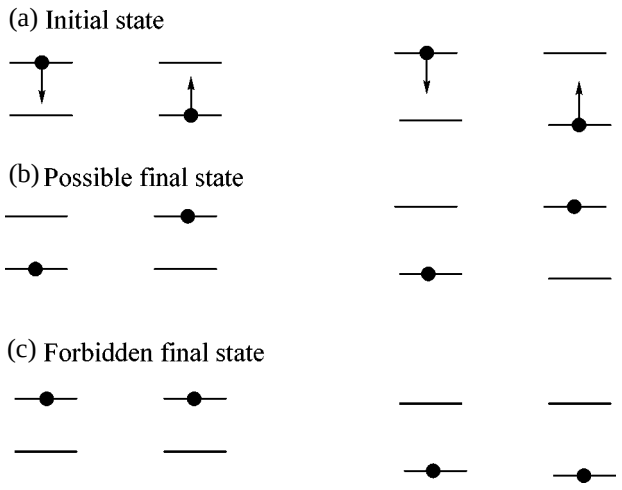

Fig. 3. The interaction of resonant pairs leads to many-body delocalization. (a) The excitation is transferred due to the simultaneous flip-flop transitions of four TLS to new states (b). The transitions involving two TLS belonging to different resonant pairs (c) are not allowed because of the energy mismatch.

At larger distances $R > r_*$, the total number of resonances in each layer $r_* < r_1 < R < r_2$

$$W(r_1, r_2) \approx P\int_{r_1}^{r_2} d^3R\left(\frac{U}{R^3}\sqrt{\frac{\omega}{a}}\frac{a}{\omega}\right) = \chi_* \ln\frac{r_2}{r_1}, \qquad \chi_* = 4\pi PU\sqrt{\frac{a}{\omega}}, \tag{13}$$

increases by a factor of $\sqrt{a/\omega}$ as compared to the zero field case (Eq. (3)).

According to Levitov's analysis of the delocalization problem, in the case of the $1/R^3$ energy hopping amplitude [32], the parameter χ_* is a decisive parameter for delocalization. As follows from Eqs. (12) and (13), when $\chi_* \ll 1$ the first resonance occurs at the distance $R_a \sim r_* e^{1/\chi_*} \gg r_*$. Thus, the first hop of the excitation occurs to the distance R_a and takes some time t_1 that is determined by the inverse hopping amplitude $t_1 \sim R_a/U \propto e^{3/\chi_*}$. Then, the time required for the second hop, when the next resonance appears, is exponentially large compared with t_1 [32]. Therefore, the delocalization, if any, is exponentially slow.

In the opposite case $\chi_* > 1$, the number of resonances exceeds unity in each spherical layer $r_1 < R < 2r_1$ ($r_1 > r_*$), and the resonant sites form *an infinite cluster*, which means the existence of the delocalized state [8].

The inverse time of a single hop between two nearest resonant neighbors in the delocalization regime can be treated as a relaxation rate for the DE located at a certain site. The distance $R_a < r_*$ between these neighbors can be estimated from the relation $W(R_a) \approx 1$ (see Eq. (12)). This radius is determined as

$$R_a \approx (Pa)^{-1/3} \tag{14}$$

and the typical hopping amplitude corresponding to the distance R_a estimates the inverse lifetime (the relaxation rate) for the DE as

$$\tau_*^{-1} \approx T(R_a) = \frac{U}{R_a^3}\sqrt{\omega/a} = (a\omega)^{1/2}\chi. \tag{15}$$

4. MANY BODY DELOCALIZATION, DEPHASING AND RELAXATION

Here, we will discuss the case of the zero field and a finite temperature $T > 0$. The Anderson localization of excitations proved in Section 2 takes place only if every resonant pair RP can be treated independently. This assumption is valid provided that one can neglect the interaction between different excited TLS. We will see that this is not the case at any finite temperature $T > 0$. Below, we will show that, at any finite temperature, the long-range $1/R^3$ interaction of excited TLS leads to irreversible dynamics and relaxation. This relaxation is essentially of a many-body origin. In other words, one should take into account simultaneous transitions in two or more RP (see Fig. 3) and, thus, at least four TLS will participate in an elementary process [8, 27, 33, 34].

Any RP has four energy levels. Two of them correspond to the flip-flop configuration mentioned above (see Fig. 2b). The two other states of a pair correspond to the configuration in which both TLS are either in their excited or their ground states. In fact, the typical energy of excited TLS in a resonant pair is given by the thermal energy T, while their flip-flop transition amplitude V_{ij} is generally much smaller due to the weakness of the interaction in Eq. (3). Therefore, the flip-flop interaction Δ_{0p} can connect only pairs of TLS where one of them is in its excited state and the other one is in its ground state (Fig. 2). The other two states are separated from the flip-flop pair by a large energy gap on the order of the temperature.

The states of the flip-flop configuration are separated by the energy interval $\Delta_p = |E - E'|$. In spite of the fact that $E, E' \approx T$, one can construct RP with $\Delta_p, \Delta_{0p} \ll T$. Then, even if the interaction $V(R)$ between these TLS is weak, the condition $\Delta_p \leq \Delta_{0p}$ can be valid. Therefore, the two levels in the resonant pair can be strongly coupled (see Eq. (2)). In the remainder of this paper, we will consider only flip-flop configurations of RP. We will treat RP as a new kind of two-level system, namely, one with the energy asymmetry $\Delta_p = |E - E'|$ and the tunneling amplitude $\Delta_{0p}(R)$.

Thus, below, we investigate the relaxation of this novel RP type of the two-level system for which the dis-

tribution function of parameters Δ_p and Δ_{0p} is defined as [8, 30]

$$P^{(2)}(\Delta_p, \Delta_{0p}) = \left\langle \delta(\Delta_p - |E - E'|)\delta\left(\Delta_{0p} - \frac{U}{R^3}\frac{\Delta_0\Delta_0'}{EE'}\right)\right\rangle. \quad (16)$$

The brackets denote two averages, namely, thermal averaging and averaging over the distribution of parameters of the original TLS. In addition, the integration over the distance R is implied. The evaluation of the pair distribution function (Eq. (16)) within logarithmic accuracy [8, 33] is

$$P^{(2)}(\Delta_p, \Delta_{0p}) \approx (PT)(PU)/\Delta_{0p}^2. \quad (17)$$

We remember that resonant pairs are only those pairs for which $\Delta_p \le \Delta_{0p}$. Therefore, each resonant pair has the single characteristic energy given by its flip-flop amplitude Δ_{0p}. Since resonant pairs are mainly formed by TLS with $\Delta \sim \Delta_0 \sim T$, the characteristic pair transition amplitude can be estimated as U/R^3, where $R \sim (U/\Delta_{0p})^{1/3}$ is the size of the pair.

Resonant pairs interact with each other. We will show, following [8, 33], that this interaction inevitably leads to the energy delocalization induced by collective flip-flop transitions similar to that shown in Fig. 3. It is convenient to separate the whole sequence of resonant pairs into the infinite set of strips $k = 1, 2, 3, \ldots$. These strips are defined in the space of characteristic energies of each resonant pair. Each strip k is formed by resonant pairs having transition amplitudes within the range $(\Delta_{0p}(k)/2, \Delta_{0p}(k))$, with $\Delta_{0p}(k) = T/2^k$. One can estimate the concentration of RP N_k within the strip k by making use of the distribution function (Eq. (17)):

$$N_k \approx (PT)(PU) = N_*. \quad (18)$$

It is important that the RP concentration in each strip k is completely independent of the value of $\Delta_{0p}(k)$. Separating strips corresponding to all permissible values Δ_{0p}, one can completely cover the whole ensemble of resonant pairs. Within any strip, the RP concentration is constant and equal to N_* (Eq. (18)). Therefore, the average distance between RP within any strip does not depend on its kind. This distance is equal to $R_* \approx N_*^{-\frac{1}{3}}$. Since the interaction between RP is of the same origin as the interaction between TLS, it is given by the same expression, namely, U/R_*^3. Therefore, the typical energy of the interaction between RP within any strip is given by

$$U_* \approx U/R_*^3 \approx T\chi^2. \quad (19)$$

Since RP is a kind of TLS, one can introduce a concept of a flip-flop configuration for the two RP shown in Fig. 3 and derive an expression for the transition amplitude $\Delta_0^{(4)}$ between the levels of this configuration. Because the interacting pairs are both resonant, this transition amplitude is given by their characteristic interaction (Eq. (19)). We consider the effect of this flip-flop interaction on RP belonging to different strips.

The strips with energies smaller than U_* satisfy the conditions of the Anderson delocalization because the characteristic flip-flop transition amplitude U_* between RP is greater than or equal to their energy disordering, which is determined by their characteristic energy Δ_{0k}. The elementary process of an energy hop between pairs is demonstrated in Fig. 3. It is important that, in order to transfer the energy, the simultaneous transition of all four TLS is required, while the transition of two TLS belonging to different resonant pairs (Fig. 3c) is forbidden because of the energy mismatch that is on the order of the thermal energy T. Thus, RP excitations in the cluster formed by the strip with the energy U_* are delocalized. The relaxation rate of excitations within this strip is given by the inverse characteristic interaction

$$\tau_*^{-1} \sim U_* \approx T(PU)^2. \quad (20)$$

$$\tau_2^{-1} \approx U(R_*) \approx T\chi^2. \quad (21)$$

This dephasing rate decreases linearly with temperature. Compared with the phonon-induced channel providing a T^2 dependence (see [11]), the dephasing governed by the mechanism under consideration predominates at sufficiently low temperatures.

Regardless of the relaxation mechanism, the spectral diffusion rate is defined as [9, 11]

$$\langle|\dot{E}|\rangle \sim \tau_2^{-2}. \quad (22)$$

On the other hand, in a system with the $1/R^3$ interaction, this rate can be expressed as the ratio of the spectral diffusion amplitude χT and the thermal TLS relaxation time τ_1 [9, 11]:

$$\tau_2^{-2} = \chi T/\tau_1. \quad (23)$$

Using Eqs. (21) and (23), one can estimate the relaxation rate for thermal TLS as [8]

$$\tau_1^{-1} = \chi^3 T. \quad (24)$$

5. RELAXATION AT FINITE TEMPERATURES AND UNDER STRONG FIELDS

Previously, we have shown that the $1/R^3$ interaction of excitations and the external alternating field can independently result in delocalization and in irreversible TLS dynamics in the regime of arbitrarily strong disordering. Under real experimental conditions, both the TLS interaction and the external alternating (measuring) field are significant. Below, we consider the

Frequency-dependent relaxation rate

Frequency range	τ_1^{-1}	τ_2^{-1}
$0 < \omega < (T\chi^2)^2/a$	$T\chi^3$	$T\chi^2$
$(T\chi^2)^2/a < \omega < a\chi^2$	$(a\omega)^{1/2}\chi$	$(a\omega T^2)^{1/4}\chi$
$a\chi^2 < \omega < T\chi$	$a\chi^2$	$(aT)^{1/2}\chi^{3/2}$
$T\chi < \omega < a$	$(a/\omega)T\chi^3$	$(a/\omega)^{1/2}T\chi^2$
$a < \omega < T$ or $a < T\chi$	$T\chi^3$	$T\chi^2$

combined contribution of two those effects on the TLS relaxation.

Our analysis starts with the very low frequency of the external field, where the field can be treated as static. Then, the frequency will substantially increase to its maximum value $\omega \sim T$. The case of larger frequencies $\omega > T$ is beyond the scope of this paper, because of almost unavoidable heating. The results of our consideration are noted in the table.

Below, we consider the case of a relatively large field amplitude $a > T\chi$, where the field effect is significant. Such a regime has been realized in metallic glasses [35], where a nonlinear behavior has been revealed. The condition $a > T\chi$ means that the fluctuation of a TLS energy induced by an external field exceeds the interaction-induced fluctuation. To avoid heating, we also assume that the field amplitude is less than the thermal energy. Thus, in our consideration below, the field amplitude a satisfies the inequality

$$T\chi < a < T. \tag{25}$$

5.1. Quasistatic Field

When the frequency of the external field ω is very small, the field is almost static and we can ignore it. Then, the relaxation and dephasing rates are defined by the zero-field limit (Eqs. (21) and (24), respectively). In this regime, the fluctuations of TLS energy are due to the self-consistent spectral diffusion alone. The spectral diffusion rate is given by Eq. (22). The rate of a TLS energy fluctuation induced by the external field is $a\omega$. The external field can be treated as static until the spectral diffusion rate exceeds the fluctuation rate due to the field, i.e., when $\tau_2^{-2} > a\omega$, which takes place at $\omega < (T\chi^2)^2/a$ (see the first row in the table).

5.2. Adiabatic Relaxation Induced by a Slow Field

At a larger frequency

$$\omega > (T\chi^2)^2/a \tag{26}$$

the field cannot be ignored. It can stimulate transitions of TLS and irreversible relaxation due to energy-level crossings of different TLS. At a large field amplitude (Eq. (25)), crossing between two TLS energy levels E_0 and E_j ($E_0 - E_j - a\cos\omega t = 0$) [36] is possible provided that

$$|E_0 - E_j| < a. \tag{27}$$

The average distance between two TLS satisfying Eq. (27) is given by $R_a \simeq (Pa)^{-1/3}$.

Consider a flip-flop pair of TLS with close energies satisfying Eq. (27) and separated by a distance R_j. This pair undergoes level crossing during the field oscillation period ω^{-1}. If the pair transition amplitude is large, i.e, $V^2 = (U/R_j^3)^2 > \dot{E} \simeq a\omega$, *adiabatic relaxation* takes place. Then, according to the Landau–Zener theory, the excitation will transfer within a TLS pair with almost *unity probability* if the size R_j of the pair is sufficiently small (see Eq. (11)):

$$R_j < r_* \simeq (U/\sqrt{a\omega})^{1/3}. \tag{28}$$

The *adiabatic* regime takes place when each thermal TLS has a large number of adiabatic neighbors, thus satisfying Eqs. (27) and (28). This requires $r_* > R_a$, which leads to the frequency constraint (see the table, second row)

$$\omega < a\chi^2. \tag{29}$$

For a given thermal TLS, the relaxation rate τ_1^{-1} can be estimated as a frequency of adiabatic level crossings given by the product of the field oscillation frequency ω and the number of adiabatic level-crossing events during the single field oscillation. The latter value is given by the number of adiabatic neighbors χ_* that satisfy Eq. (27) and that are located within the sphere of the radius r_* around a given TLS, $\chi_* \simeq Par_*^3 = (a/\omega)^{1/2}\chi \gg 1$

$$\tau_1^{-1} \simeq \chi_*\omega = (a\omega)^{1/2}\chi. \tag{30}$$

It is interesting that the relaxation rate (Eq. (30)) coincides with that of Eq. (15).

In the adiabatic regime, we can estimate the dephasing rate using Eqs. (23) and (30):

$$\tau_2^{-1} = (T\chi/\tau_1)^{1/2} = (a\omega T^2)^{1/4}\chi. \tag{31}$$

It is important that dephasing (Eq. (31)) is so fast that the phase coherency between the periodic events of level crossings occurring during the period ω^{-1} can be ignored. This is true in the whole adiabatic frequency domain (the second row of the table), because the dephasing time is, in fact, less than the oscillation period (see Eqs. (25), (29), (31))

$$\omega\tau_2 = (\omega/(a\chi^2))^{3/4}(a/T)^{1/4}\chi^{1/2} < 1. \tag{32}$$

5.3. Nonadiabatic Regime at Intermediate Frequencies

Consider the *nonadiabatic regime*, which takes place at higher frequencies

$$\omega > a\chi^2. \tag{33}$$

This condition is opposite to Eq. (29). In this regime, the vast majority of thermal TLS undergo nonadiabatic level crossings (see Eq. (34) below).

In the adiabatic case, we have dealt with the regime $\omega\tau_2 < 1$ (see Eq. (32)). In the nonadiabatic regime, characterized by Eq. (33), one should distinguish between two cases, namely, $\omega\tau_2 < 1$ and $\omega\tau_2 > 1$, where the phase memory between two subsequent level crossings either exists or does not exist, respectively.

We consider the first case $\omega\tau_2 < 1$, which is valid at the border of adiabatic and nonadiabatic domains $\omega = a\chi^2$ (see the table). Here, dephasing is fast, and phase correlations between periodic level crossings can be ignored. Most efficient flip-flop transitions occur between thermal TLS separated by the average distance R_a (Eq. (14)). In fact, this distance is the characteristic separation of neighboring two-level systems with energy differences less than the field amplitude a that is required for level crossing. On the other hand, at larger distances, the nonadiabatic-transition probability decreases with the distance very quickly, i.e., as $V^2 \sim R^{-6}$. Therefore, the most efficient energy transfer should occur between nearest neighbors. The relevant transition amplitude reads $V_a = U/R_a^3 \sim a\chi$. In the large-frequency case (Eq. (33)), one has

$$V_a^2 < \dot{E} = a\omega \tag{34}$$

and transitions are *nonadiabatic*. According to the Landau–Zener theory, their probability per one energy-level crossing, of occurring a few times for the period ω^{-1} is $W_a \simeq V_a^2/(a\omega) = (a/\omega)\chi^2$. This probability defines the TLS relaxation rate as the inverse average time between two successful transitions

$$\tau_1^{-1} = W_a\omega \simeq a\chi^2. \tag{35}$$

Then, using Eq. (23), one finds

$$\tau_2^{-1} = a^{1/2}T^{1/2}\chi^{3/2}. \tag{36}$$

The above derivation remains valid until the breaking of the condition of Eq. (32) at

$$\omega > a^{1/2}T^{1/2}\chi^{3/2}. \tag{37}$$

In the opposite case, i.e., that of $\omega\tau_2 > 1$, the field periodicity is significant, meaning that the formalism of DE introduced in Section 3 (see also [31]) becomes applicable.

The further analysis depends on the relationship between the DE energy splitting ω and the spectral diffusion amplitude $T\chi$ (see Eq. (25)). We start with the case of lower frequencies (see the table)

$$\omega \le T\chi, \tag{38}$$

where all pairs of TLS with an energy difference of less than the field amplitude a inevitably undergo DE level crossing during the spectral diffusion quasi-period τ_1. These crossing levels are coupled by the transition amplitude of dressed excitations (Eq. (10)).

In the regime of Eqs. (37) and (38), relaxation is induced by nonadiabatic level crossing caused by spectral diffusion. On the other hand, the spectral diffusion is caused by the relaxation dynamics of TLS, so the process is self-consistent [8, 27, 33, 34].

We assume that there is an existing characteristic relaxation rate of thermal TLS τ_1^{-1}. Transitions of thermal TLS change other TLS energies, thus giving rise to spectral diffusion. The spectral diffusion leads to level crossing of DE, stimulating irreversible transitions with the output rate r_{out}. The self-consistent relaxation mechanism requires the input rate τ_1^{-1} to be equal to this output rate.

The rate of transitions induced by the spectral diffusion can be estimated as the number of transitions induced by level crossings during the quasiperiod of the spectral diffusion τ_1 multiplied by the frequency of spectral-diffusion cycles τ_1^{-1}. Energy-level crossing for two DE happens when (cf. Eq. (8); Fig. 2)

$$E_1 - E_2 = n\omega \tag{39}$$

(where n is an integer number). The total number of such crossings due to the spectral-diffusion induced energy fluctuation $T\chi$ for the time τ_1 is given by

$$N_{\tau_1} \simeq (T\chi/\omega). \tag{40}$$

Multiple crossings for the same TLS pair give a logarithmic correction to Eq. (40) and can be neglected in the qualitative scaling approximation [8, 33, 34]. This is due to the specific behavior of the spectral diffusion induced by the $1/R^3$ interaction. For this spectral diffusion, the characteristic energy fluctuation is directly proportional to the time [9, 11]. Therefore, this is an anomalous diffusion process as compared to the normal diffusive $t^{1/2}$ behavior of the displacement. For this super-diffusion case, the probability of energy returning back to its initial value is not so large as in the case of the normal diffusion.

We consider nonadiabatic flip-flop transitions only between neighboring thermal DE separated by the distance R_a (see Eq. (14)), because the nonadiabatic transition probability over larger distances drops with the distance very quickly (R^{-6}). The probability of a nonadiabatic transition during one level crossing for such a pair of thermal DE induced by the spectral diffusion with the rate $\langle|\dot{\varepsilon}|\rangle \approx \tau_2^{-2}$ can be estimated using the Lan-

dau–Zener theory in the nonadiabatic limit. The transition probability can be found using the transition amplitude (Eq. (10)) for $R = R_a$

$$W_* = (V_a\tau_2)^2 < 1. \quad (41)$$

The relaxation rate is expressed as

$$\tau_1^{-1} = r_{\text{out}} = N_{\tau_1}W_*/\tau_1 \simeq a\chi^2. \quad (42)$$

One can show that, if we take the input relaxation rate as being slower than Eq. (42), the output rate will be faster than the input one, and, if we take the input rate as being larger than Eq. (42), the output rate will be smaller than the input rate. Therefore, the solution (Eq. (42)) is stable and the only one possible. Thus, the *nonadiabatic single-particle* relaxation described by Eqs. (35) and (36) takes place within the whole frequency domain $a\chi^2 < \omega < T\chi$ (table, third row).

5.4. High Frequencies

When the external field frequency ω exceeds the scale $T\chi$, the spectral diffusion does not necessarily lead to the DE energy-level crossing for closely located pairs that was considered in Section 5.3. The single-particle delocalization in this case does not occur similarly to the case that was studied in Section 2, because the field frequency is large compared to that needed for the delocalization (see the table, line 2). On the other hand, there exists a finite concentration of excited DE (excited TLS dressed by some certain number of the external-field quanta, see Fig. 2), and the many-body relaxation should be similar to that described in Section 4.

Following the approach of Section 4, one can introduce the concept of a resonant pair of DE rather than of RP (resonant pairs of TLS). A resonant pair of DE (RPDE) is defined as a pair of DE separated by the distance R_{12} with sublevel energies E_1 and E_2, which obeys the resonant condition for some integer $n < a/\omega$ (see Fig. 2)

$$\Delta_{pn} = |E_1 - E_2 + n\omega| < T(R). \quad (43)$$

Here, the transition amplitude $T(R) \approx (U/R^3)\sqrt{\omega/a}$ is taken from Eq. (10). Like a resonant pair, one can treat a RPDE as a new kind of two-level system. The parameter Δ_{pn} is the asymmetry energy for RPDE. Then, strictly following the derivation between Eqs. (16) and (18), one can estimate the concentration of RPDE for any given value of transition amplitude $T(R)$. This concentration is given by the expression

$$N^* \approx T\chi^2\sqrt{\frac{a}{\omega}}. \quad (44)$$

The concentration N^* is independent of the given parameter $T(R)$, just as the concentration of RP N_* defined by Eq. (18) does not depend on the parameter Δ_{0p}. The appearance of the factor $\sqrt{a/\omega}$ in Eq. (44) in comparison with Eq. (18) can be understood as follows. The concentration N^* compared with N_* acquires the factor $n_* = a/\omega$, since resonance condition (43) should be valid for at least one integer $|n| < n_*$ so that the number of possible distinguishable resonances for the single pair multiplies the resonance probability by the factor n_*. On the other hand, the resonance probability decreases by the factor $1/\sqrt{n_*}$ proportionally to the reduction in the transition amplitude (Eq. (10)). The overall effect is just the increase in the density of resonant pairs by the factor $\sqrt{a/\omega}$ (cf. Eq. (13)). Accordingly, the interaction between these resonant DE pairs is enhanced by the same factor, and the new dephasing rate is given by this universal interaction:

$$1/\tau_2 = T\chi^2(a/\omega)^{1/2}. \quad (45)$$

Making use of Eq. (23), one can estimate the relaxation rate as

$$\tau_1^{-1} = (T\chi\tau_2^2)^{-1} = (a/\omega)T\chi^3. \quad (46)$$

When the frequency exceeds the amplitude $a < \omega < T$, excitation dressing becomes negligibly small and we return to the linear regime (the last row of the table). The regime when the frequency exceeds the temperature is realized in several echo measurements [2]. This regime can lead to heating and requires a special study.

6. SUMMARY

We have described the self-relaxation rate of TLS at different temperatures, external field amplitudes, and frequencies. We have found that the relaxation rate is either temperature-independent (see the table), or decreases with temperature as T. The phonon-stimulated relaxation $\tau_1^{-1} \propto T^3$ (see [9]) is much slower in the low-temperature limit, and the self-relaxation described above should dominate when $T \longrightarrow 0$.

The suggested theory predicts the parametric dependences of relaxation rates in various regimes. In contrast to the theory for the phonon-stimulated relaxation (see the review of Hunklinger and Raychaudchary [9] and references therein), we are not able to determine the numerical coefficients for each rate process shown in the table. This missing factor can be of order of unity, but it can also be much greater or much smaller than unity, e.g., 0.01 or 10^2. An example of the latter situation is given by the tunneling rate involving two-phonon processes, which was examined by Kagan and Maksimov [37] for the quantum diffusion problem; they found a large numerical prefactor of 1000 due to the large factorial factor involved.

We also expect large numerical prefactors for our expressions. There are several reasons for this. First, each factor χ possibly involves the spherical integration

factor 4π or $4\pi/3$ in addition to the PU factor. In this paper, we have included the factor 4π in the definition of our factor χ (Eq. (4)), contrary to previous work. This was done because this factor naturally appears in the localization criterion (Eq. (3)) and, correspondingly, it can enter the rate expressions of the table. Thus, the parameter of interaction weakness $PU \sim 10^{-4}$–10^{-3} can be increased by an order of magnitude. Accordingly, the "linear" expression for the relaxation rate (Eq. (24)) agrees better with the results of the systematic internal-friction measurements performed by Classen, Burkert, Enss, and Hunklinger [6]. We believe that the factor $\chi = 4\pi PU$ reflects the absolute values of relaxation rates better than the smaller factor $\chi = PU$ itself. Accurate calculations of the numerical factors are beyond the scope of our qualitative study. The alternative explanation for a quantitative disagreement [6] can be based on the strong nonlinearity. For instance, the extra factor a/ω in the relaxation rate (see Eq. (46)) can account for the difference of theory and experiment as well. The comparison of our predictions with experiment can still be performed using the experimental data for different glasses, with different values of the parameter χ. Note that the preliminary numerical analysis of the Floquet state delocalization, which was described in Section 3, in the equivalent one-dimensional model supports our expectations of a large numerical prefactor exceeding unity by at least one order of magnitude.

Another possible problem of the direct application of our theory to the experiment is that the interaction-induced relaxation leads to equilibration within the TLS subsystem rather than for the whole system. This is similar to the spin–spin and spin–lattice relaxations in the NMR problem. Then, in order to describe the heat balance between TLS and phonons, one should introduce the separate TLS and phonon temperatures and perform the thermal balance analysis for the whole system. This study is beyond the scope of this paper.

The crossover temperature between two regimes depends on the external field parameters a and ω. It usually reduces with a decrease in the field amplitude and can also decrease with a decrease in the field frequency (see the table). This knowledge helps us to understand the absence of the interaction-stimulated relaxation reported by Pohl and coworkers in [38]. In this work, the strain field amplitude was made extremely small ($\varepsilon \le 10^{-8}$), while the frequency $\omega \sim 0.5$ MHz was higher than in other groups' studies [4–6] and belongs to the range described by the fourth column of the table, when the relaxation rate decreases with increasing ω.

Our results agree with the recent low-temperature measurements of the dielectric constant by Ladieu and coworkers [24, 39], which can be interpreted assuming that the TLS relaxation rate becomes temperature-independent. This shows the dependence on the external field amplitude $\sqrt{a}$ (the second row of the table). Another very interesting discovery of Ladieu and coworkers includes the sensitivity of the TLS relaxation rate to the sample thickness. The suggested theory is essentially three-dimensional. If the thickness of the sample is less than the typical distance between resonant pairs (around a few tens of nanometers), then the irreversible relaxation will remarkably slow down. This agrees with the observations of [24, 39]. A more accurate theoretical analysis of the data is necessary for a careful interpretation.

Our predictions can be directly verified using the nonequilibrium measurement technique developed by Osheroff and coworkers [5, 40], which is based on an analysis of the response of the system to the large sweep of the external electric field E_{DC} when taking different times τ_s. Our results for the field-stimulated relaxation are valid in this case if one takes $a \sim E_{DC}\mu_{TLS}$ (where $\mu_{TLS} \sim 1$D is the typical TLS dipole moment) and $\omega \simeq 1/\tau_s$. Since the maximum possible amplitude a is very high, namely, $a \ge 0.1$ K, while the minimum "frequency" is as low as $\omega \sim 1$ s^{-1}, all the regimes described in the table can be attained and analyzed.

The authors would like to draw the reader's attention to the fact that, during the past decade, the activity dealing with interactions between active point defects in amorphous materials has been appreciably supported by the Russian Foundation for Basic Research. In addition, the work of A.L. Burin is supported by TAMS GL fund no. 211043 through Tulane University.

We are sincerely grateful to Yu. Kagan, in collaboration with whom we obtained the vast majority of the results described above. A.B. and I.P. are grateful to the organizers and participants of the International Workshop "Collective phenomena in glasses at low temperature" (Dresden, 2003) for many useful discussions and suggestions. And finally, I.P. has the pleasure to thank P. Fulde for valuable discussions and kind hospitality during his stay in Dresden, where this paper was prepared.

REFERENCES

1. P. W. Anderson, B. I. Halperin, and C. M. Varma, Philos. Mag. **25**, 1 (1972); W. A. Phillips, J. Low Temp. Phys. **7**, 351 (1972).
2. L. Bernard, L. Piche, G. Schumacher, and J. Joffrin, J. Low Temp. Phys. **45**, 411 (1979); G. Baier and M. V. Schickfus, Phys. Rev. B **38**, 9952 (1988).
3. B. Golding and T. E. Graebner, in *Amorphous Solids*, Ed. by W. A. Phillips (Springer, Berlin, 1984), Topics in Current Physics, Vol. 24, p. 107.
4. P. Esquinazi, R. König, and F. Pobell, Z. Phys. B **87**, 305 (1992).
5. S. Rogge, D. Natelson, and D. D. Osheroff, Phys. Rev. Lett. **76**, 3136 (1996).
6. J. Classen, T. Burkert, C. Enss, and S. Hunklinger, Phys. Rev. Lett. **84**, 2176 (2000).
7. M. A. Continentino, Phys. Rev. B **22**, 6127 (1980); C. C. Yu, Phys. Rev. B **32**, 4220 (1985); S. V. Maleev, Sov. Phys. JETP **67**, 157 (1988); A. Würger and D. Bodea, Chem. Phys. **296**, 301 (2004).

8. A. L. Burin and Yu. Kagan, Zh. Éksp. Teor. Fiz. **106**, 633 (1994) [JETP **79**, 347 (1994)].
9. S. Hunklinger and A. K. Raychaudchary, Prog. Low Temp. Phys. **9**, 267 (1986).
10. W. Arnold and S. Hunklinger, Solid State Commun. **17**, 833 (1975).
11. J. L. Black and B. I. Halperin, Phys. Rev. B **16**, 2819 (1968).
12. S. Volker, J. Lumin. **36**, 251 (1987).
13. H. Maier, R. Wunderlich, D. Haarer, *et al.*, Phys. Rev. Lett. **74**, 5252 (1995).
14. K. Fritsch and J. Friedrich, Physica D (Amsterdam) **107**, 218 (1997).
15. J. E. Grabner and B. Golding, Phys. Rev. B **19**, 964 (1979).
16. D. J. Salvino, S. Rogge, B. Tigner, and D. D. Osheroff, Phys. Rev. Lett. **73**, 268 (1994).
17. A. L. Burin, J. Low Temp. Phys. **100**, 309 (1995).
18. C. Enss and S. Hunklinger, Phys. Rev. Lett. **79**, 2831 (1997).
19. P. Strehlow, C. Enss, and S. Hunklinger, Phys. Rev. Lett. **80**, 5361 (1998).
20. S. Kettemann, P. Fulde, and P. Strehlow, Phys. Rev. Lett. **83**, 4325 (1999).
21. P. Strehlow, M. Wohlfahrt, A. G. M. Jansen, *et al.*, Phys. Rev. Lett. **84**, 1938 (2000).
22. M. Wohlfahrt, P. Strehlow, C. Enss, and S. Hunklinger, Europhys. Lett. **56**, 690 (2001).
23. A. Würger, Phys. Rev. Lett. **88**, 075502 (2002).
24. J. Le Cochec, F. Ladieu, and P. Pari, Phys. Rev. B **66**, 064203 (2002).
25. P. W. Anderson, Phys. Rev. **109**, 2041 (1958).
26. B. D. Laikhtman, Phys. Rev. B **31**, 490 (1985).
27. I. Ya. Polishchuk, L. A. Maksimov, and A. L. Burin, JETP **79**, 634 (1994).
28. B. I. Shklovskiĭ and A. L. Éfros, *Electronic Properties of Doped Semiconductors* (Nauka, Moscow, 1979; Springer, Heidelberg, 1984).
29. J. J. Freeman and A. C. Anderson, Phys. Rev. B **34**, 5684 (1986); A. J. Leggett and C. C. Yu, Comments Condens. Matter Phys. **14**, 231 (1989).
30. A. L. Burin, D. Natelson, D. D. Osheroff, and Yu. Kagan, in *Tunneling Systems in Amorphous and Crystalline Solids*, Ed. by P. Esquinazi (Springer, Berlin, 1998), Chap. 5, p. 243.
31. A. L. Burin, Yu. Kagan, and I. Ya. Polishchuk, Phys. Rev. Lett. **86**, 5616 (2001).
32. L. S. Levitov, Phys. Rev. Lett. **64**, 547 (1990); Ann. Phys. (Leipzig) **8**, 697 (1999).
33. A. L. Burin, Yu. Kagan, L. A. Maksimov, and I. Ya. Polishchuk, Phys. Rev. Lett. **80**, 2945 (1998).
34. A. L. Burin, L. A. Maksimov, and I. Ya. Polishchuk, JETP Lett. **49**, 784 (1989).
35. R. König, M. A. Ramos, I. Usherov-Marshak, *et al.*, Phys. Rev. B **65**, 180201 (2002).
36. The field amplitude α strongly fluctuates in its value and sign because of the random orientation of each TLS dipole or elastic moment with respect to the external field. Therefore, the difference in the coupling constants of two different TLS has the same scale, namely, α, thus modulating the energy difference of TLS pairs.
37. Yu. Kagan and L. A. Maksimov, Zh. Éksp. Teor. Fiz. **87**, 348 (1984) [Sov. Phys. JETP **60**, 201 (1984)].
38. E. J. Thompson, G. Lawes, J. M. Parpia, and R. O. Pohl, Phys. Rev. Lett. **84**, 4601 (2000).
39. F. Ladieu, J. Le Cochec, P. Pari, *et al.*, Phys. Rev. Lett. **90**, 205501 (2003); J. Le Cochec and F. Ladieu, Eur. Phys. J. B **32**, 13 (2003).
40. S. Ludwig and D. D. Osheroff, Phys. Rev. Lett. **91**, 105501 (2003).